

IMAGING HETEROGENEOUS OBJECTS USING TRANSPORT THEORY AND
NEWTON'S METHOD

A Thesis

by

NATHANIEL RAYMOND FREDETTE

Submitted to the Office of Graduate Studies of
Texas A&M University
in partial fulfillment of the requirements for the degree of

MASTER OF SCIENCE

December 2011

Major Subject: Nuclear Engineering

IMAGING HETEROGENEOUS OBJECTS USING TRANSPORT THEORY AND
NEWTON'S METHOD

A Thesis

by

NATHANIEL RAYMOND FREDETTE

Submitted to the Office of Graduate Studies of
Texas A&M University
in partial fulfillment of the requirements for the degree of

MASTER OF SCIENCE

Approved by:

Co-Chairs of Committee,	Jean C. Ragusa
	Wolfgang Bangerth
Committee Members,	Marvin Adams
Head of Department,	Raymond Juzaitis

December 2011

Major Subject: Nuclear Engineering

ABSTRACT

Imaging Heterogeneous Objects Using Transport Theory and Newton's Method.

(December 2011)

Nathaniel Raymond Fredette, B.S., Marquette University

Co-Chairs of Advisory Committee: Dr. Jean C. Ragusa
Dr. Wolfgang Bangerth

This thesis explores the inverse problem of optical tomography applied to two-dimensional heterogeneous domains. The neutral particle transport equation was used as the forward model to simulate how neutral particles stream through and interact within these heterogeneous domains. A constrained optimization technique that uses Newton's method served as the basis of the inverse problem.

The capabilities and limitations of the presented method were explored through various two-dimensional domains. The major factors that influenced the ability of the optimization method to reconstruct the cross sections of these domains included the locations of the sources used to illuminate the domains, the number of separate experiments used in the reconstruction, the locations where measurements were collected, the optical thickness of the domain, the amount of signal noise and signal bias applied to the measurements, and the initial guess for the cross section distribution. All of these factors were explored for problems with and without scattering.

Increasing the number of sources, measurements and experiments used in the reconstruction generally produced more successful reconstructions with less error. Using more sources, experiments and measurements also allowed for optically thicker domains to be reconstructed. The maximum optical thickness that could be reconstructed with this method was ten mean free paths for pure absorber domains and two mean free paths for domains with scattering. Applying signal noise and signal bias to the measured fluxes produced more error in the reconstructed image. Gener-

ally, Newton's method was more successful at reconstructing domains from an initial guess for the cross sections that was greater in magnitude than their true values than from an initial guess that was lower in magnitude.

To my father and mother, Mark and Denise Fredette

ACKNOWLEDGMENTS

I would like to acknowledge my father and mother, Mark and Denise Fredette, for their support and advice during the process of achieving this degree. I would also like to acknowledge my sister, Jackie Fredette, for her suggestions. I would like to thank my friends and family for helping me develop into a productive young professional.

I would like to acknowledge Dr. Jean C. Ragusa for his time and support throughout this project, his knowledge of transport methods and his professional counsel when considering my career options. In addition, I would like to acknowledge Dr. Wolfgang Bangerth for his insight regarding optimization methods and programming.

TABLE OF CONTENTS

CHAPTER		Page
I	INTRODUCTION	1
	A. Motivation	1
	B. Inverse Problems	2
	C. Optimization	4
	D. Outline of Thesis	5
II	PREVIOUS WORK	6
	A. Inverse Neutral Particle Transport Related to Cargo Container Imaging	6
	B. Radiation Imaging in Medical Physics	9
	C. Imaging Applied to DC-Resistivity and Magnetostatics . .	15
III	TRANSPORT THEORY	17
	A. Balance Equation	17
	B. Adjoint Transport Equation	19
IV	OPTIMIZATION TECHNIQUES	20
	A. Overview	20
	B. Nelder-Mead Method	22
	C. Newton's Method	24
	1. Gradient and Hessian System	26
	2. Schur Complement	28
	3. Line Search	28
	a. Sufficient Decrease Condition	29
	b. Curvature Condition	30
	c. Additional Checks	31
V	INVERSE TRANSPORT PROBLEM	32
	A. Objective Function	32
	B. Formulation of Lagrangian	33
	C. Optimality Conditions	34
	D. Hessian Matrix	36
	E. Schur Complement Method	38

CHAPTER		Page
	F. Newton's Method for Multiple Experiments	40
VI	RESULTS AND DISCUSSION	43
	A. Pure Absorber Problems	43
	1. Example 1 - Misfit Surfaces	43
	2. Example 2 - Homogeneous Domain and Dual In- clusion Convergence Study	49
	3. Example 3 - Four-Strip Domain	54
	4. Example 4 - Four-Region Domain with Illuminat- ing Sources on 1, 2, 3 or 4 Side(s)	57
	5. Summary of Findings from Pure Absorber Problems .	61
	B. Pure Absorbers with Multiple Experiments	63
	1. Example 5 - Central Inclusion Domains with 8 Ex- periments	63
	2. Example 6 - Central Inclusion Domains with 16 Experiments	67
	3. Example 7 - Homogeneous Domain Initial Guess Study	71
	4. Example 8 - Four-Region Domain with Measure- ments taken on 1, 2, 3 and 4 Sides	76
	5. Summary of Findings from Pure Absorbers with Multiple Experiments	79
	C. Pure Absorbers with Signal Noise and Bias	80
	1. Example 9 - Four-Strip Domain with Signal Noise . .	81
	2. Example 10 - Central Inclusion with Signal Noise and Positive and Negative Signal Bias	84
	3. Summary of Findings from Pure Absorbers with Signal Noise and Bias	89
	D. Problems with Scattering	90
	1. Example 11 - Scattering Misfit Surface Plots	91
	2. Example 12 - 8-Parameter Homogeneous Domain . . .	95
	3. Example 13 - Four-Strip Domain with No Signal Noise, Only Noise, and Both Noise and Bias	100
	4. Example 14 - Central Inclusion Optical Thickness Study Reconstructing Both Scattering and Total Cross Sections	113
	5. Example 15 - Homogeneous Domain Initial Guess Study Reconstructing Both Scattering and Total Cross Sections	117

CHAPTER	Page
6. Example 16 - Four-Region Domain with Illuminating Sources on 1, 2, 3 or 4 Sides Reconstructing Both Scattering and Total Cross Sections	124
7. Example 17 - Four-Region Domain Reconstructing Both Scattering and Total Cross Sections Using Measurements from 1, 2, 3 and 4 Sides	129
8. Summary of Findings from Scattering Problems	134
VII CONCLUSIONS AND OUTLOOK	137
REFERENCES	139
VITA	142

LIST OF TABLES

TABLE		Page
VI-I	Misfit Surface Parameter Description	46
VI-II	Homogeneous Domain Parameter Description	50
VI-III	Homogeneous Domain Convergence Comparison	52
VI-IV	Dual Inclusion Domain Parameter Description	53
VI-V	Parameter Description of Four-Strip Domain	56
VI-VI	Parameter Description of Four-Region Domain with Varying Illuminating Sources	58
VI-VII	Parameter Description of Central Inclusion Domains with 8 Experiments	64
VI-VIII	Parameter Description of Central Inclusion Domains with 16 Experiments	68
VI-IX	Parameter Description of Homogeneous Domain Reconstruction from Various Initial Guesses	72
VI-X	Parameter Description of Four-Region Domain Measuring on 1, 2, 3 or 4 Side(s) of Model	77
VI-XI	Parameter Description of Four-Strip Domain with Signal Noise . . .	82
VI-XII	Parameter Description of Central Inclusion Domain with Signal Noise and Signal Bias	85
VI-XIII	Parameter Description of Misfit Surface Geometry	92
VI-XIV	Parameter Description of Homogeneous Domain with Scattering . . .	96
VI-XV	Parameter Description of Four-Strip Domain with Signal Noise and Bias	101

TABLE	Page
VI-XVI Average Cross Section Comparison for Four-Strip Domain with 0.10% Signal Noise and 1.00% Positive Signal Bias	107
VI-XVII Average Cross Section Comparison for Four-Strip Domain with 0.10% Signal Noise and 5.00% Positive Signal Bias	109
VI-XVIII Average Cross Section Comparison for Four-Strip Domain with 0.10% Signal Noise and 1.00% Negative Signal Bias	111
VI-XIX Average Cross Section Comparison for Four-Strip Domain with 0.10% Signal Noise and 5.00% Negative Signal Bias	113
VI-XX Parameter Description of Central Inclusion Domains with 8 Ex- periments and Scattering	114
VI-XXI Parameter Description of Homogeneous Domain Reconstruction from Various Initial Guesses with Scattering	118
VI-XXII Parameter Description of Four-Region Domain with Scatting and Varying Illuminating Sources	125
VI-XXIII Parameters Description of Four-Region Domain Measuring on 1, 2, 3 or 4 Side of Model	130

LIST OF FIGURES

FIGURE		Page
VI-1	Two-Parameter Problem - True Cross Section Distribution.	44
VI-2	Two-Parameter Problem - Left Illumination Only.	47
VI-3	Two-Parameter Problem - Right Illumination Only.	48
VI-4	Two-Parameter Problem - Illumination from Both Left and Right Sides.	49
VI-5	Homogeneous Domain: Reconstructed Cross Sections and Error Using Newton's Method.	51
VI-6	Homogeneous Domain: Reconstructed Cross Sections and Error Using Nelder-Mead Method.	51
VI-7	Dual Inclusion Domain Reconstruction.	54
VI-8	Actual Four-Strip Domain.	55
VI-9	Four-Strip Domain Reconstructed Cross Sections and Error.	57
VI-10	Diagram of Four-Region Domain with Sides and Material Regions Identified.	59
VI-11	Domain with Source on 1 Side Reconstructing the Total Cross Sections.	60
VI-12	Domain with Sources on 2 Sides Reconstructing the Total Cross Sections.	60
VI-13	Domain with Sources 3 Sides Reconstructing the Total Cross Sections.	61
VI-14	Domain with Sources on 4 Sides Reconstructing the Total Cross Sections.	61
VI-15	Reconstruction, Error and Condition Number Results for the 8x8cm Central Inclusion Problem with 8 Experiments.	65

FIGURE	Page
VI-16 Reconstruction, Error and Condition Number Results for the 12x12cm Central Inclusion Problem with 8 Experiments.	66
VI-17 Reconstruction, Error and Condition Number Results for the 16x16cm Central Inclusion Problem with 8 Experiments.	66
VI-18 Reconstruction, Error and Condition Number Results for the 20x20cm Central Inclusion Problem with 8 Experiments.	67
VI-19 Reconstruction, Error and Condition Number Results for the 8x8cm Central Inclusion Problem with 16 Experiments.	69
VI-20 Reconstruction, Error and Condition Number Results for the 12x12cm Central Inclusion Problem with 16 Experiments.	69
VI-21 Reconstruction, Error and Condition Number Results for the 16x16cm Central Inclusion Problem with 16 Experiments.	70
VI-22 Reconstruction, Error and Condition Number Results for the 20x20cm Central Inclusion Problem with 16 Experiments.	70
VI-23 Reconstruction, Error and Condition Number Results for the 24x24cm Central Inclusion Problem with 16 Experiments.	70
VI-24 Initial Guess of $75\% \pm 5\%$ of Actual Cross Section of Homogeneous Domain.	73
VI-25 Initial Guess of $50\% \pm 10\%$ of Actual Cross Section of Homogeneous Domain.	73
VI-26 Initial Guess of $25\% \pm 15\%$ of Actual Cross Section of Homogeneous Domain.	74
VI-27 Initial Guess of $1000\% \pm 200\%$ of Actual Cross Section of Homogeneous Domain.	75
VI-28 Initial Guess of $5000\% \pm 1000\%$ of Actual Cross Section of Homogeneous Domain.	75
VI-29 Initial Guess of $10000\% \pm 2500\%$ of Actual Cross Section of Homogeneous Domain.	75

FIGURE		Page
VI-30	Four-Region Domain Measuring on 1 Side.	78
VI-31	Four-Region Domain Measuring on 2 Sides.	78
VI-32	Four-Region Domain Measuring on 3 Sides.	79
VI-33	Four-Region Domain Measuring on 4 Sides.	79
VI-34	Reconstructions of Four-Strip Domain with Differing Amounts of Signal Noise.	83
VI-35	Error in Reconstructions of Four-Strip Domain with Differing Amounts of Signal Noise.	83
VI-36	Reconstruction of Central Inclusion Domain with Differing Amounts of Signal Noise.	86
VI-37	Error in Reconstruction of Central Inclusion Domain with Differ- ing Amounts of Signal Noise.	86
VI-38	Central Inclusion Domain with 0.10% Signal Noise and Positive 1.00% Signal Bias.	87
VI-39	Central Inclusion Domain with 0.10% Signal Noise and Positive 5.00% Signal Bias.	88
VI-40	Central Inclusion Domain with 0.10% Signal Noise and Negative 1.00% Signal Bias.	89
VI-41	Central Inclusion Domain with 0.10% Signal Noise and Negative 5.00% Signal Bias.	89
VI-42	Misfit Surface Plot with 10% Scattering.	93
VI-43	Misfit Surface Plot with 50% Scattering.	94
VI-44	Misfit Surface Plot with 90% Scattering.	94
VI-45	Misfit Surface Plot with 99% Scattering.	95
VI-46	Total Cross Section Reconstruction for the 8-Parameter Homoge- neous Domain with 10% Scattering.	97

FIGURE		Page
VI-47	Scattering Cross Section Reconstruction for the 8-Parameter Homogeneous Domain with 10% Scattering.	97
VI-48	Total Cross Section Reconstruction for the 8-Parameter Homogeneous Domain with 50% Scattering.	98
VI-49	Scattering Cross Section Reconstruction for the 8-Parameter Homogeneous Domain with 50% Scattering.	98
VI-50	Total Cross Section Reconstruction for the 8-Parameter Homogeneous Domain with 90% Scattering.	99
VI-51	Scattering Cross Section Reconstruction for the 8-Parameter Homogeneous Domain with 90% Scattering.	99
VI-52	Total Cross Section Reconstruction Results for Four-Strip Domain without Signal Noise.	102
VI-53	Scattering Cross Section Reconstruction Results for Four-Strip Domain without Signal Noise.	102
VI-54	Total Cross Section Reconstruction Results for Four-Strip Domain with 0.01% Signal Noise.	103
VI-55	Scattering Cross Section Reconstruction Results for Four-Strip Domain with 0.01% Signal Noise.	103
VI-56	Total Cross Section Reconstruction Results for Four-Strip Domain with 0.10% Signal Noise.	104
VI-57	Scattering Cross Section Reconstruction Results for Four-Strip Domain with 0.10% Signal Noise.	104
VI-58	Total Cross Section Reconstruction Results for Four-Strip Domain with 1.00% Signal Noise.	105
VI-59	Scattering Cross Section Reconstruction Results for Four-Strip Domain with 1.00% Signal Noise.	105
VI-60	Total Cross Section Reconstruction Results for Four-Strip Domain with 0.10% Signal Noise and 1.00% Positive Signal Bias.	106

FIGURE	Page
VI-61 Scattering Cross Section Reconstruction Results for Four-Strip Domain with 0.10% Signal Noise and 1.00% Positive Signal Bias. . .	106
VI-62 Total Cross Section Reconstruction Results for Four-Strip Domain with 0.10% Signal Noise and 5.00% Positive Signal Bias.	108
VI-63 Scattering Cross Section Reconstruction Results for Four-Strip Domain with 0.10% Signal Noise and 5.00% Positive Signal Bias. . .	108
VI-64 Total Cross Section Reconstruction Results for Four-Strip Domain with 0.10% Signal Noise and 1.00% Negative Signal Bias.	110
VI-65 Scattering Cross Section Reconstruction Results for Four-Strip Domain with 0.10% Signal Noise and 1.00% Negative Signal Bias. .	110
VI-66 Total Cross Section Reconstruction Results for Four-Strip Domain with 0.10% Signal Noise and 5.00% Negative Signal Bias.	111
VI-67 Scattering Cross Section Reconstruction Results for Four-Strip Domain with 0.10% Signal Noise and 5.00% Negative Signal Bias. .	112
VI-68 Total Cross Sections Results for the 4x4cm Central Inclusion Domain.	115
VI-69 Scattering Cross Sections Results for the 4x4cm Central Inclusion Domain.	115
VI-70 Total Cross Sections Results for the 6x6cm Central Inclusion Domain.	116
VI-71 Scattering Cross Sections Results for the 6x6cm Central Inclusion Domain.	116
VI-72 Initial Guess, Reconstruction and Error Results for Total Cross Section with $90 \pm 2\%$ Initial Guess.	119
VI-73 Initial Guess, Reconstruction and Error Results for Scattering Cross Section with $90 \pm 2\%$ Initial Guess.	119
VI-74 Initial Guess, Reconstruction and Error Results for Total Cross Section with $80 \pm 5\%$ Initial Guess.	120
VI-75 Initial Guess, Reconstruction and Error Results for Scattering Cross Section with $80 \pm 5\%$ Initial Guess.	120

FIGURE	Page
VI-76 Initial Guess, Reconstruction and Error Results for Total Cross Section with $50 \pm 10\%$ Initial Guess.	120
VI-77 Initial Guess, Reconstruction and Error Results for Scattering Cross Section with $50 \pm 10\%$ Initial Guess.	121
VI-78 Initial Guess, Reconstruction and Error Results for Total Cross Section with $1000 \pm 200\%$ Initial Guess.	122
VI-79 Initial Guess, Reconstruction and Error Results for Scattering Cross Section with $1000 \pm 200\%$ Initial Guess.	122
VI-80 Initial Guess, Reconstruction and Error Results for Total Cross Section with $5000 \pm 1000\%$ Initial Guess.	123
VI-81 Initial Guess, Reconstruction and Error Results for Scattering Cross Section with $5000 \pm 1000\%$ Initial Guess.	123
VI-82 Initial Guess, Reconstruction and Error Results for Total Cross Section with $10000 \pm 2500\%$ Initial Guess.	123
VI-83 Initial Guess, Reconstruction and Error Results for Scattering Cross Section with $10000 \pm 2500\%$ Initial Guess.	124
VI-84 Total Reconstruction and Error for Four-Region Domain with Sources on 1 Side.	126
VI-85 Scattering Reconstruction and Error for Four-Region Domain with Sources on 1 Side.	126
VI-86 Total Reconstruction and Error for Four-Region Domain with Sources on 2 Sides.	127
VI-87 Scattering Reconstruction and Error for Four-Region Domain with Sources on 2 Sides.	127
VI-88 Total Reconstruction and Error for Four-Region Domain with Sources on 3 Sides.	128
VI-89 Scattering Reconstruction and Error for Four-Region Domain with Sources on 3 Sides.	128

FIGURE		Page
VI-90	Total Reconstruction and Error for Four-Region Domain with Sources on 4 Sides.	128
VI-91	Scattering Reconstruction and Error for Four-Region Domain with Sources on 4 Sides.	129
VI-92	Total Reconstruction and Error Results for the Four-Region Domain with Measurements on 1 Side.	131
VI-93	Scattering Reconstruction and Error Results for the Four-Region Domain with Measurements on 1 Side.	131
VI-94	Total Reconstruction and Error Results for the Four-Region Domain with Measurements on 2 Sides.	132
VI-95	Scattering Reconstruction and Error Results for the Four-Region Domain with Measurements on 2 Sides.	132
VI-96	Total Reconstruction and Error Results for the Four-Region Domain with Measurements on 3 Sides.	133
VI-97	Scattering Reconstruction and Error Results for the Four-Region Domain with Measurements on 3 Sides.	133
VI-98	Total Reconstruction and Error Results for the Four-Region Domain with Measurements on 4 Sides.	133
VI-99	Scattering Reconstruction and Error Results for the Four-Region Domain with Measurements on 4 Sides.	134

CHAPTER I

INTRODUCTION

A. Motivation

A current area of research interest in national security is to effectively and efficiently determine the presence of highly-enriched uranium (HEU) or plutonium in the many shipping containers that enter ports in the United States. This interest comes as a result of the 9/11 Commission Act passed by Congress in 2007 that requires 100% of inbound cargo to be scanned by 2012.¹ It appears that this requirement may not be fully achieved by 2012, but as of February of 2009 eighty percent of the 11.5 million inbound cargo containers were being scanned.²

The systems used today in all major U.S. ports to determine the presence of radioactive material within cargo containers are Radiation Portal Monitors (RPM). These devices generally exist in the form of a gate or series of gates that the containers can be driven through and scanned. The monitors are effective for determining the presence of radiation, but offer little more information about the particular source. This simple pass-fail system leads to many false alarms as many everyday items emit radiation including smoke detectors due to the americium-241 source contained inside, bananas, milk, cocoa powder and lean beef due to the trace amounts of potassium-40,³ and fire brick and kitty litter due to their high clay content which often contains traces of uranium and thorium. In addition, if an illuminating source is imposed on the boundary of the container, the contents of the container may become activated. These materials include steel, aluminum and many agricultural products.³ Current portal

The journal model is *Nuclear Science and Engineering*.

monitors also have not proven to be that effective at identifying natural or highly enriched uranium (HEU). In fact, the best available Advanced Spectroscopic Portal Monitors (ASP) are only capable of identifying bare HEU 70-88 percent of the time and masked HEU and depleted uranium (DU) only 53 percent of the time.⁴ Therefore, a better algorithm that uses more information collected from better detectors about the specific material distribution within the container is desired.

B. Inverse Problems

An inverse problem can be generally defined as a case where one wants to know the values of some unknown quantities, often the material properties of a object, but only has access related quantities.⁵ This relationship between the desired quantities and the related quantities can be modeled by a partial differential equation (PDE). This PDE serves as the basis for the forward model, since the related measurable quantities (the particle flux or count at a detector location, for instance) can be computed from solving the PDE given some yet unknown quantities (again material properties). Therefore, one must successively guess values of the unknown parameters and solve the PDE to obtain values for the measurable quantities. The values of the computed quantities that result from solving the PDE are then compared with the actual observed quantities and sophisticated techniques are used to propose the next guess for the values of these parameters. This process is then repeated until the difference between the observable quantities and the computed quantities is reduced to some acceptable level. These inverse problems can be found in many fields including groundwater flow,^{5,6} DC resistivity,⁶ hydraulic head,⁵ optical tomography,⁵⁻¹⁵ magnetotelluric inversion⁶ and gravity gradiometry.⁵ Optical tomography is the type of inverse problem considered in this thesis.

Since only the values of some related quantities are available at some distance

away from the object of interest, inverse problems are often ill-posed. This means that the observable quantities could arise from an object of many different parameter distributions. Because of this fact, the solution to inverse problems is known to be much more difficult to find than simply solving the forward problem. There are also many factors common to many inverse problems that effect the ability to find the searched parameters. Some of these factors are the number and locations of the measuring devices, the number of separate experiments that are conducted where measurements are collected, the amount of signal noise present in the environment, the amount of signal bias due to the limitations of the measuring device, the initial guess for the parameter distribution, the material properties of the object and any surrounding materials and the magnitude of the measurable signal. Each of these factors that affect the ability to find the solution to the inverse problem will be considered in this thesis.

The specific inverse problem considered in this Thesis is the problem of inverse neutral particle transport through a cargo container. Like many inverse problems, only a measurable quantity of radiation that escapes the container will be used to generate an image of the container. Therefore, when actually implemented, some detection system will be required to collect measurements of the fluxes emitted from the cargo container. Many different detectors can be used in portal monitors such as scintillators such as Sodium Iodide (NaI), High Purity Germanium (HPGe), Polyvinyl Toluene (PVT) for gamma particle detection and gas-filled detectors like Helium-3 (He-3) tubes for neutron detection. These detectors are positioned within the portal monitor on multiple sides of the scanned vehicle to measure the radiation emitted from the boundary of the vehicle. The portal monitors are used to measure the natural radiation that is emitted from the contents of the cargo container passively or the emitted radiation when sources are used to actively illuminate the container by im-

posing neutral particles on different sides and at different angles. Active interrogation will be the focus of this thesis.

Several simplifications will be made in this thesis to lay the ground for a proof-of-principle demonstration. The cargo container problem will be simplified to a study on two-dimensional heterogeneous domains. The external illuminating sources will be imposed on the boundaries of the domains and only the most normal angles determined by the Sn angular quadrature will be used. The number of possible imposed boundary sources and measurement locations considered in this thesis will be equivalent to the dimensions of the material map for the considered domain. Several other assumptions will be made in this thesis to simplify the inverse transport process and they will be presented in the Sections III-A, III-B, IV-A and IV-C.

C. Optimization

In mathematics, a simple optimization process can be defined as a systematic approach to minimize or maximize some real function based on choosing values of parameters from a set of acceptable values. There are many different optimization methods that cater to many different specific problem types. Inverse problems are often difficult, ill-posed optimization problems where convergence cannot be guaranteed. Constraints can be applied to the optimizer to narrow the set of possible parameters that will be proposed. In addition, the more information that is provided in the optimization routine, the faster this process can be conducted. This is why derivative-free methods where the gradient of the objective function is not provided generally perform slower than methods that use the gradient information. However, the faster Newton-based routines that use gradient information can introduce additional convergence problems. For instance, if the gradient of the objective function is very close to zero, then Newton's method can propose a new guess for the parameters

that is very far from the actual minimum and the method can diverge. Both the Nelder-Mead and Newton's methods were explored in this document.

In the case of our problem, the objective or misfit function that is to be minimized is a measure of the difference between the measured boundary angular fluxes as recorded from the detector and the computed angular fluxes as calculated from our model. The computed angular fluxes will be calculated by solving the transport equation iteratively with updated parameters provided by the optimization routine. The formulation of the optimization problem yields systems of nonlinear equations because of the coupling between angular fluxes and cross sections.

D. Outline of Thesis

In Chapter II, a summary of some methods that have been explored with respect to solving the inverse problems of cargo container imaging, optical tomography, applied DC-resistivity and magnetostatics is presented. In Chapter III, the transport equation and adjoint transport equation are presented as the balance equations used to model the transport of radiation through a heterogeneous medium. In Chapter IV, the optimization process is described as well as some of the methods investigated in this document. In Chapter V, the particular optimization problem of inverse neutral particle transport through a cargo container is introduced. This entails establishing the objective function, Lagrangian relationship, the optimality conditions and the Hessian matrix. In Chapter VI, some sample problems are presented that were explored to determine some of the capabilities and limitations of the method. Results from both the derivative-free and Newton based methods are presented in this section. In Chapter VII, conclusions are drawn from the results collected in this study. Suggestions for future research in inverse neutral particle transport applied to cargo container imaging are also made in this section.

CHAPTER II

PREVIOUS WORK

A. Inverse Neutral Particle Transport Related to Cargo Container Imaging

The conservation of neutral particles can be modeled using the transport equation. This neutral particle transport equation is applicable to neutron, gamma and coupled neutron-gamma transport. In this thesis, only neutron transport will be considered, but the model is applicable to other neutral particle transport problems.

The idea of using neutron transport to noninvasively infer the contents of shipping containers is a topic of growing interest for national security reasons. Many researchers in United States are working to solve this challenging problem. Several researchers at Texas A&M University have investigated this topic and three unique approaches to cargo imaging are discussed in the following paragraphs.¹⁶⁻¹⁸

First, the idea of using both transmitted and scattered radiation to reconstruct images of a object was suggested by Scipolo.¹⁶ In the process of using transmitted radiation, the difference between the original beam and the portion of the beam that makes it through an object is used to generate an image of the object. In other words, it is the removal of some percentage of the original beam in some pattern due to scattering and absorption that allows one to generate an image of an object. In scattered radiation, the angle at which the radiation is redirected after an interaction within some object can be used to make inferences about the material properties of the object. A S_n quadrature was used as the basis of the angular discretization and the Step Characteristic (SC) method was used as the spatial discretization scheme. The SC method transforms the angular dependence of the transport equation into

a one dimensional equation by rotating the axis of the coordinate system along the direction of motion. The angular flux at one point along this line and the known source term can be used to solve for the angular flux anywhere along the characteristic line. The effects of uncollided and collided fluxes are then added and angular fluxes within the entire domain can be determined. The inverse models were composed of the steepest decent and conjugate gradient routines. The steepest decent method used the gradient of the objective function to determine the direction that minimizes the objective function. The conjugate gradient method minimizes the residual of the objective function and the direction of the updated guess for the parameters is determined by a linear interpolation between the old direction and the new gradient. Because the angular flux is calculated as a separate combination of the contributions due to uncollided and collided fluxes, the gradient must also be calculated in this manner. This method showed promise in its ability to correctly identify the location and cross sections of inclusion materials within a domain with some degree of error. The method did tend to smear the size and position of the inclusion. This is possibly an artifact of how the SC method calculates the angular fluxes along the characteristic lines.

Sternat¹⁷ suggested to use diffusion theory to approximate neutral particle transport through a medium and constrained optimization to reconstruct the cross sections of two dimensional domains. The chosen optimization technique was Newton's method with the Armijo algorithm applied for step length control. The gradient and Hessian matrix were formed and substitution was used to form the Schur complement to avoid inverting the large Hessian system. The steepest decent method was also employed for comparison sake. The effects of reconstruction depth, resolution and number of experiments was investigated. The number of experiments generally had the effect of reducing the amount of iterations required for the reconstruction process

and increasing the accuracy of the final image. Single energy and multigroup models were studied and signal noise and bias were added to the synthetic measurement data in some of these models to better simulate real detection systems. The method was successful in its ability to reconstruct many domains, but a reconstruction depth limit of 6-7 characteristic lengths was determined. Some multigroup models were considered where energy dependent cross sections were reconstructed using illuminating sources with specific energies. Adding energy dependence, signal bias and noise increased the complexity of the imaging problem and as a result, the size of the domains that could be reconstructed was reduced. Using multiple experiments generally improved image quality in fewer iterations, but a point of diminishing returns was noticed where more experiments added little new information to the reconstruction and image quality showed little improvement.

Wu¹⁸ suggested the idea of assuming a finite library of possible materials within the container. This then allowed for the use of a discrete optimization method where a discrete material indicator was proposed rather than the continuous cross section value. This method also employed a combined deterministic and stochastic methods for simulating neutron transport. First, inexpensive calculations are conducted using a gradient based deterministic search to get a general idea of the domain using a single energy group, a coarse spatial mesh or diffusion theory instead of transport theory. Next, cells that have similar cross sections or material properties are grouped together and interface regions that may contain multiple materials are identified. Third, the materials that possess similar properties to those identified in the initial deterministic search are placed in material candidate libraries. Fourth, additional constraints can be applied to the material regions to limit the candidate materials. Finally, an iterative optimization process is conducted where guesses for the material distributions are proposed and a high resolution transport forward model is used to compute the objec-

tive function. Because the optimization problem has been reformulated into a discrete problem, meaningful derivatives of the objective function can not be computed and a gradient based technique can not be used. Instead, the problem becomes one of combinatorial optimization where random numbers and some information learned from previous guesses are used to generate the new material distribution for the domain. The idea of reformulating the continuous optimization problem of determining cross sections into a discrete one of determining materials from a candidate library proved to be a novel approach to the cargo container imaging problem. However, this method generates a new interface region materials which contain some combination of two or more materials. Of course, these regions do not really exist and the size of these regions is a function of the resolution of the image. This method is also subject to the same limitations of the other techniques with regard to optically thick and highly scattering materials.

B. Radiation Imaging in Medical Physics

Optical tomography is a method of noninvasive diagnostics that is growing in interest in the medical field. In this process light is used to illuminate tissue and measurements are taken of the transmitted and scattered light. Because of the different scattering and absorption coefficients of fat, muscle, white matter, grey matter, etc., measurements of the transmitted and scattered light can be used to reconstruct an image that depicts the tissue sample. This imaging technique shows promise in applications which include breast and brain imaging for the detection of cancers, finger joint imaging for the diagnosis of arthritis and blood toxicology. Many numerical methods have been reviewed that use the photon transport equation as the forward model and some optimization techniques as the inversion method.

Klose⁷⁻⁹ and Hielscher⁷⁻¹² have thoroughly investigated various numerical meth-

ods for imaging in the field of optical tomography. In most of these methods, the equation of radiative transfer (ERT) or transport equation is used as the basis of the forward model.⁷⁻¹¹ In some of these studies^{7,10} the time dependent transport equation was considered, but in most cases the transport equation was simplified by the steady state assumption.^{8,9,11} However, Hielscher and Bartel also proposed the time dependent diffusion equation as the model of light propagation in tissue.¹² The objective function took many different forms in these many studies. In all cases an objective function is formed as a least squares comparison between the measured and computed fluxes and it is used to quantify their difference. However, this least squares term is often normalized in different ways. The objective function is normalized by the measurements or detector readings of each source detector pair,^{8,11} the predicted fluxes for each source detector pair,⁷ a normalization constant that quantifies the confidence in the accuracy of a certain measurement,⁹ or some other constant.¹² Abdoulaev, Ren and Hielscher proposed the addition of a regularization term to the objective function that imposes additional constraints.¹⁰ This Tikhonov regularization functional is included in the objective function to help suppress high-frequency components of the optical properties because of the ill-posedness of the optical tomography problem.

Various different optimization techniques were applied in the studies by Hielscher and Klose. A one-dimensional line search using the golden section rule along the gradient direction was used to minimize the objective function in one paper.⁷ The gradient of the objective function is determined by differentiating the adjoint transport equation which is accomplished by solving the transport equation in the reverse direction. The method displayed image resolution improvement as the number of iterations was increased. The test cases also displayed the trend that increasing the number of sources and the number of measurement points leads to image resolution improvement, but there did exist a point of diminishing returns where more exper-

iments and measurements adds little improvement to quality. Klose and Hielscher propose the use of a quasi-Newton method that uses the secant condition to approximate the Hessian system.⁸ This specific quasi-Newton method is referred to as Broyden-Fletcher-Goldfarb-Shanno method (BFGS) or the limited-memory Broyden-Fletcher-Goldfarb-Shanno (lm-BFGS) and it is used to find the zeros of the gradient of the objective function and the minimum of the objective function. The Armijo or sufficient decrease line search was implemented with the quasi-Newton method to ensure that the method did not overshoot the minimum. The quasi-Newton methods were compared to a conjugate gradient optimization technique and a 2-10 fold reduction in the number of iterations to minimize the objective function was noticed. This was determined to be a result of the better search direction determined in the quasi-Newton method and inexact line search which required fewer evaluations of the forward model. The next method used lm-BFGS to determine the spatial distribution of fluorescent sources contained within biological tissue.⁹ This method was employed along with an adjoint differentiation scheme that allows for the gradient of the objective function to be calculated during the computation of the forward model. This adjoint differentiation technique eliminated the need to evaluate the adjoint transport equation and decreases the number of computational operations. Experiments were conducted with a phantom and the trend of improved image depth resolution was noticed as the sources and detectors were positioned on more sides of the phantom was noticed. The idea of rescaling the measurements was also explored to reduce the likelihood of reconstruction errors created by coarse spatial grids, ray-effects or false scattering.

In a contrasting method, Abdoulaev, Ren and Hielscher¹⁰ use an augmented Lagrangian approach where the inverse transport problem is formulated into a PDE-constrained optimization problem. The new objective is to minimize a Lagrangian

function that is then formed as the difference between the objective function, the constraints and a penalty term that measures how severely that the constraints are violated for the current guess of the optical properties and fluences. The gradient of this now augmented Lagrangian function is then computed to form the Karush-Kuhn-Tucker (KKT) optimality conditions and lm-BFGS is also employed to find the minimizer of the Lagrangian function. This PDE-constrained optimization technique showed a 10-30 fold decrease in computing time as compared with unconstrained optimization techniques and is highly parallelizable.

Another technique used a gradient based optimization technique that uses the lm-BFGS scheme extended to three dimensions.¹¹ Hexahedral and tetrahedral spacial meshes were examined on geometries similar to the human head. The limitations of the current implementation to only consider isotropic scattering was mentioned, but plans to add anisotropy were discussed.

Yet another technique considers two different inverse problems where n tissues types with n different optical properties are known to be contained within a medium.¹² In the first case, the volume fractions and locations of these tissues are unknown prior to the reconstruction, where as in the second case the volumes and tissue types are assumed to be known prior to the reconstruction but not the locations of the tissue types. Penalty factors for the two cases were applied to the objective function and a gradient-based iterative image reconstruction (GIIR) scheme was employed. Generally, the addition of the penalty terms limited the search space of the gradient method and led to improvements in image quality. The sensitivity of the reconstruction method with respect to the chosen hyperparameter was noted and the GIIR method with penalty terms was compared to the linear-perturbation approach.

Bangerth^{5,13} and Joshi¹³ proposed the idea of applying adaptive finite element methods to the solution to inverse problems, with applications to optical tomogra-

phy. In the first paper,⁵ Bangerth outlines a general framework for the solution of inverse problems that utilizes adaptive finite element meshes. This framework formulates inverse problems as PDE-constrained optimization problems where a Newton-type method is to minimize a Lagrangian function comprised of an objective function and its constraints. A Tikhonov regularization term is included in the Lagrangian to suppress unwanted features in the solutions of the forward model and parallelization is considered throughout the optimization process. A line search technique is proposed that uses the norm of the residual of the optimality conditions as the merit function and the Schur complement method is used to avoid the inversion of the large Hessian matrix. This framework was applied to an optical tomography test case and a tumor of a centimeter in diameter was correctly identified and located. In addition, the adaptive mesh technique proved less computationally expensive because of the ability to conduct initial iterations with a coarser mesh. In the second paper,¹³ the specific fluorescence tomography problems were discussed more thoroughly as the process of illuminating a fluorescent dye with red light and the emitted infrared light is measured. The coupled photon diffusion equations were provided as the basis of the forward model. The Lagrangian formulation for the PDE-constrained optimization problem consisted of the least squares error function and Tikhonov regularization term, the constraints on the state equation and the parameter inequalities. A Gauss-Newton method is used where an approximation of the Hessian system is used to determine the search direction for the value of the updates of the parameters. The merit function based line search is then employed to determine an acceptable step length and the Schur complement method is employed to decompose the approximate Hessian matrix. The choice of the regularization functional is more explicitly explained as a function of the material property distribution and the goal reducing the regularization parameter as the misfit decreases was presented. Again, the method proved

capable of imaging a small tumor located in a lymph node in the groin of a Yorkshire Swine. The benefits of the adaptive meshes with respect to the reduction in overall computational time and to increase image resolution in the areas of concern was presented.

Roy and Sevick-Muraca¹⁴ propose an active constrained truncated Newton method for optical tomography. In this method the coupled photon diffusion equations formulated in the frequency domain are solved using Galerkin finite elements in the forward model. The objective function is formed as the summation over all sources and all detectors of the product of the difference between the computed and measured fluxes and their respective complex conjugates. An active constrained method is then employed where the set of optical properties that lie between a lower and upper bound is first determined, then the subproblem of minimizing the objective function with respect to the remaining variables is approached as an unconstrained minimization problem. These upper and lower bounds are determined dynamically and the search space for the parameters is reduced with each iteration. A Newton method with trust region is then used to update the free variables and a line search using both of the Wolfe conditions was employed. Reverse automatic differentiation (RAD) was included in the forward model to calculate the gradient of the error function without the need for an additional sweep. The active constrained Newton method was tested on a few two-dimensional domains and the results were compared with those generated with an unconstrained gradient based method. The active constrained method was more efficient, accurate and less computationally expensive than the unconstrained gradient based technique. This was mainly attributed to the second order nature of the Newton method and the reduction in the search space for the parameters due to the constraints.

Hussein and Bowles¹⁵ propose a method that uses the incoherently scattered ra-

diation in imaging. The forward model is generated on a pixel by pixel basis and is comprised of an attenuation term for the beam before it enters the pixel of interest, a probability term that quantifies the likelihood of scattering and another attenuation term for the scattered beam. This forward model yields a detector response function that allows for duplicity of possible solutions based on whether the dominant interaction process is scattering or attenuation. Therefore, a numerical scheme for biasing the solution towards the dominant process is included to overcome this problem of multiple solutions. The source term in each pixel is then calculated in a sweeping manner along the source beam to the pixel of interest and then along the scattered direction to the measurement point. The imaging algorithm was tested on meter scale cargo containers where the detection of weapons was the goal. The reconstruction scheme using scattering radiation and the contraction method proved successful in reconstructing the many test cases examined. The scaling procedure used to modify the measurements improved the conditioning of the problem to allow for the reconstruction of noisy systems without further constraints or regularization. It also permitted the imaging of low density materials and thin objects and the method to be less sensitive to initial guesses.

C. Imaging Applied to DC-Resistivity and Magnetostatics

Haber and Ascher⁶ suggest formulating the inverse problem as a constrained optimization problem where a preconditioner can be applied directly to the optimality conditions derived from a Newton-type method. The objective function is formed as the sum of the least squares difference and the Tikhonov regularization term. The Lagrangian is then formed as the sum of the objective function and the product of the constraints and the Lagrange multiplier. The KKT system is then calculated as the first and second partial derivatives of the Lagrangian. The Hessian system is

then permuted so that the blocks on the diagonal of the matrix dominate and a reduced Hessian is computed by decomposing the larger system. A preconditioner that approximates the inverse of the large permuted Hessian system is then used to avoid the computationally expensive inversion process. The suggested method was tested on DC-resistivity and magnetostatic problems. In both cases the proposed preconditioned symmetric quasi-minimal residual (PSQMR) method was compared to a preconditioned conjugate gradient (PCG) method. The number of iterations and the total number of floating point operations were used as metrics for the performance of the method. Generally, the PSQMR method required more iterations, but less floating point operations per iteration than the PCG method. The main advantage noticed by the PSQMR method was the elimination of the need to maintain conjugacy of the direction vectors to a high accuracy when using the conjugate gradient method.

CHAPTER III

TRANSPORT THEORY

A. Balance Equation

The behavior of a neutron population within some differential volume of interest can be described by the neutron transport equation whose unknown quantity is the angular flux. Neutrons are produced or removed from a system in several ways and these processes can be described in a balance equation or Eq. (3.1):¹⁹

$$\begin{aligned} \frac{1}{v(E)} \frac{\partial \psi(\vec{r}, E, \vec{\Omega}, t)}{\partial t} = & -\vec{\Omega} \cdot \vec{\nabla} \psi(\vec{r}, E, \vec{\Omega}, t) - \Sigma_t(\vec{r}, E) \psi(\vec{r}, E, \vec{\Omega}, t) + \\ & \int_0^{+\infty} dE' \int_{4\pi} d\Omega' \Sigma_s(\vec{r}, E' \rightarrow E, \vec{\Omega}' \rightarrow \vec{\Omega}) \psi(\vec{r}, E', \vec{\Omega}', t) + \\ & S(\vec{r}, E, \vec{\Omega}, t) \end{aligned} \quad (3.1)$$

Here, the term with the time derivative represents the change in the angular flux with respect to time. In this study of the cargo container imaging, the neutron population is assumed to be at steady state and this term in the neutron transport equation is zero. The second and third terms of Eq. (3.1) represent the mechanisms by which neutrons can be removed from a specific direction and energy group within a specific differential volume across a specific time interval. These loss terms represent how neutrons are removed due to streaming through and interaction within the differential volume. In imaging, the leakage term is important because of the ability to measure the leaked neutrons that exit the boundary of the domain. The fourth and fifth terms of Eq. (3.1) represents the mechanisms by which neutrons are introduced into the differential phase-space. These mechanisms are due to scattering within the

system and internal sources. Internal sources are especially interesting in cargo container imaging because the presence of internal sources will indicate whether or not SNM is confined within a container. This thesis will only consider a single energy group analysis, the dependence of all of the terms on energy can also be removed. Now that we have applied some simplifying assumptions to the neutron transport equation, Eq. (3.2) results:

$$\vec{\Omega} \cdot \vec{\nabla} \psi(\vec{r}, \vec{\Omega}) + \Sigma_t(\vec{r}) \psi(\vec{r}, \vec{\Omega}) = \int_{4\pi} d\vec{\Omega}' \Sigma_s(\vec{r}, \vec{\Omega}' \rightarrow \vec{\Omega}) \psi(\vec{r}, \vec{\Omega}') + S(\vec{r}, \vec{\Omega}) \text{ for } \vec{r} \in V, \vec{\Omega} \in S^2 \quad (3.2)$$

In addition, it is important to remember that the source term of Eq. (3.2) can include internal sources due to fissionable material or other internal sources contained within the differential volume. However, no fissionable materials were considered in this thesis. In the cargo imaging problem, illuminating sources are often imposed on the boundary of the domain to determine the contents of the domain. The boundary conditions that describe these illuminating sources are given in Eq. (3.3):

$$\psi(\vec{r}, \vec{\Omega}) = \psi^{inc}(\vec{r}, \vec{\Omega}) \text{ for } \begin{cases} \vec{r} \in \partial V \\ \vec{\Omega} \cdot \vec{n}(\vec{r}) < 0 \end{cases} \quad (3.3)$$

Here, $\psi^{inc}(\vec{r}, \vec{\Omega})$ is the angular flux imposed on the domain from an illuminating source such as a neutron source from an x-ray generator. Eq. (3.2) can then be written in matrix form to better represent the system of linear equations that results as the equations are discretized with respect to space and angle:

$$\mathbf{A}\Psi = \mathbf{q} \quad (3.4)$$

This discretized operator, \mathbf{A} , seen in Eq. (3.4), is referred to as the transport operator. This transport operator is formed as the difference between the loss and scattering matrices. \mathbf{q} is the source term that contains the contributions to the neutral particle fluxes due to internal volumetric and boundary sources.

B. Adjoint Transport Equation

The adjoint transport equation serves as the basis of the backward model. By solving the adjoint equation, the Lagrange multipliers or importance function can be determined. Obtaining this importance function is crucial to solving the constrained optimization problem. The adjoint transport equation is given in Eq. (3.5):

$$\mathbf{A}^\dagger \Psi^\dagger = \mathbf{q}^\dagger \quad (3.5)$$

Here, Ψ^\dagger is the adjoint angular flux, \mathbf{q}^\dagger is the adjoint source term and \mathbf{A}^\dagger is the adjoint transport operator. Since the \mathbf{A} matrix is comprised of only real-valued quantities, the adjoint matrix \mathbf{A}^\dagger is equivalent to the transpose of the \mathbf{A} matrix or \mathbf{A}^T . Eq. (3.5) determines how important a given source distribution is. In the remainder of this thesis, Ψ^\dagger will be denoted as λ , the Lagrange multiplier, for consistency with the notation used in the optimization literature. The adjoint source, \mathbf{q}^\dagger , will be determined by the optimality conditions for the optimization problem.

CHAPTER IV

OPTIMIZATION TECHNIQUES

A. Overview

Optimization is the process of deciding which is the best choice from a set of choices. Optimization involves minimizing some real valued cost function by systematically choosing real valued parameters from a set of allowable values. Optimization is a large field in applied mathematics with many different iterative approaches to achieve the final solution parameters. The best optimization algorithm depends on the specific problem being solved and the trade-offs between robustness, efficiency and accuracy of each method.

The general form of an optimization problem can be formulated as the minimization relationship seen in Eq. (4.1):²⁰

$$\min_{x \in R^n} f(x) \tag{4.1}$$

Here, x is the vector of variables or parameters, $f(x)$ is the scalar objective function or misfit that we want to minimize and R^n is the set of all possible real numbers to which the parameters belong. Based on knowledge of the problem or physical system that is being modeled, often times the searchable space for the parameters can be reduced to some subset of R^n . This reduction in the searchable space is accomplished through the application of constraints to the optimization process. The general form of a constrained optimization problem can be seen in Eq. (4.2):²⁰

$$\min_{x \in \mathbb{R}^n} f(x) \text{ subject to } \begin{cases} c_i(x) = 0, i \in \mathcal{E} \\ c_i(x) \geq 0, i \in \mathcal{I} \end{cases} \quad (4.2)$$

Here, $c_i(x)$ is the equality or inequality constraint imposed on $f(x)$, i is the index of the constraint, \mathcal{E} is the set of all equality constraints and \mathcal{I} is the set of all inequality constraints imposed on the minimization problem.

There are various classifications of problems that are encountered in engineering applications that govern which optimization techniques are best suited for the problem. First, optimization problems can be constrained or unconstrained as evidenced by Eq. (4.2). Constrained optimization problems have limitations that are imposed on the objective function or parameters to limit the number of possible solutions. For example, the parameters of cargo container domain represent the cross sections of the materials contained within the container. Since a negative cross section has no physical meaning, a logical constraint on this optimization problem would be to limit the possible parameters that the optimizer could propose to values greater than or equal to zero. Unconstrained optimization problems do not propose any limitations on the solution process. Generally, the more information that can be provided to the optimization routine, the more accurate and efficient the routine can be. However, the algorithms used in constrained optimization problems are generally much more complex than those for unconstrained techniques and require more computations to determine the next update for the parameters. The cargo container problem can be approached as either a constrained or unconstrained optimization problem. Second, optimization problems can be discrete or continuous. This classification can also be thought of as a constraint that is imposed on the solution parameters. The cargo container problem is a continuous optimization problem because cross sections are positive real valued numbers and are not limited to some discrete set. Third,

optimization problems can be stochastic or deterministic. This classification of the problems is rooted in the model that is used to represent the problem. Transport theory as presented in this document is deterministically modeled, but similar processes in particle physics can be stochastically modeled as well.

Just as there are many different classifications of optimization problems, there are also many different optimization algorithms or methods used to achieve the solution. These methods are all iterative, but they differ in the amount of information they require to achieve the solution. All optimization routines make use of the objective function and any constraints that exist to arrive at the solution parameters. Some optimization routines make use of the first and second derivatives of the objective function and constraints to solve the problem. Newton based methods generally require first and second derivative information, where as derivative-free methods do not. Derivative-free methods are applicable to a wider variety of optimization problems and require less computer storage, but require more computational time. Newton methods require less computational time, but also require more computer storage and are specific to problems where derivative information is accessible. Two methods are investigated in this document. The first is the Nelder-Mead method, a derivative-free method. The second is a Newton based method.

B. Nelder-Mead Method

The Nelder-Mead algorithm²¹ for function minimization is an unconstrained, derivative-free optimization technique. It works by evaluating an objective function of n variables by creating a simplex of $n+1$ vertices. The objective function is then evaluated for each of the combination of variables that form the vertices of the simplex, and the combination of these variables that leads to the largest and smallest value of the objective function, x_h and x_l , are stored. Three operations are then performed based

on this largest value of the objective function which are reflection, expansion and contraction. In reflection, the centroid of the simplex defined by all of the vertices except the one with the largest objective function value, \bar{x} , is calculated. The vertex with the largest value is then reflected across the centroid using Eq. (4.3):

$$x^* = (1 + \alpha)\bar{x} - \alpha x_h \quad (4.3)$$

Here, α is a positive constant known as the reflection coefficient. The objective function is then evaluated at this new reflection point and if the resulting value lies between the maximum and minimum values of the original simplex, then this new point replaces x_h and a new simplex is formed. However, if this reflection point yields a value of the objective function which is new minimum, then an expansion can be conducted to determine the amplification of magnitude of the reflection point based on Eq. (4.4):

$$x^{**} = \gamma x^* + (1 - \gamma)\bar{x} \quad (4.4)$$

Here, γ is a real number greater than one which is calculated based on the ratio of the distance from the centroid to the expanded point, x^{**} , to the distance from the centroid to the reflected point, x^* . Once the new expanded point has been determined, the objective function is evaluated at this point. If the evaluation of the expanded point is the new minimum, then the new simplex is formed by replacing x_h by x^{**} . Otherwise, the new simplex is formed by replacing x_h by x^* . In the last case where the objective function evaluated at the reflected point is larger than that of x_h , a contraction occurs described by Eq. (4.5):

$$x^{**} = \beta x_h + (1 - \beta)\bar{x} \quad (4.5)$$

Here, β is a real number between zero and one which is calculated based on the ratio of the distance from the centroid to the contracted point, x^{**} , to the distance from the centroid to the original point, x_h . In the contraction process, the value of the objective function evaluated at the initial point is compared with that of the reflected point and the larger of the two is redefined as x_h . If the contracted point yields an objective function that is greater than that associated with either the reflected or original points, then all of the original simplex vertices are averaged with x_l to generate the new simplex. Otherwise, the contracted point replaces x_h to form the next simplex.

The Nelder-Mead algorithm is a robust algorithm that is only capable of finding local minima. It only requires the evaluation of the objective function, which makes it applicable to optimization problems where the objective function is non-differentiable. It is also a very stable method that generally does not propose outrageous values for the parameters, because the gradient is not used to propose new guesses for the parameters. However, because only the objective function is evaluated, the method requires many iterations and much computational time to locate the solution.

C. Newton's Method

In optimization problems, Newton-based methods require the gradient and Hessian system to be calculated in order to generate an updated prediction of the parameters. Newton methods generally converge to the solution more rapidly than derivative free methods, but they are less reliable and do not guarantee convergence unless considered with a line search. In this thesis, the inverse neutral particle transport

problem is tackled with Newton's method as a constrained optimization problem. In this constrained optimization problem, prior knowledge about neutral particle physics is applied to the objective function in the form of a constraint. Only one equality constraint will be applied to the objective function in this thesis even though other constraints could be applied. Because of this, Eq. (4.2) can be simplified to consider only equality constraints and the general formulation of the constrained optimization problem becomes Eq. (4.6):

$$\min_{x \in \Omega} f(x) \text{ where } \Omega = \{x | c_i(x) = 0, i \in \mathcal{E}\} \quad (4.6)$$

Here, Ω is the acceptable domain space of possible parameter combinations defined by the set of imposed equality constraints, \mathcal{E} . In the case of the inverse neutral particle transport problem, a set of equality constraints is applied to the optimization problem that ensures that the transport equation is satisfied for every angular flux at every angle and spatial coordinate. A relationship known as the Lagrangian functional can be defined as the combination of the objective function and its constraints or Eq. (4.7):

$$\mathcal{L}(x, \lambda) = \mathcal{L}(\Sigma, \Psi, \lambda) = f(\Sigma, \Psi) + \sum_{i \in \mathcal{E}} \lambda_i c_i(\Sigma, \Psi) \quad (4.7)$$

Here, λ_i is the importance factor and \mathcal{L} is the Lagrangian. Also, it can be seen that the objective function is only dependent on x which is comprised of the set of total cross sections, Σ_t , scattering cross sections, Σ_s , and angular fluxes Ψ , where as the Lagrangian is dependent on both x and λ . This evidences the fact that the objective function requires only the evaluation of the forward model or transport equation and the Lagrangian requires this computation plus the evaluation of the backward model

or adjoint transport equation. This is because the Lagrangian function required that the Lagrange multipliers, λ_i , be computed. These Lagrange multipliers track the neutral particles in the reverse direction and they contain information about the neutron importance with respect to the imposed sources.

1. Gradient and Hessian System

Now that the constrained optimization problem has been presented, the gradient and Hessian systems can be computed as the first and second partial derivatives of the Lagrangian function with respect to the coupled independent variables. In inverse problems, these variables are generally the input and output variables of physical model and importances or adjoint variables. The specific independent variables of the inverse neutral particle transport problem are presented in the next section of this thesis. Since the goal of the minimization process is to determine the minimum of the objective function while still satisfying the constraints, the value of the gradient of the Lagrangian function at this minimum is zero or $\vec{\nabla}\mathcal{L} = 0$. Therefore, the gradient of the Lagrangian function, also known as the Karush - Kuhn - Tacker (KKT) optimality conditions¹⁰ seen in Eq. (4.8), results:

$$\mathbf{F}(\mathbf{y}) = \begin{pmatrix} \frac{\partial \mathcal{L}}{\partial x} \\ \frac{\partial \mathcal{L}}{\partial \lambda} \end{pmatrix} = \begin{pmatrix} 0 \\ \vdots \\ 0 \end{pmatrix} \quad (4.8)$$

Here, x again represents the input and output variables of the transport model, λ represents the importances or adjoint variables and \mathbf{y} is one vector that combines both x and λ . And again, it is desired to determine the point where the gradient of the objective function is equal to zero. In the case of the inverse transport problem of

cargo container imaging, the determining where the gradient of the objective function is zero is a nonlinear problem. Then Newton's method is used to solve this nonlinear problem. Newton's method require the computation of the derivative of the gradient of the Lagrangian function or the second derivative of the Lagrangian. This set of all the second derivatives of the Lagrangian or the Hessian operator can then be computed as the second derivative of the Lagrangian with respect to each the variables and importances or Eq. (4.9):

$$\mathbf{H} = \begin{pmatrix} \partial_{xx}\mathcal{L} & \partial_{\lambda x}\mathcal{L} \\ \partial_{x\lambda}\mathcal{L} & \partial_{\lambda\lambda}\mathcal{L} \end{pmatrix} \quad (4.9)$$

Now that the gradient and Hessian terms have been presented, update values for the parameters of interest can be computed. These parameters of interest now include both the input and output variables of the transport model, x , and the importances or adjoint variables, λ . So a new vector $\delta\mathbf{y}$ is introduced as a update vector that contains all of the variables and importances and the general equation that is solved in Newton's method to calculate this update vector is Eq. (4.10):

$$\delta\mathbf{y} = -\mathbf{H}^{-1}\mathbf{F}(\mathbf{y}^k) \quad (4.10)$$

Here, \mathbf{H} is the Hessian matrix and \mathbf{F} is the gradient vector. The change in the vector of variables can then be used to update the vector of variables or Eq. (4.11) where \mathbf{k} represents the Newton iteration index:

$$\mathbf{y}^{k+1} = \mathbf{y}^k + \delta\mathbf{y} \quad (4.11)$$

Newton's method is iterated until $\|\mathbf{F}(\mathbf{y}^k)\| < \epsilon$, where ϵ is a user-defined tolerance.

2. Schur Complement

The Schur Complement is a technique that recognizes that the Hessian system seen in Eq. (4.9) is composed of multiple smaller matrices or blocks and uses substitution to solve for each of the updated unknowns that are contained in $\delta\mathbf{y}$ individually. This method is less computationally expensive because it requires that matrices only as large as the blocks of the Hessian be stored and inverted as opposed to storing and inverting the full Hessian matrix. The Schur complement method can be implemented on any linear system that consists of blocks.

3. Line Search

When using Newton's method, it is common to use a line search method to determine an acceptable step length or fraction of the update direction vector to apply to the vector of parameters. This is done because using the full Newton step length can lead to divergence especially when the initial guess is far from the solution and the objective function has a minimum that is difficult to locate. Divergence can occur because often, a full step in the update direction can stride beyond the minimum and this can yield a worse guess than in the previous iteration. The general equation that displays how the parameters are updated in Newton's method with the additional damping parameter, α , can be seen in Eq. (4.12):

$$\mathbf{y}^{k+1} = \mathbf{y}^k + \alpha^k \delta\mathbf{y}^k \quad (4.12)$$

The goal of the line search is solely to determine an acceptable value for this

damping parameter that yields an improved guess for the parameters. This damping parameter is generally determined by computing two conditions. These two conditions are collectively referred to as the Wolfe conditions. Separately, the first condition is referred to as the sufficient decrease or Armijo condition and the second condition is referred to as the curvature condition. Both of these conditions are more fully explained in the following sections. In practice, an initial value for α of unity is attempted first and the two conditions are checked. If these conditions are satisfied, then the current step length is accepted, otherwise then value of alpha is reduced and the conditions are recomputed. This process is repeated until the conditions are satisfied or some minimum step length specified by the developer is achieved. This minimum step length was chosen to be 10^{-3} and the step length was reduced by a constant 1.5 with every iteration for this thesis. These values were chosen because the value of the objective function changes only minimally with each successive guess when a step size of this magnitude is applied and 1.5 was chosen because reducing the step size by half each time was thought to reduce it too rapidly.

a. Sufficient Decrease Condition

The sufficient decrease condition evaluates a merit function, often chose to be the objective function, and gradient at the current Newton iteration and compares these values with the merit function evaluated at the next iteration as seen in Eq. (4.13):

$$\phi(\mathbf{y}_k + \alpha \delta \mathbf{y}) \leq \phi(\mathbf{y}_k) + c_1 \alpha \nabla \phi(\mathbf{y}_k)^T \delta \mathbf{y} \quad (4.13)$$

Here, $\phi(\mathbf{y}_k + \alpha \delta \mathbf{y})$ is the merit function evaluated at the possible next Newton step, $\phi(\mathbf{y}_k)$ is the merit function evaluated at the current Newton step, c_1 is a constant that was set to 10^{-4} in the results in this thesis, α is the fraction of the update direction

vector to be added to the current Newton iteration, $\delta\mathbf{y}$ is the update direction vector and $\nabla\phi(\mathbf{y}_k)^T$ is the transpose of the gradient of the merit function evaluated at the current Newton iteration. The sufficient decrease condition ensures that the value of the merit function has been sufficiently reduced between successive iterations.

b. Curvature Condition

The curvature condition evaluates the gradient at the current Newton iteration and compares it with the gradient of the merit function evaluated at the next iteration as seen in Eq. (4.14):

$$\nabla\phi(\mathbf{y}_k+\alpha\delta\mathbf{y})^T\delta\mathbf{y} \geq c_2\nabla\phi(\mathbf{y}_k)^T\delta\mathbf{y} \quad (4.14)$$

Here, $\nabla\phi(\mathbf{y}_k+\alpha\delta\mathbf{y})^T$ is the gradient of the merit function evaluated at the possible next Newton step and c_2 is a constant that was set to 0.9 in the results in this thesis. The curvature condition ensures that the slope of the merit function has been sufficiently reduced between successive iterations. Satisfying both of these conditions generally implies that the updated parameters represent a better approximation of the true parameters.

Both the sufficient decrease and curvature conditions served as the basis of the line search used for all of the test cases explored in this thesis except for in Example 14 or the optical thickness study with scattering. These two conditions were applied to Newton's method because they are a common line search that is often used to ensure that Newton's method does not overshoot the solution parameters.

c. Additional Checks

A negative cross section backtrack method was also applied that allowed the minimum step length value to be 10^{-4} so that Newton's method would be less likely to propose negative values for the cross sections. Along these same line of thought, a backtrack was also applied that reduced the step length if the proposed scattering cross section was larger than the proposed total cross section for any region. This check also allowed the step length to be reduced to values less than 10^{-4} .

CHAPTER V

INVERSE TRANSPORT PROBLEM

A. Objective Function

In the case of noninvasive cargo container imaging, the only available data are outgoing angular flux measurements. Therefore, the model of radiation transport is used to make predictions for these outgoing angular fluxes and a metric to quantify the difference between the computed and measured fluxes is required. This measure of the difference between the computed and measured angular fluxes is the objective function or misfit. This function is generally computed using a least squares technique where the difference between the measured and computed fluxes is squared to treat positive and negative flux differences equally. All of the squared flux differences are then summed and then divided by two to yield a single value for the objective function. Reducing the magnitude of this value should lead to a better material map and is the basis for most optimization techniques. The expression that describes the misfit in the inverse transport problem is given in Eq. (5.1):

$$f = \frac{1}{2} \int_{\partial V^m} d^2r \int_{\vec{\Omega} \cdot \vec{n} > 0} d\vec{\Omega} |\vec{\Omega} \cdot \vec{n}| \left(\psi(\vec{r}, \vec{\Omega}) - \tilde{\psi}(\vec{r}, \vec{\Omega}) \right)^2 \quad (5.1)$$

Here, f is the objective function, ∂V^m is the subset of the cargo boundary where measurements are taken, \vec{n} the outward normal unit vector, ψ is the computed angular flux and $\tilde{\psi}$ is the measured angular flux. This misfit function written in discrete notation in Eq. (5.2) will serve as the metric to determine the quality of the material map at every iteration for every simulation studied in this Thesis:

$$\Delta = \frac{1}{2}(\Psi - \tilde{\Psi})^T \mathbf{M}(\Psi - \tilde{\Psi}) \quad (5.2)$$

Here, $\tilde{\Psi}$ and Ψ are the vectors of measured and computed angular fluxes for every spatial coordinate, angle and energy group, respectively. The matrix \mathbf{M} is a filtering matrix that only extracts the outgoing angular fluxes that lie on the boundary where measurements were taken. This is done again because for noninvasive imaging, the only measurements that are accessible lie on some portion of the boundary.

B. Formulation of Lagrangian

As discussed in the section on optimization, the Lagrangian function is comprised of the objective function and its constraints. In this inverse transport problem, the only constraint that is applied to the objective function is that the proposed cross sections must produce angular fluxes that satisfy the transport equation. The Lagrangian is defined by Eq. (5.3):

$$\mathcal{L}(\Psi, \lambda, \Sigma) = \frac{1}{2}(\Psi - \tilde{\Psi})^T \mathbf{M}(\Psi - \tilde{\Psi}) + \lambda^T (\mathbf{A}\Psi - \mathbf{q}) \quad (5.3)$$

Here, λ is the importance function or the adjoint angular flux vector, \mathbf{A} is the transport operator and \mathbf{q} is the external volumetric and surface source terms of the transport equation. Σ is the vector of parameters or cross sections and this term can be found within the transport operator, \mathbf{A} . Again, in order to minimize the Lagrangian, the transport equation, $(\mathbf{A}\Psi - \mathbf{q} = \mathbf{0})$, must be fulfilled.

C. Optimality Conditions

The optimality conditions form the gradient or first derivative of the Lagrangian with respect to the vector of angular fluxes, the vector of adjoint fluxes and the vector of cross sections. These optimality conditions determine the direction of the steepest ascent of the Lagrangian function and the location of the minimum of the Lagrangian will be found when all these conditions are zero. When the derivative of the Lagrangian functional is taken with respect to the variable vectors, a dimension is added and the optimality conditions are vector quantities. The derivative of the Lagrangian with respect to the vector of angular fluxes is Eq. (5.4):

$$\frac{\partial \mathcal{L}}{\partial \Psi} = \mathbf{M}(\Psi - \tilde{\Psi}) + \mathbf{A}^T \lambda = \begin{pmatrix} 0 \\ \vdots \\ 0 \end{pmatrix} \quad (5.4)$$

Here, it can be noted that the filtering matrix, \mathbf{M} , and the adjoint transport operator matrix, \mathbf{A}^T , are present. Conventionally, the variable vectors of the Lagrangian equation and the optimality conditions are presented as column vectors. In this term, the filtering matrix extracts the measured flux differences and the result is summed with the transport operator which models all the radiation interaction processes weighted according to their computed importances. This term represents the gradient of the objective function and the constraints with respect to the angular fluxes. It is also important to note that the flux difference at the boundary, $\mathbf{M}(\Psi - \tilde{\Psi})$, is the adjoint source term in this adjoint problem. The derivative of the Lagrangian with respect to the vector of adjoint angular fluxes is Eq. (5.5):

$$\frac{\partial \mathcal{L}}{\partial \lambda} = \mathbf{A} \Psi - \mathbf{q} = \begin{pmatrix} 0 \\ \vdots \\ 0 \end{pmatrix} \quad (5.5)$$

When the derivative of the Lagrangian is taken with respect to the importance function, the result is the transport equation. This result is true for all optimization problems. The derivative of the Lagrangian with respect to the vector of cross sections is Eq. (5.6):

$$\frac{\partial \mathcal{L}}{\partial \Sigma} = \lambda^T \frac{\partial \mathbf{A}}{\partial \Sigma} \Psi = \begin{pmatrix} 0 \\ \vdots \\ 0 \end{pmatrix} \quad (5.6)$$

The only place that the cross sections are found in the Lagrangian are in the transport operator. Therefore, the derivative of the transport operator matrix with respect to the vector of cross sections yields a three dimensional tensor or a vector of two dimensional matrices. In other words, there should exist a collection of N matrices based on the number of cross sections each with a row dimension with a length equivalent to the length of the importance function and a column dimension with a length equivalent to the length of the angular flux vector. In this term, the contribution to the transport equation constraint attributed to each reconstructed cross section is isolated in the $\frac{\partial \mathbf{A}}{\partial \Sigma}$ term. In summary, the full gradient vector, \mathbf{F} , is Eq. (5.7):

$$\mathbf{F} = \begin{pmatrix} \mathbf{M}(\Psi - \tilde{\Psi}) + \mathbf{A}^T \lambda \\ \mathbf{A}\Psi - \mathbf{q} \\ \lambda^T \partial_{\Sigma} \mathbf{A}\Psi \end{pmatrix} \quad (5.7)$$

D. Hessian Matrix

Newton's method requires the formulation of the Hessian matrix, \mathbf{H} , in addition to the gradient of the Lagrangian function. The requirement is because the $\vec{\nabla} \mathcal{L} = \vec{0}$ is a nonlinear problems that must be solved with an iterative method. The optimality conditions form a nonlinear problem because in each term a product of the variables of the linear system or their derivatives can be found. Therefore, a root finding method is needed to solve this nonlinear system and Newton's method was chosen because of the low computational time and number of iterations required to find the solution. The Hessian matrix is formulated by taking a derivative of the optimality conditions with respect to the angular flux, adjoint flux and cross section vectors. In other words, this large matrix represents all of the combinations of the second partial derivative of the Lagrangian equation with respect to each of the variable vectors or Eq. (5.8):

$$\mathbf{H} = \begin{pmatrix} \partial_{\Psi\Psi} \mathcal{L} & \partial_{\lambda\Psi} \mathcal{L} & \partial_{\Sigma\Psi} \mathcal{L} \\ \partial_{\Psi\lambda} \mathcal{L} & \partial_{\lambda\lambda} \mathcal{L} & \partial_{\Sigma\lambda} \mathcal{L} \\ \partial_{\Psi\Sigma} \mathcal{L} & \partial_{\lambda\Sigma} \mathcal{L} & \partial_{\Sigma\Sigma} \mathcal{L} \end{pmatrix} \quad (5.8)$$

Here, the rows of the Hessian represent each of the optimality conditions and all have the same first derivatives. The columns of the Hessian represent the process of taking the derivative of the optimality conditions with respect to each of the variable vectors and all have the same second derivatives. From looking at this matrix, we

can predict that the Hessian matrix should be symmetric because the below diagonal derivatives are the same as the above diagonal derivatives taken in the opposite order. The results of evaluating the derivatives of the Lagrangian for the inverse transport problem are provided in Eq. (5.9):

$$\mathbf{H} = \begin{pmatrix} \mathbf{M} & \mathbf{A}^T & \partial_{\Sigma} \mathbf{A}^T \lambda \\ \mathbf{A} & \mathbf{0} & \partial_{\Sigma} \mathbf{A} \Psi \\ \lambda^T \partial_{\Sigma} \mathbf{A} & \Psi^T \partial_{\Sigma} \mathbf{A}^T & \mathbf{0} \end{pmatrix} \quad (5.9)$$

This equation does display symmetry where the below diagonal sub-matrices are simply the transposes of the above diagonal sub-matrices. Because of the ambiguity associated with taking the transpose of a vector of matrices for the $\partial_{\Sigma} \mathbf{A}^T$ term, the matrix has been rewritten and given indices in Eq. (5.10):

$$\mathbf{H} = \begin{pmatrix} \mathbf{M}_{i,j} & \mathbf{A}_{j,i} & \sum_j \left(\frac{\partial}{\partial \Sigma_k} \mathbf{A}_{j,i} \right) \lambda_j \\ \mathbf{A}_{i,j} & \mathbf{0}_{i,j} & \sum_i \left(\frac{\partial}{\partial \Sigma_k} \mathbf{A}_{i,j} \right) \Psi_i \\ \sum_j \lambda_j^T \left(\frac{\partial}{\partial \Sigma_k} \mathbf{A}_{i,j} \right) & \sum_i \Psi_i^T \left(\frac{\partial}{\partial \Sigma_k} \mathbf{A}_{j,i} \right) & \mathbf{0}_{k,k} \end{pmatrix} \quad (5.10)$$

Here, the index, i , corresponds to the index of the angular flux vector, the index, j , corresponds to the index of the adjoint flux vector and the index, k , corresponds to the parameter vector. The transpose of the transport operator simply swaps the indices of this two dimensional matrix. The product of a flux and the partial derivative of the transport matrix with respect to the vector of cross sections can be clearly represented as the dot product of the flux and the partial of the transport operator over the flux index represented in summation notation as shown in Eq. (5.10). The system of equations that is solved in Newton's method can be seen in Eq. (5.11):

$$\begin{pmatrix} \mathbf{M} & \mathbf{A}^T & \partial_\Sigma \mathbf{A}^T \lambda \\ \mathbf{A} & \mathbf{0} & \partial_\Sigma \mathbf{A} \Psi \\ \lambda^T \partial_\Sigma \mathbf{A} & \Psi^T \partial_\Sigma \mathbf{A}^T & \mathbf{0} \end{pmatrix} \begin{pmatrix} \delta \Psi \\ \delta \lambda \\ \delta \Sigma \end{pmatrix} = - \begin{pmatrix} \mathbf{M}(\Psi - \tilde{\Psi}) + \mathbf{A}^T \lambda \\ \mathbf{A} \Psi - \mathbf{q} \\ \lambda^T \partial_\Sigma \mathbf{A} \Psi \end{pmatrix} \quad (5.11)$$

E. Schur Complement Method

Newton's method requires building and inverting the large Hessian system. This process can require large amounts of memory and computational time. The Schur complement of the Hessian system was found to alleviate some of these memory and time problems. The Schur complement method simply recognizes that the Hessian system is block diagonal and it uses substitution to solve for the change in each of the variables of the nonlinear system independently. This process gains a computational edge over solving the Hessian system, because the transport operator is the largest matrix that is formed which alleviates some of the memory problems of building the full Hessian. This Schur complement still requires the transport operator to be inverted several times, but since the full Hessian does not need to be inverted, this method still saves computational time. Based on Eq. (5.11), the Hessian system can be deconstructed into three basic equations. The quantity that we desire to update first is the cross sections, so substitution will be used to eliminate the $\delta \Psi$ and $\delta \lambda$ from (5.11). Evaluating the second row of the Hessian matrix yields Eq. (5.12):

$$\mathbf{A} \delta \Psi + \partial_\Sigma \mathbf{A} \Psi \delta \Sigma = \mathbf{q} - \mathbf{A} \Psi \quad (5.12)$$

Solving this equation for $\delta \Psi$, Eq. (5.13) result:

$$\delta\mathbf{\Psi} = \mathbf{A}^{-1}(\mathbf{q} - \mathbf{A}\mathbf{\Psi} - \partial_{\Sigma}\mathbf{A}\mathbf{\Psi}\delta\Sigma) \quad (5.13)$$

Evaluating the first row of the Hessian system, Eq. (5.14) results:

$$\mathbf{M}\delta\mathbf{\Psi} + \mathbf{A}^T\delta\lambda + \partial_{\Sigma}\mathbf{A}\lambda\delta\Sigma = -\mathbf{M}(\mathbf{\Psi} - \tilde{\mathbf{\Psi}}) - \mathbf{A}^T\lambda \quad (5.14)$$

Solving this equation for $\delta\lambda$, Eq. (5.15) results:

$$\delta\lambda = \mathbf{A}^{-T}(-\mathbf{M}(\mathbf{\Psi} - \tilde{\mathbf{\Psi}}) - \mathbf{A}^T\lambda - \mathbf{M}\delta\mathbf{\Psi} - \partial_{\Sigma}\mathbf{A}\lambda\delta\Sigma) \quad (5.15)$$

Eq. (5.13) can be substituted into Eq. (5.15) and Eq. (5.16) results:

$$\delta\lambda = \mathbf{A}^{-T}(-\mathbf{M}(\mathbf{\Psi} - \tilde{\mathbf{\Psi}}) - \mathbf{A}^T\lambda - \mathbf{M}\mathbf{A}^{-1}(\mathbf{q} - \mathbf{A}\mathbf{\Psi} - \partial_{\Sigma}\mathbf{A}\mathbf{\Psi}\delta\Sigma) - \partial_{\Sigma}\mathbf{A}\lambda\delta\Sigma) \quad (5.16)$$

The third row of the Hessian system can now be evaluated and the result is Eq. (5.17):

$$\lambda^T\partial_{\Sigma}\mathbf{A}\delta\mathbf{\Psi} + \mathbf{\Psi}^T\partial_{\Sigma}\mathbf{A}\delta\lambda = -\lambda^T\partial_{\Sigma}\mathbf{A}\mathbf{\Psi} \quad (5.17)$$

Eqs. (5.13) and (5.16) can now be substituted into Eq. (5.17) and the result is Eq. (5.18):

$$\begin{aligned}
& \Psi^T \partial_{\Sigma} \mathbf{A} \mathbf{A}^{-T} (-\mathbf{M}(\Psi - \tilde{\Psi}) - \mathbf{A}^T \lambda - \mathbf{M} \mathbf{A}^{-1} (\mathbf{q} - \mathbf{A} \Psi - \partial_{\Sigma} \mathbf{A} \Psi \delta \Sigma) - \partial_{\Sigma} \mathbf{A} \lambda \delta \Sigma) + \\
& \lambda^T \partial_{\Sigma} \mathbf{A} \mathbf{A}^{-1} (\mathbf{q} - \mathbf{A} \Psi - \partial_{\Sigma} \mathbf{A} \Psi \delta \Sigma) = -\lambda^T \partial_{\Sigma} \mathbf{A} \Psi
\end{aligned} \tag{5.18}$$

This equation can now be solved for the $\delta \Sigma$. The terms that contain $\delta \Sigma$ are grouped together to form a square matrix that will be referred to as the \mathbf{S} matrix or Schur complement. The terms that do not contain a $\delta \Sigma$ are grouped together to form a vector that will be referred to as the \mathbf{U} vector. Therefore, the systems of linear equations is reformulated in the form of $\mathbf{S} \delta \Sigma = \mathbf{U}$. The terms that form the \mathbf{S} matrix are displayed in Eq. (5.19):

$$\mathbf{S} = \lambda^T \partial_{\Sigma} \mathbf{A} \mathbf{A}^{-1} \partial_{\Sigma} \mathbf{A} \Psi + \Psi^T \partial_{\Sigma} \mathbf{A} \mathbf{A}^{-T} (\mathbf{M} \mathbf{A}^{-1} \partial_{\Sigma} \mathbf{A} \Psi - \partial_{\Sigma} \mathbf{A} \lambda) \tag{5.19}$$

The terms that form the \mathbf{U} vector can be seen in Eq. (5.20):

$$\mathbf{U} = -\lambda^T \partial_{\Sigma} \mathbf{A} \mathbf{A}^{-1} \mathbf{q} + \Psi^T \partial_{\Sigma} \mathbf{A} (\lambda + \mathbf{A}^{-T} \mathbf{M} (\mathbf{A}^{-1} \mathbf{q} - \tilde{\Psi})) \tag{5.20}$$

Once $\delta \Sigma$ has been found, then the updates for the other parameters, $\delta \Psi$ and $\delta \lambda$, can be found by solving Eqs. (5.14) and (5.15) with these values of $\delta \Sigma$.

F. Newton's Method for Multiple Experiments

The inverse transport problem can be extended to multiple experiments rather easily. First, the Lagrangian functional for multiple experiments can be written as the summation of the Lagrangian functionals for each experiment. This relationship is given in Eq. (5.21):

$$\mathcal{L}_e(\Psi, \lambda, \Sigma) = \sum_i^N \frac{1}{2}(\Psi_i - \tilde{\Psi}_i)^T \mathbf{M}_i(\Psi_i - \tilde{\Psi}_i) + \lambda_i^T (\mathbf{A}\Psi_i - \mathbf{q}_i) \quad (5.21)$$

Here, i is the experiment index and it denotes that each experiment contains its respective set of computed angular fluxes, N is the total number of experiments, Ψ_i , measured angular fluxes, $\tilde{\Psi}_i$, importances, λ_i , sources, \mathbf{q}_i , and measurements locations on the boundary, \mathbf{M}_i . The transport operator, \mathbf{A} , remains unchanged with each new experiment because the geometry of the domain remains unchanged. The gradient of the Lagrangian for multiple experiments can then be given in Eq. (5.22):

$$\mathbf{F}_e(\Psi, \lambda, \Sigma) = \begin{pmatrix} \mathbf{M}_1(\Psi_1 - \tilde{\Psi}_1) + \mathbf{A}^T \lambda_1 \\ \vdots \\ \mathbf{M}_N(\Psi_N - \tilde{\Psi}_N) + \mathbf{A}^T \lambda_N \\ \mathbf{A}\Psi_1 - \mathbf{q}_1 \\ \vdots \\ \mathbf{A}\Psi_N - \mathbf{q}_N \\ \lambda_1^T \partial_{\Sigma} \mathbf{A}\Psi_1 \\ \vdots \\ \lambda_N^T \partial_{\Sigma} \mathbf{A}\Psi_N \end{pmatrix} = \begin{pmatrix} 0 \\ \vdots \\ 0 \\ 0 \\ \vdots \\ 0 \\ 0 \\ \vdots \\ 0 \end{pmatrix} \quad (5.22)$$

The Hessian matrix for multiple experiments is given by Eq. (5.23):

$$\mathbf{H}_e = \begin{pmatrix} \mathbf{M}_1 & 0 & 0 & \mathbf{A}^T & 0 & 0 & \partial_\Sigma \mathbf{A}^T \lambda_1 & 0 & 0 \\ 0 & \ddots & 0 & 0 & \ddots & 0 & 0 & \ddots & 0 \\ 0 & 0 & \mathbf{M}_N & 0 & 0 & \mathbf{A}^T & 0 & 0 & \partial_\Sigma \mathbf{A}^T \lambda_N \\ \mathbf{A} & 0 & 0 & \mathbf{0} & 0 & 0 & \partial_\Sigma \mathbf{A} \Psi_1 & 0 & 0 \\ 0 & \ddots & 0 & 0 & \ddots & 0 & 0 & \ddots & 0 \\ 0 & 0 & \mathbf{A} & 0 & 0 & \mathbf{0} & 0 & 0 & \partial_\Sigma \mathbf{A} \Psi_N \\ \lambda_1^T \partial_\Sigma \mathbf{A} & 0 & 0 & \Psi_1^T \partial_\Sigma \mathbf{A}^T & 0 & 0 & \mathbf{0} & 0 & 0 \\ 0 & \ddots & 0 & 0 & \ddots & 0 & 0 & \ddots & 0 \\ 0 & 0 & \lambda_N^T \partial_\Sigma \mathbf{A} & 0 & 0 & \Psi_N^T \partial_\Sigma \mathbf{A}^T & 0 & 0 & \mathbf{0} \end{pmatrix} \quad (5.23)$$

The Schur complement of the Hessian system with multiple experiments can also be determined. This Schur complement can be seen in Eq. 5.24:

$$\delta \Sigma = \left[\sum_{i=1}^N \mathbf{S}_i \right]^{-1} \left[\sum_{i=1}^N \mathbf{U}_i \right] \quad (5.24)$$

CHAPTER VI

RESULTS AND DISCUSSION

A. Pure Absorber Problems

In this section, the ability of Newton's method to identify the material properties of some simple pure absorber problems with only a single experiment will be explored. Example 1 presents the minimization problem that Newton's method is trying to solve. The effects of the number and position of the illuminating sources used to scan the domain is also examined in example 1. Example 2 serves as a comparison between Newton's method and the derivative-free Nelder-Mead method. The convergence process as Newton's method get closer to the actual solution is also present in example 2 for a problem with two inclusions. Example 3 displays the ability of Newton's method to reconstruct a more complex four-strip domain. Finally, Example 4 presents the effects of applying illuminating sources on different sides of a four-region domain.

1. Example 1 - Misfit Surfaces

The first example problem is a simple model with two homogeneous regions each encompassing half of the geometry and it can be seen in Figure VI-1. The two regions of the model are divided vertically down the center of the model. A complete description of the problem layout can be seen in Table VI-I. This two-parameter problem allows the objective function surface to be plotted as function of the two total cross sections of the two regions. The surface plots of the objective function will display the challenges associated with inverse transport because the finding the minimum of the objective function is not a trivial task.

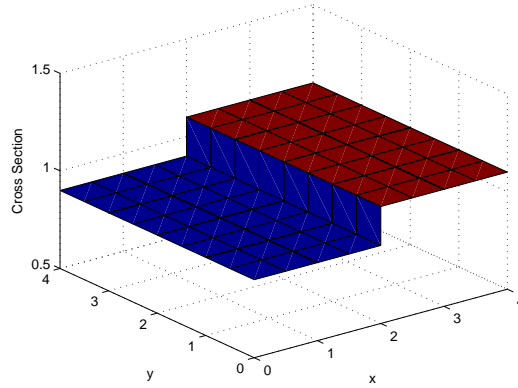


Fig. VI-1.: Two-Parameter Problem - True Cross Section Distribution.

Tables similar to Table VI-I will be used to describe the input parameters used to define the model geometry, reconstruction parameters and boundary sources used in each example. An angular quadrature of S_8 was maintained for all of the example problems in this thesis because it provided a reasonable compromise between sufficient angular resolution and reasonable computing times. Only square domains were examined in this thesis and the domain size is identified in either centimeters or number of mean free paths. The number of material regions specifies how many distinct materials regions exist in true geometry of the example problem. For this example, there are two distinct material regions in this problem. The material mesh specifies the number of possible distinct material regions. In example 1, a total of sixteen distinct materials could be modeled and independently reconstructed. However, the domain was assumed to consist of only two material regions so that the misfit surface could be plotted. The flux mesh specified the total number of cells used in the angular flux computation. This mesh is generally finer than the material mesh to increase model accuracy. The number of search parameters specifies the number of independent cross sections that are to be reconstructed in the optimization process.

The actual cross sections of the various material regions specify the values of the true solution which are used to obtain the reference solution and then discarded before the reconstruction begins. In this problem, the objective function surface was generated by evaluating the misfit function at 625 different parameter combinations. The parameter combinations were generated by varying the cross sections from 50 to 200% of their actual values in 25 equally-spaced increments. The surface source intensity was maintained at 100 for all examples explored in this thesis. In the reconstruction process, only the comparison between the boundary angular fluxes at each iteration and of the actual solution is significant and the exact magnitude of the illuminating source is irrelevant. The boundaries where each illuminating source was imposed is also presented in this Table. In future test problems, the initial guess for the cross section distribution within the domain is also presented in the Table. The initial guess is very crucial in the optimization process and the performance of the routine is highly dependent on the quality of the initial guess. Finally, the addition of multiple experiments on the reconstruction process is explored in future problems and the number of experiments is specified in these Tables.

Table VI-I.: Misfit Surface Parameter Description

Angular Quadrature (Sn)	8
Domain Size (cm)	4x4
Number of Material Regions	2
Material Mesh	4x4
Flux Mesh	8x8
Number of Searched Parameters	2
Actual Cross Section of Material 1 (cm^{-1})	0.9
Actual Cross Section of Material 2 (cm^{-1})	1.1
Number of Guessed Parameter Pairs	625
Range of Guesses for Cross Section of Material 1 (cm^{-1})	0.45-1.80
Range of Guesses for Cross Section of Material 2 (cm^{-1})	0.55-2.20
Illuminating Source Intensity ($\frac{n}{(cm^2-Sr)}$)	100
Boundaries of Imposed Illuminating Sources	left, right, both

As can be seen in Table VI-I, the misfit surface was plotted for three different illuminating sources. These illuminating sources only imposed a flux directed at the angle that was most normal to that boundary of the domain. The misfit values in the following surface plots were represent logarithmically to amplify the small changes in the value of the object function as the two parameters varied. However, since the logarithm of zero is infinite, nothing is plotted for the combination of the parameters that yields the true domain configuration. This accounts for the holes in the data plotted in the following misfit surface plots.

First, a beam that encompassed the entire left side of the model was used to

illuminate the domain. The objective function surface that resulted from this process can be seen in Fig. VI-2. Because the left boundary is formed completely by the first region and the illuminating source is only imposed on this boundary, the flux measured at the boundaries offers little recognition that the domain consists of two regions. This is the reason why the misfit surface appears as a shallow valley with a minimum that is rather difficult to locate. In fact, if one only imposed the source on the left side and only measured the emitted radiation on the right side, one might expect that the reconstructed domain would be homogeneous with a magnitude equivalent to the average of the cross sections of the two actual regions. The orientation of the misfit surface is also interesting to note. The valley of the misfit surface for the first case runs parallel to the value of the cross section of the second region. This means that the illuminating source provides more information about the first region than the second region. This makes sense because the illuminating source is imposed directly on the first region and the signal has already undergone much attenuation before it reaches the second region.

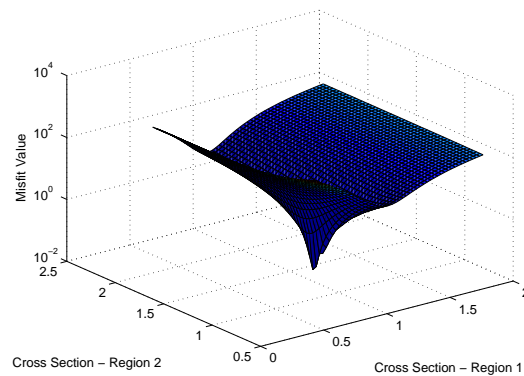


Fig. VI-2.: Two-Parameter Problem - Left Illumination Only.

In Fig. VI-3, again the objective function surface can be seen as a shallow valley. This is the result of the fact that the emitted flux on the left boundary offers

little information about the existence of the two distinct regions of the model. The orientation of the valley should also be noted. Since the boundary flux is imposed on the right side of the model, more information is now provided about the cross section of the second region than the first.

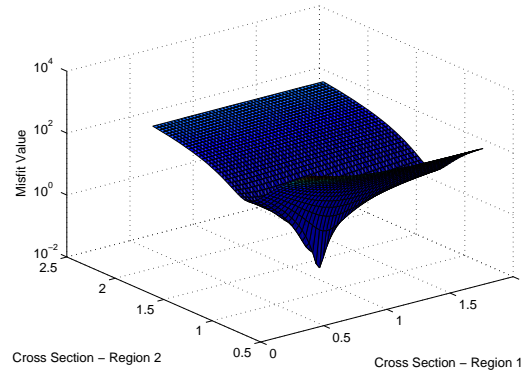


Fig. VI-3.: Two-Parameter Problem - Right Illumination Only.

Finally, illuminating sources were imposed on both the left and right boundaries of the model in Fig. VI-4. In this case, the sources illuminate both sides of the model and both cross sections become much more distinguishable. This is evidenced by the fact that the misfit surface plot is no longer a shallow valley, but more conical in shape. Finding the minimum of a cone is a much simpler optimization problem than finding the minimum of a shallow valley, because the objective function varies greatly along the conical surface and the gradient of a conical surface points more directly toward the minimum of the objective function. This also evidences a general trend that will be reinforced in the example problems to come that the addition of more illuminating beams, more measurement points and more experiments improves the ability of Newton's method to reconstruct the cross section values.

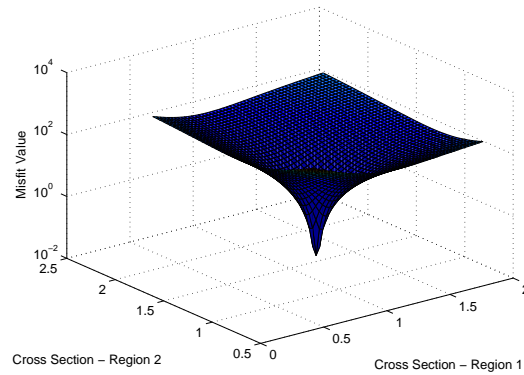


Fig. VI-4.: Two-Parameter Problem - Illumination from Both Left and Right Sides.

2. Example 2 - Homogeneous Domain and Dual Inclusion Convergence Study

The second example problem explores the ability of Newton's method to reconstruct the total cross sections of a homogeneous domain. All twenty-five of the cross sections of the domain are reconstructed independently and the Nelder-Mead method was also explored as a comparison between a method that computes the first and second derivatives of the Lagrangian versus one that simply evaluates the objective function. A list of the parameters that define the geometry, discretization scheme and source positions for the problem can be seen in Table VI-II.

Table VI-II.: Homogeneous Domain Parameter Description

Angular Quadrature (Sn)	8
Domain Size (cm)	6x6
Number of Material Regions	1
Material Mesh	5x5
Flux Mesh	15x15
Number of Searched Parameters	25
Actual Cross Section (cm^{-1})	1.00
Newton Initial Guess for Cross Section (cm^{-1})	1.75
Nelder-Mead Initial Guess for Cross Section (cm^{-1})	1.10
Illuminating Source Intensity ($\frac{n}{(cm^2-Sr)}$)	100
Illuminating Sources	all sides

The reconstruction and error results for the homogeneous domain can be seen in Fig. VI-5 for Newton's method and in Fig. VI-6 for the derivative-free method. It is noticeable that the error in the reconstruction for Newton's method is orders of magnitude less than the error found using the Nelder-Mead method. The Nelder-Mead method was also provided with a homogeneous initial guess for the total cross section within the domain of 1.1. This value was much closer to the actual cross section of the domain than the initial guess provided for Newton's method of 1.75. Based on these results, it seems that the Nelder-Mead algorithm is more susceptible to be stuck in local minima than Newton's method. Further comparison of the two methods has been included in Table VI-III.

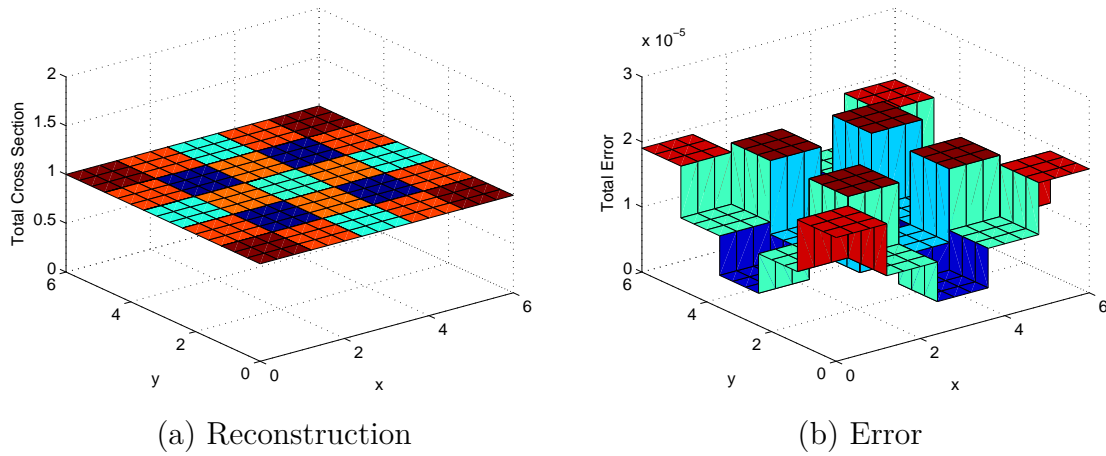


Fig. VI-5.: Homogeneous Domain: Reconstructed Cross Sections and Error Using Newton's Method.

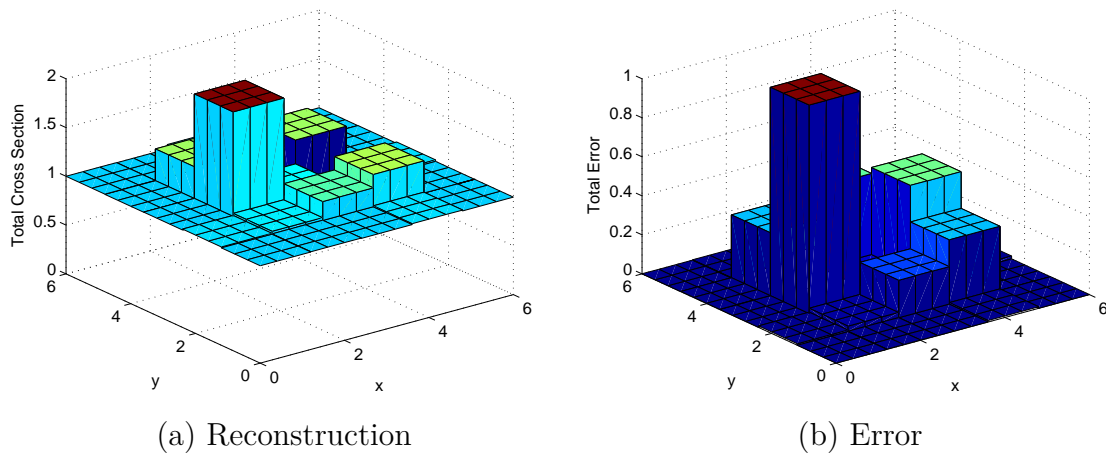


Fig. VI-6.: Homogeneous Domain: Reconstructed Cross Sections and Error Using Nelder-Mead Method.

In Table VI-III, we can see that Newton's method required much less computational time and fewer iterations than the Nelder-Mead algorithm. This is expected because Newton's method is a second order method that uses more information about

the objective function to locate its minimum. The final value of the Lagrangian was also determined to be orders of magnitude smaller for Newton's method as supposed to the derivative free method. This also is to be expected because the quality of the reconstruction was much better for Newton's method than that of the Nelder-Mead method.

Table VI-III.: Homogeneous Domain Convergence Comparison

Method	Newton	Nelder-Mead
Time (hrs)	0.06	8.47
Number of Iterations	56	72515
Magnitude of \mathcal{L}	10^{-6}	10^{-1}

Once the ability of Newton's method to reconstruct a homogeneous domain was established, a domain with two inclusions was reconstructed using Newton's method. Multiple figures have been included in this thesis to display the convergence process of Newton's method as it tries to find the parameters of the domain. A list of the parameters that define the geometry, discretization scheme and source positions for the problem can be seen in Table VI-IV. Again, all twenty-five parameters were reconstructed independently and further refinement was used in the computation of the flux solution to achieve a more accurate result.

Table VI-IV.: Dual Inclusion Domain Parameter Description

Angular Quadrature (Sn)	8
Domain Size (cm)	6x6
Number of Material Regions	3
Material Mesh	5x5
Flux Mesh	60x60
Number of Searched Parameters	25
Actual Cross Section of Surroundings (cm^{-1})	1.00
Actual Cross Section of Absorbers (cm^{-1})	1.50
Homogeneous Initial Guess for Cross Section (cm^{-1})	1.75
Illuminating Source Intensity ($\frac{n}{(cm^2-Sr)}$)	100
Illuminating Sources	all sides

Fig. VI-7 shows the convergence history for the dual inclusion problem. Each picture represents about every ninth iteration. It can be noticed that solution changes greatly in the first thirty iterations as Newton's method is searching for the parameters that best represent those of the domain. After iteration 30, the image changes very little and even large Newton steps lead to very small changes in the values of the parameters. Finally, the convergence criteria of reducing the Lagrangian and misfit functions to values less than 10^{-6} is achieved by iteration 92. This convergence criteria was used on all of the problems in this thesis unless specified otherwise.

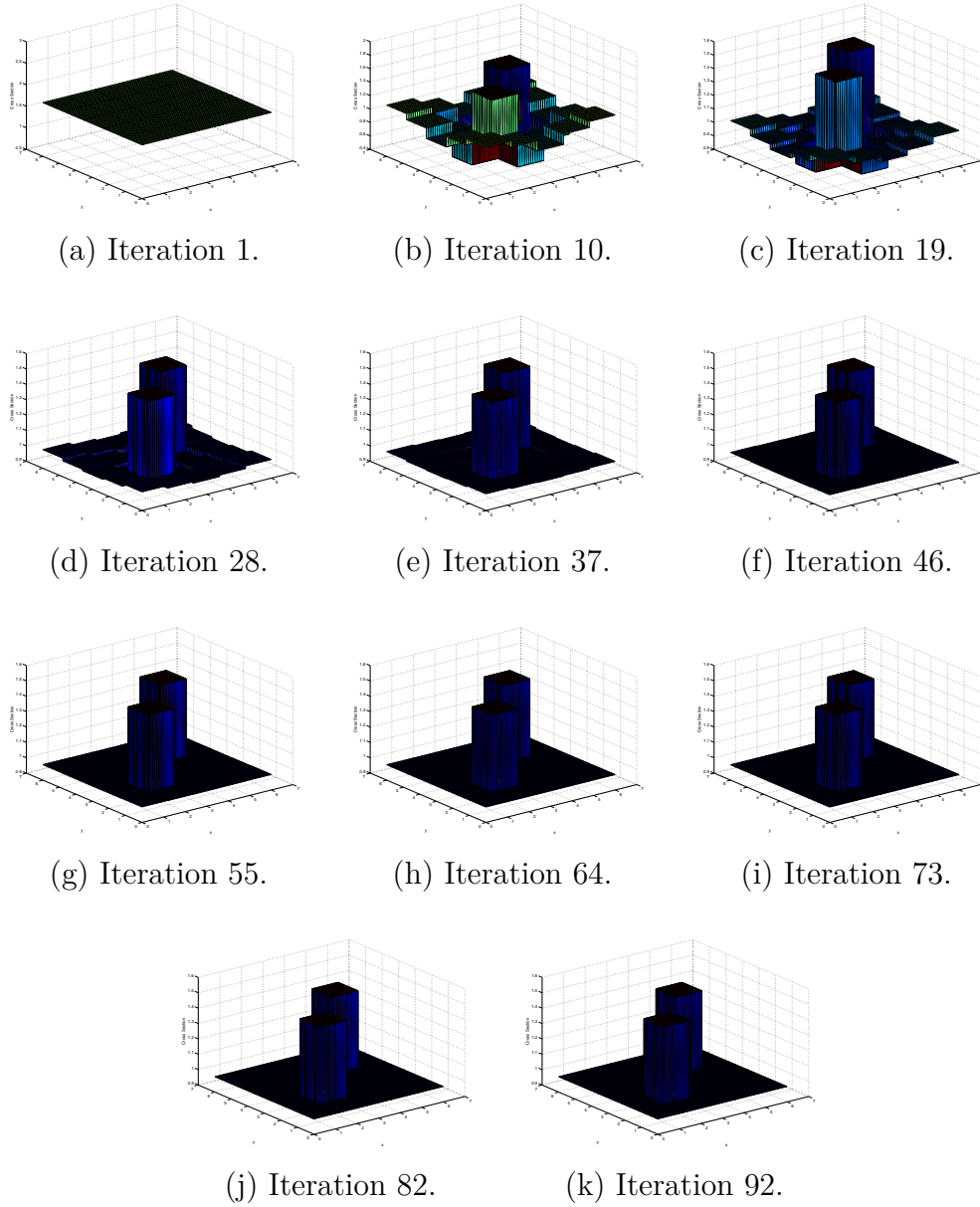


Fig. VI-7.: Dual Inclusion Domain Reconstruction.

3. Example 3 - Four-Strip Domain

The third example problem explores the ability of the optimization method to reconstruct a domain comprised of four different materials aligned in a series of strips

of equal width. Each of the four different regions possesses a different cross section value and the example tests the ability of Newton's method to reconstruct a more complex domain. The true cross section map of the four strip domain can be seen in Fig. VI-8. A detailed description of the parameters that definite the geometry, discretization scheme, source locations and reconstructed cross sections can be found in Table VI-V. Because of the increased complexity of this four domain model, further refinement was required in the flux solution to allow domain reconstruction. In this model, all 16 of the possible distinct materials were allowed to independent in the reconstruction process. Sources were imposed and measurements were recorded on all boundaries of this model.

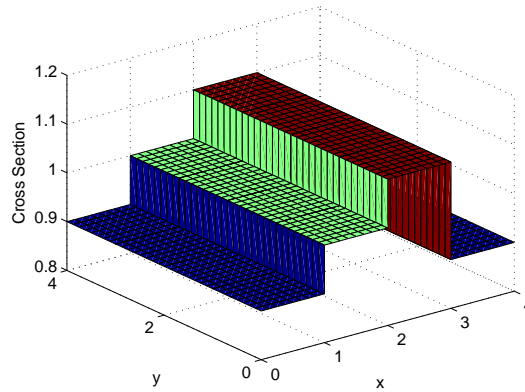


Fig. VI-8.: Actual Four-Strip Domain.

Table VI-V.: Parameter Description of Four-Strip Domain

Angular Quadrature (S_n)	8
Domain Size (cm)	4x4
Number of Material Regions	4
Material Mesh	4x4
Flux Mesh	32x32
Number of Searched Parameters	16
Actual Cross Section of Material 1 (cm^{-1})	0.9
Actual Cross Section of Material 2 (cm^{-1})	1.0
Actual Cross Section of Material 3 (cm^{-1})	1.1
Actual Cross Section of Material 4 (cm^{-1})	0.9
Homogeneous Initial Guess for Cross Section (cm^{-1})	1.0
Illuminating Source Intensity ($\frac{n}{(cm^2-Sr)}$)	100
Illuminating Sources	all sides

In Fig. VI-9, it can be noticed that the reconstruction was a success and the final error was on the order of 10^{-5} . In this process the misfit and Lagrangian values were minimized to less than 10^{-6} in fourteen iterations. This convergence tolerance was maintained for all of the results presented in this thesis. All fourteen iterations were conducted in about twenty minutes.

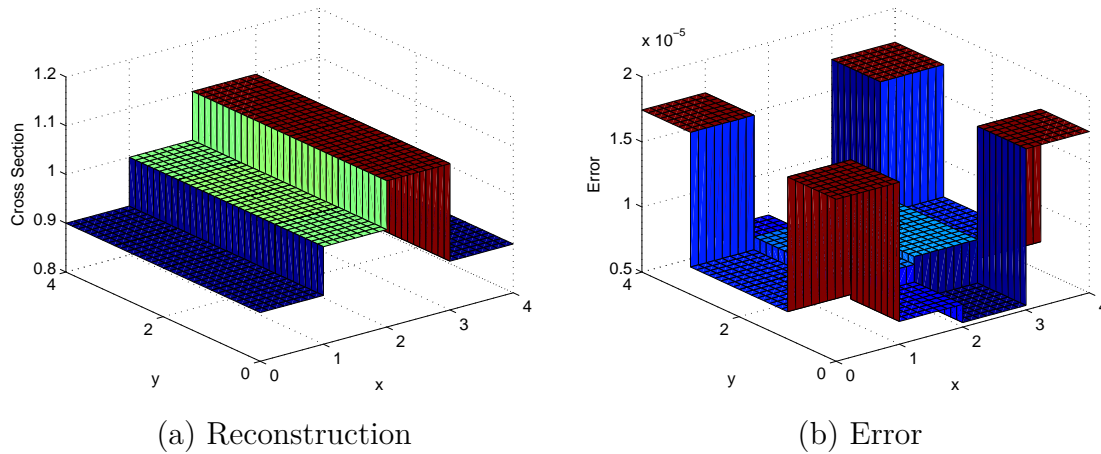


Fig. VI-9.: Four-Strip Domain Reconstructed Cross Sections and Error.

4. Example 4 - Four-Region Domain with Illuminating Sources on 1, 2, 3 or 4 Side(s)

In example 4, the ability of Newton's method to reconstruct the cross sections of a four-region domain is explored as illuminating beams are imposed on 1, 2, 3 or 4 sides of the geometry. Each reconstruction is conducted with only one experiment and it is shown that reconstruction ability improves as illuminating beams are imposed on more sides of the model. A list of the parameters that define the geometry, discretization scheme and source positions for the problem can be seen in Table VI-VI.

Table VI-VI.: Parameter Description of Four-Region Domain with Varying Illuminating Sources

Angular Quadrature (Sn)	8
Domain Size (cm)	8x8
Number of Material Regions	4
Material Mesh	4x4
Flux Mesh	16x16
Number of Searched Parameters	16
Actual Cross Section of Material 1 (cm^{-1})	0.7
Actual Cross Section of Material 2 (cm^{-1})	0.9
Actual Cross Section of Material 3 (cm^{-1})	1.1
Actual Cross Section of Material 4 (cm^{-1})	1.3
Homogeneous Initial Guess for Cross Section (cm^{-1})	1.5
Illuminating Source Intensity ($\frac{n}{(cm^2-Sr)}$)	100
Illuminating Sources	1, 2, 3, 4 sides

A diagram that displays the locations of each of the four material regions and labels each of the sides of the geometry can be seen in Fig. VI-10. This same material layout and side numbering scheme was maintained for all of the four region problems examined in this thesis. These four region problems can be found in examples 8, 16 and 17.

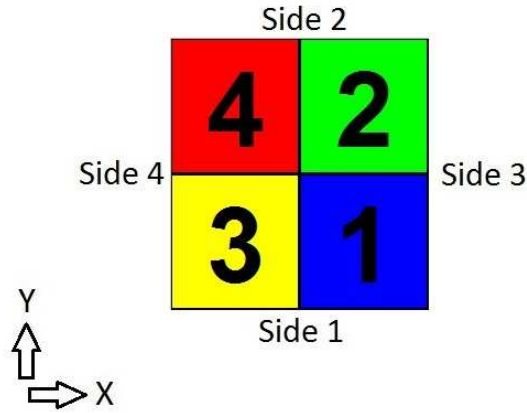


Fig. VI-10.: Diagram of Four-Region Domain with Sides and Material Regions Identified.

In Fig. VI-11, the results of the test case where beams were only imposed on the side 1 of the geometry as seen in Fig. VI-10. In this case, Newton's method fails to generate a reconstruction of the domain because insufficient radiation is transmitted through the regions defined by materials 2 and 4 when the beam is only imposed on side 1. Because only minimal radiation is transmitted through regions 2 and 4, Newton's method has little information about these regions and begins to propose outrageous values for the cross sections of these regions. Because Newton's method was diverging from the solution and reconstruction was unlikely, the process was terminated after 100 iterations and these results are presented in Fig. VI-11. Similar results are expected if the sources were applied solely to any other side of the geometry simply because insufficient information is collected from a single scan conducted on a single side of the domain.

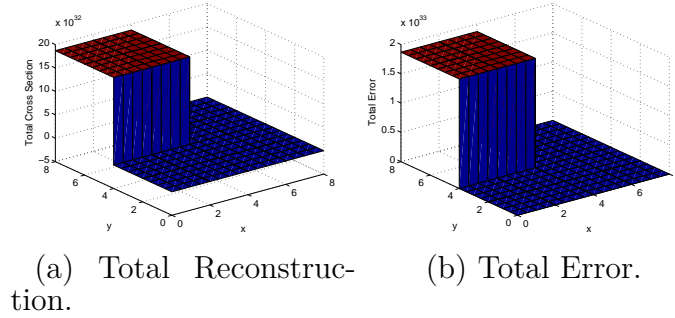


Fig. VI-11.: Domain with Source on 1 Side Reconstructing the Total Cross Sections.

In Figs. VI-12, VI-13 and VI-14, sufficient information was collected from imposing beams on multiple sides of the model to permit reconstruction. The trend of reduced reconstruction error as illuminating sources were imposed on more sides of the model can also be noticed. In Fig. VI-12, beams were imposed on the sides 1 and 2 of the geometry as explained in Fig. VI-10. In Fig. VI-13, beams were imposed on sides 1, 2 and 3 as seen in Fig. VI-10. Finally, illuminating sources were modeled on all sides of the model in Fig. VI-14.

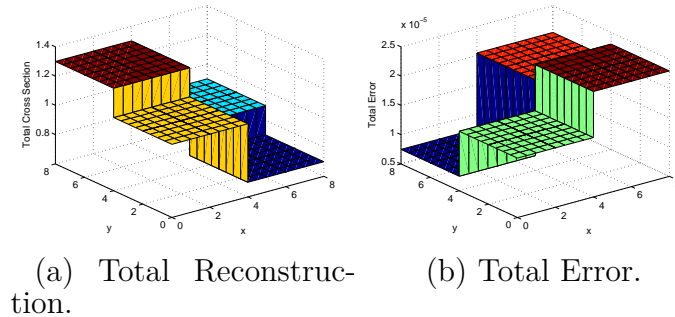


Fig. VI-12.: Domain with Sources on 2 Sides Reconstructing the Total Cross Sections.

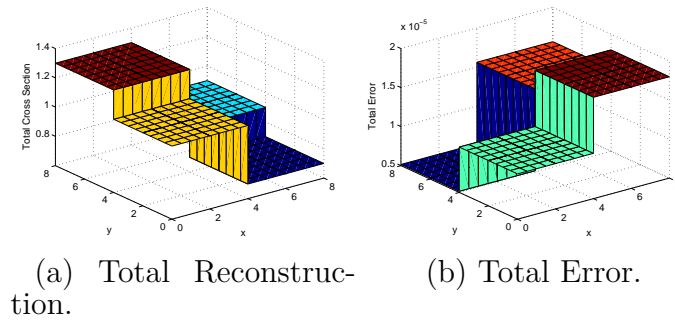


Fig. VI-13.: Domain with Sources 3 Sides Reconstructing the Total Cross Sections.

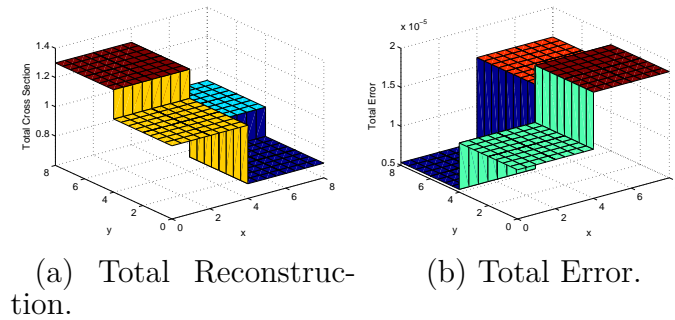


Fig. VI-14.: Domain with Sources on 4 Sides Reconstructing the Total Cross Sections.

5. Summary of Findings from Pure Absorber Problems

In the pure absorber problems section, some initial simple problems were explored to visually get a feel for the inverse transport problem and how Newton's method uses variation of parameters to locate the solution of this inverse transport problem. In example 1, the surface of objective function for a simple two-parameter problem was plotted to understand what the surface looks like and the challenges associated with locating the minimum of this surface. In this problem, the reduction in the complexity of the optimization problem by applying illuminating sources to two opposite sides of the model rather than just to one side was also noticed. This simplification in

the optimization process was noticed as the misfit surface changed shape from a shallow valley with a minimum that was rather difficult to locate to more of a conical surface with an apparent minimum. In example 2, the ability of Newton's method to reconstruct a homogeneous domain was explored. The Nelder-Mead method was also used to reconstruct the same homogeneous domain to show the benefits of Newton's method. Newton's method required fewer iterations, less computational time and reconstructed an image with less error than the Nelder-Mead algorithm. This was attributed to Newton's method's utilization of the gradient and Hessian information of the constrained optimization problem. A problem with two inclusions was also studied to display the reconstruction process using Newton's method. It was noticed that in the early iterations as Newton's method is searching for the parameters of the domain, the image varies greatly. As Newton's method begins to propose values of the parameters that are close to those used to create the synthetic data, the image changes very little even as Newton takes large steps. In example 3, a domain comprised of four strips was considered to display Newton's ability to reconstruct the material properties of a more complex domain. Finally in example 4, a four region domain each with unique cross sections was considered while imposing beams on 1, 2, 3 or all sides of the model in a single experiment. This study displayed the general trend that as illuminating sources are applied to more sides of the model, the error in the resulting image is reduced. It was also noticed that if insufficient radiation is transmitted through a domain, Newton's method can not determine the cross sections of certain regions of the model and values for those cross sections that deviate greatly from the true values of those regions are proposed.

B. Pure Absorbers with Multiple Experiments

In this section, the ability of Newton's method to reconstruct the cross sections of various pure absorber domains where multiple experiments or scans are used. Examples 5 and 6 explore the optical thickness limits where the measurable signal becomes too small to permit reconstruction. Eight experiments each covering one half of a side are used in example 5, where as sixteen experiments each covering one fourth of a side are used in example 6. Example 7 examines the sensitivity of Newton's method to the proposed initial guess for the cross sections of a homogeneous domain reconstructed as four independent regions. Finally, example 8 displays the effects of using measurements collected from different sides of the domain. This example is successful in reconstructing all of the cross sections for all of the cases, but the same example will be revisited in example 17 in the scattering section and this will not be the case.

1. Example 5 - Central Inclusion Domains with 8 Experiments

In example 5, domains with a central inclusion and surrounding medium of increasing size are studied. These problems explored the optical thickness limit of Newton's method as more material is padded around the central inclusion. This additional material increases the number of mean free paths that the incident radiation must travel through until it reaches the boundary. This results in a reduction in the measurable signal at the boundary and increases the difficulty of the reconstruction process. In each of the models in this example, the flux cell size was held constant at 0.5 by 0.5 centimeters and eight experiments with beams covering half of a side were used in the reconstruction process. The domains were assumed to be comprised of only two parameters representing the surroundings and central inclusion and only the two

cross sections were reconstructed. The condition number of the Schur matrix was tracked throughout the reconstruction to determine how ill-conditioned the problem was and the reliability of the results. A list of the parameters that define the geometry, discretization scheme, reconstructed cross sections and source positions for the problem can be seen in Table VI-VII.

Table VI-VII.: Parameter Description of Central Inclusion Domains with 8 Experiments

Angular Quadrature (S_n)	8
Domain Sizes (cm)	8x8, 12x12, 16x16, 20x20
Number of Material Regions	2
Material Mesh	4x4, 6x6, 8x8, 10x10
Flux Mesh	16x16, 24x24, 32x32, 40x40
Number of Searched Parameters	2
Actual Cross Section of Surroundings (cm^{-1})	0.9
Actual Cross Section of Absorber (cm^{-1})	1.3
Homogeneous Initial Guess for Cross Section (cm^{-1})	1.5
Illuminating Source Intensity ($\frac{n}{(cm^2-Sr)}$)	100
Illuminating Sources	8-exp, 1/2-side each

Figs. VI-15, VI-16, VI-17 and VI-18 present the reconstruction, error and condition number results for the 8x8, 12x12, 16x16 and 20x20 centimeter central inclusion problems, respectively. It can be noticed that the error in the reconstruction and the condition number of the Schur matrix is increased as the optical thickness of

the problem is increased. The reconstruction is successful for the 8x8, 12x12 and 16x16 centimeter cases, but it fails for the 20x20 centimeter case. In all of the successful cases, there is a spike in the condition number in the early iterations before the method stabilizes. The maximum order of magnitude of the condition numbers registered for the 8x8, 12x12 and 16x16 centimeter cases were 10^6 , 10^{11} and 10^{15} , respectively. In the 20x20 centimeter case, the condition number of the Schur matrix grows exponentially to 10^{27} in later iterations resulting in a failed reconstruction. In this case, again insufficient radiation reaches the center of the model where the inclusion is and therefore, the value of the cross section of this region has a negligible effect on the computed fluxes. Because of this Newton's method can not detect the inclusion and begins to propose huge values for the cross section of this region. In this case, the termination criteria of minimizing the misfit and Lagrangian below 10^{-6} were still satisfied after 134 iterations because the inclusion cross section value has no effect on the flux solution. The final reconstructed cross section of the surroundings is correct, but the cross section of the inclusion varies by orders of magnitude from the actual solution as seen in Fig. VI-18.

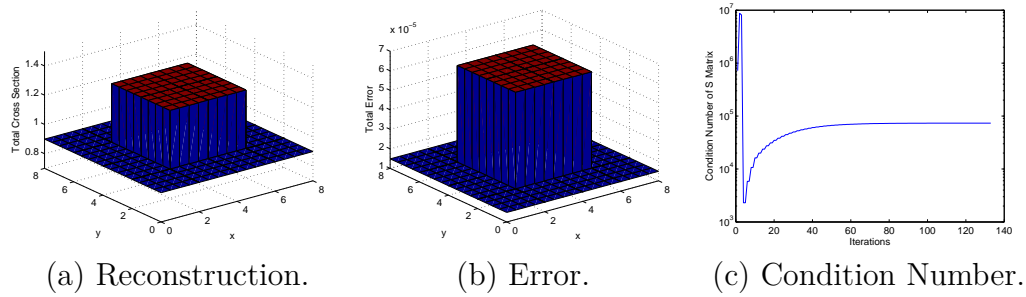


Fig. VI-15.: Reconstruction, Error and Condition Number Results for the 8x8cm Central Inclusion Problem with 8 Experiments.

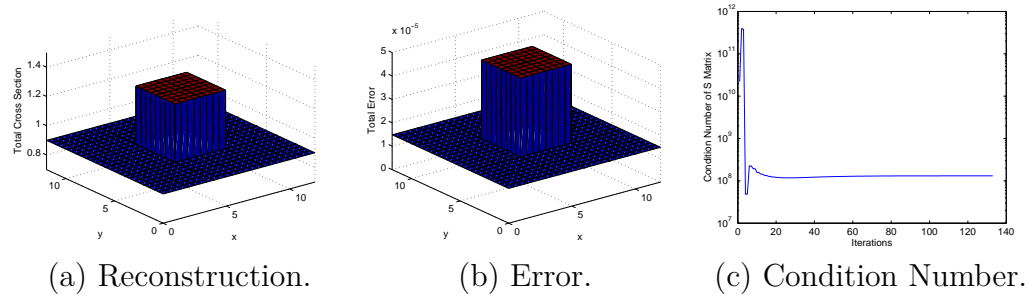


Fig. VI-16.: Reconstruction, Error and Condition Number Results for the 12x12cm Central Inclusion Problem with 8 Experiments.

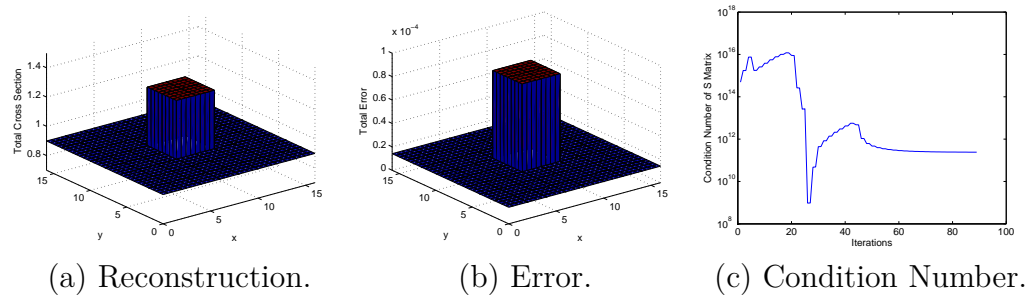


Fig. VI-17.: Reconstruction, Error and Condition Number Results for the 16x16cm Central Inclusion Problem with 8 Experiments.

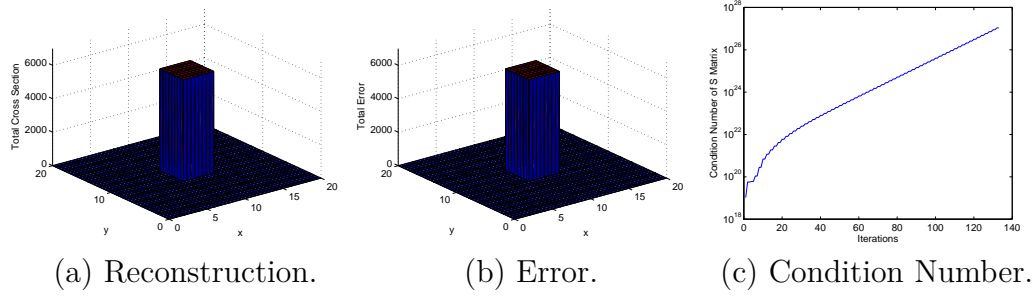


Fig. VI-18.: Reconstruction, Error and Condition Number Results for the 20x20cm Central Inclusion Problem with 8 Experiments.

2. Example 6 - Central Inclusion Domains with 16 Experiments

Example 6 is very similar to example 5 where central inclusion of increasing optical thickness is studied. In example 6, sixteen experiments each encompassing one fourth of a side are modeled as supposed to the eight experiment problems studied in example 5. Because of the additional experiments, 8x8, 12x12, 16x16 and 20x20 centimeter domains were able to be reconstructed and the method did not fail until the 24x24 centimeter domain was attempted. Again the domains were assumed to be comprised of only two materials and only two parameters were reconstructed. The same flux cell size was maintained as in example 5. A list of the parameters that define the geometry, discretization scheme, reconstructed cross sections and source positions for the problem can be seen in Table VI-VIII.

Table VI-VIII.: Parameter Description of Central Inclusion Domains with 16 Experiments

Angular Quadrature (S_n)	8
Domain Sizes (cm)	8x8, 12x12, 16x16, 20x20, 24x24
Number of Material Regions	2
Material Mesh	4x4, 6x6, 8x8, 10x10, 12x12
Flux Mesh	16x16, 24x24, 32x32, 40x40, 48x48
Number of Searched Parameters	2
Actual Cross Section of Surroundings (cm^{-1})	0.9
Actual Cross Section of Absorber (cm^{-1})	1.3
Homogeneous Initial Guess for Cross Section (cm^{-1})	1.5
Illuminating Source Intensity ($\frac{n}{(cm^2-Sr)}$)	100
Illuminating Sources	16-exp, 1/4-side each

Figs. VI-19, VI-20, VI-21, VI-22 and VI-23 present the reconstruction, error and condition number results for the 8x8, 12x12, 16x16, 20x20 and 24x24 centimeter central inclusion problems, respectively. As display in example 5, the error in the reconstruction and the condition number of the Schur matrix increase as the optical thickness of the problem increases. The reconstruction is successful for the 8x8, 12x12, 16x16 and 20x20 centimeter cases, but it fails for the 24x24 centimeter case. In all of the successful cases, there is a spike in the condition number in the early iterations before the method stabilizes. The maximum order of magnitude of the

condition numbers registered for the 8x8, 12x12, 16x16 and 20x20 centimeter cases were 10^6 , 10^{11} , 10^{16} and 10^{31} respectively. In the 24x24 centimeter case, the condition number of the Schur matrix grows exponentially to 10^{31} in later iterations resulting in a failed reconstruction. Just as in example 5, the termination criteria of minimizing the misfit and Lagrangian below 10^{-6} were still satisfied after 134 iterations because the inclusion cross section value has no effect on the flux solution. The method was again able to correctly reconstruct the cross section of the surrounding material, but the cross section of the inclusion region is off by orders of magnitude as seen in Fig. VI-23.

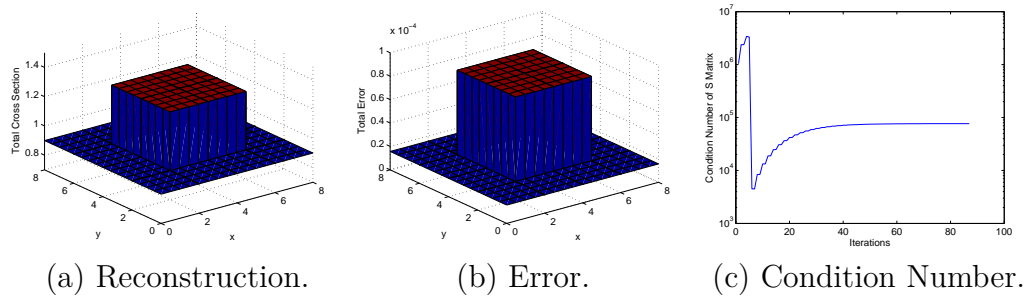


Fig. VI-19.: Reconstruction, Error and Condition Number Results for the 8x8cm Central Inclusion Problem with 16 Experiments.

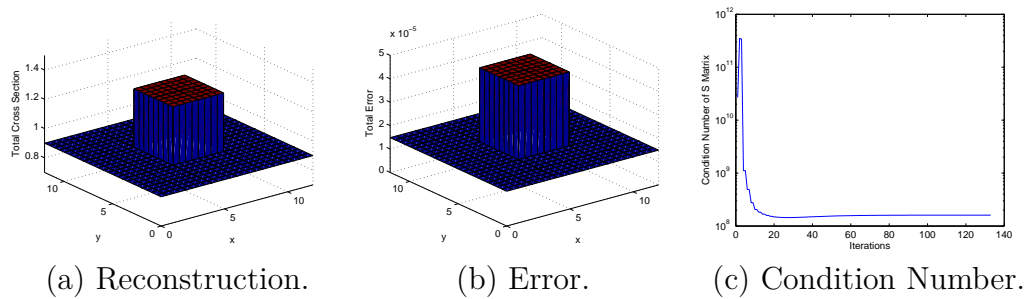


Fig. VI-20.: Reconstruction, Error and Condition Number Results for the 12x12cm Central Inclusion Problem with 16 Experiments.

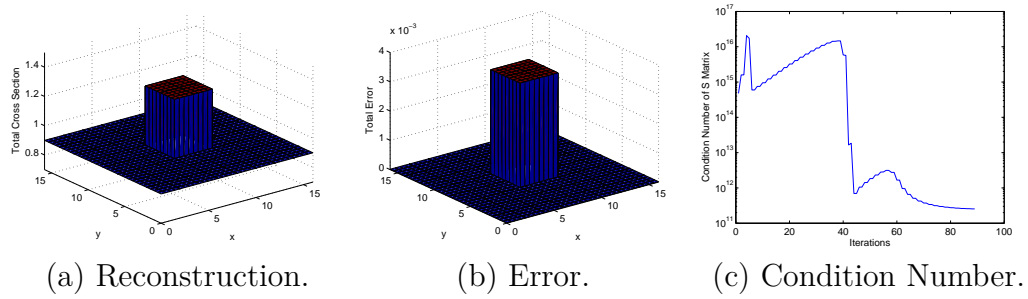


Fig. VI-21.: Reconstruction, Error and Condition Number Results for the 16x16cm Central Inclusion Problem with 16 Experiments.

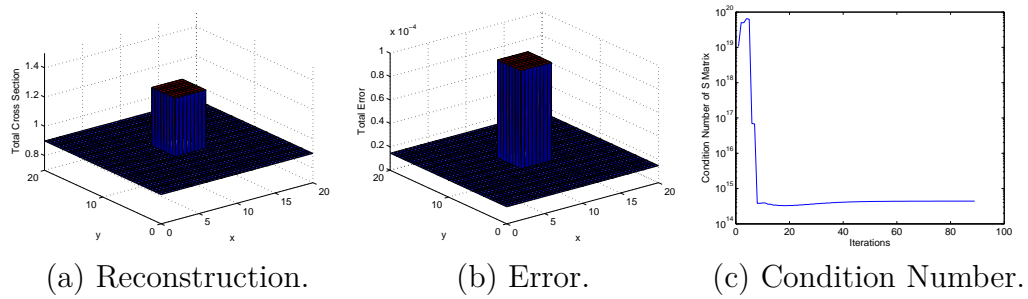


Fig. VI-22.: Reconstruction, Error and Condition Number Results for the 20x20cm Central Inclusion Problem with 16 Experiments.

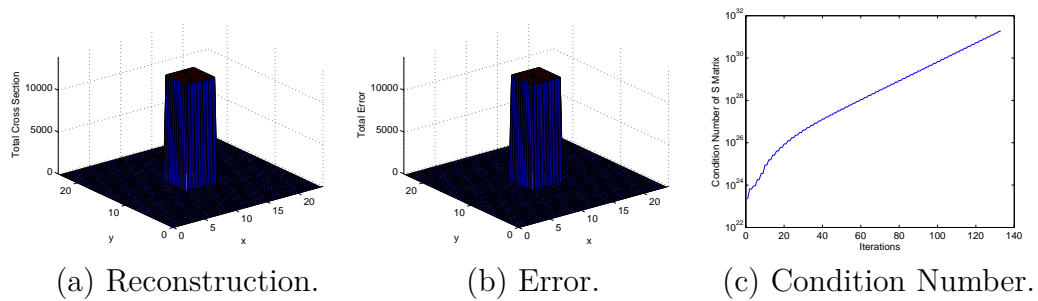


Fig. VI-23.: Reconstruction, Error and Condition Number Results for the 24x24cm Central Inclusion Problem with 16 Experiments.

Because of the only minimal improvement in the reconstruction ability when sixteen versus eight experiments were conducted and the increased computational time required for the additional experiments, the remaining problems in this thesis will be simulated with eight experiments unless otherwise specified. But, generally increasing the number of experiments leads to some improvements which include more accurate reconstructions with less error, reconstructions that converge in fewer iterations and reduction in the condition numbers seen in the Schur matrix. The one downfall is that increasing the number of experiments leads to more computational time spent in each Newton iteration. There definitely exists a threshold where the addition of more experiments leads to minimal improvement in image quality because imposing sources extremely close together and taking additional measurements extremely close together adds little new information to the reconstruction.

3. Example 7 - Homogeneous Domain Initial Guess Study

In example 7, the effect of varying the initial guess for the parameters was studied for a homogeneous domain. The proposed initial guesses were varied at different distances from the actual solution in the positive and negative directions. The method proved rather robust for reconstructing the parameters of this problem for all of the initial guesses attempted. Since the domain considered in this problem was homogeneous, a heterogeneous initial guess generated using random numbers was used to make the reconstruction more challenging. In each case, the initial guess for the parameters was shifted based on some percentage of the actual parameter distribution and then random numbers were then used to create heterogeneity in the initial guess at 20-25% of the shift percentage. A description of these initial guesses and the input parameters for the problem can be found in Table VI-IX.

Table VI-IX.: Parameter Description of Homogeneous Domain Reconstruction from Various Initial Guesses

Angular Quadrature (Sn)	8
Domain Sizes (cm)	4x4
Number of Material Regions	1
Material Mesh	4x4
Flux Mesh	16x16
Number of Searched Parameters	4
Actual Cross Section of Domain (cm^{-1})	1.0
Initial Guesses Approaching from Above (%)	1000 ± 200 , 5000 ± 1000 , 10000 ± 2500
Initial Guesses Approaching from Below (%)	75 ± 5 , 50 ± 10 , 25 ± 15
Illuminating Source Intensity ($\frac{n}{(cm^2-Sr)}$)	100
Illuminating Sources	8-exp, 1/2-side each

The sufficient decrease and curvature conditions were employed in all of the initial guess reconstructions conducted in this example. It was noticed that on many of the problems where the initial guess was below the actual solution, the Wolfe conditions would never be satisfied and the minimum step length was always used. To combat this problem, a slightly heuristic approach was employed where a check was conducted on the magnitude of the step length. If the step length was determined to be the same values for the five preceding iterations, the step length was then reset to 0.25 and the Newton iteration was continued. This approach proved successful for all of the cases tested in this example. The results of the three initial guess studies where the solution was approach from below can be seen in Figs. VI-24, VI-25 and VI-26.

All of these figures display the proposed initial guess, the final reconstruction and the error in the final reconstruction. All of these reconstructions were successful and the errors are all of similar magnitudes. The total number of iterations required to reduce the misfit and Lagrangian to less than 10^{-6} was determined to be 163, 81 and 62 for initial guesses of 75%, 50% and 25% of the actual parameters, respectively. Each of these reconstructions required the value of the step length to be reset to 0.25 multiple times.

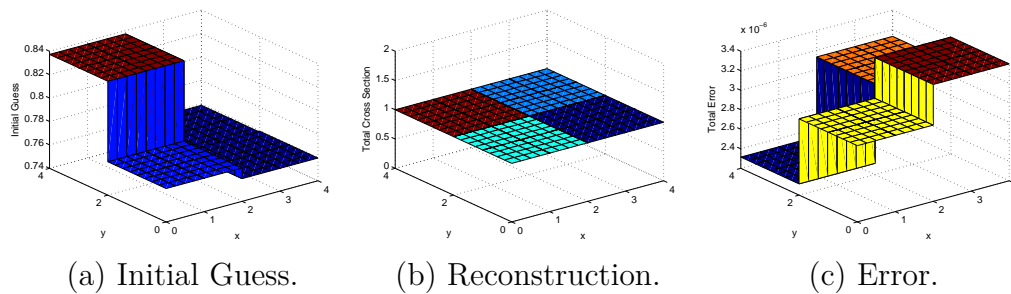


Fig. VI-24.: Initial Guess of $75\% \pm 5\%$ of Actual Cross Section of Homogeneous Domain.

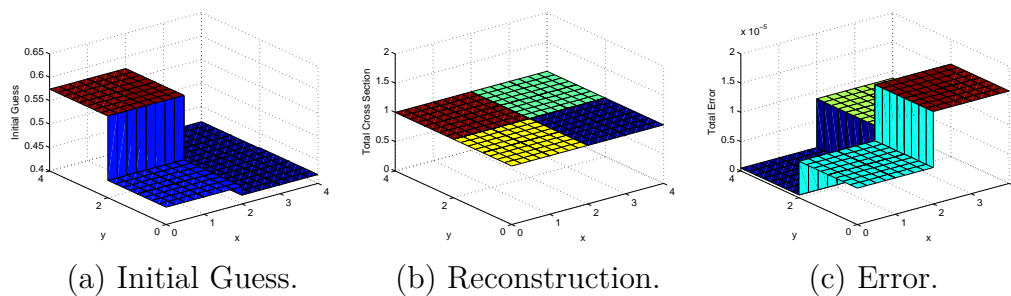


Fig. VI-25.: Initial Guess of $50\% \pm 10\%$ of Actual Cross Section of Homogeneous Domain.

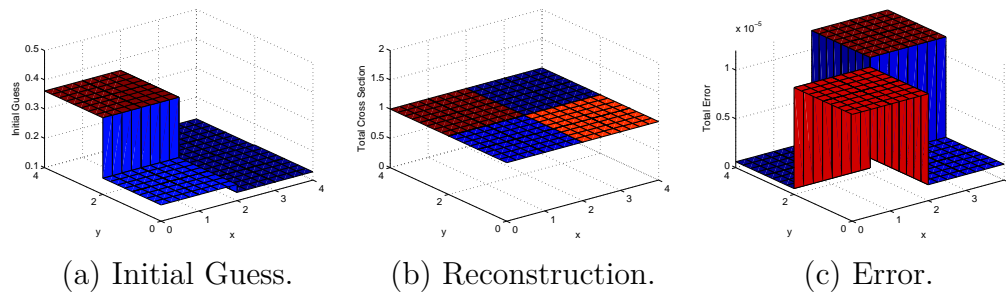


Fig. VI-26.: Initial Guess of $25\% \pm 15\%$ of Actual Cross Section of Homogeneous Domain.

In the case of the initial guess that approach the solution from above, the optimization method never stagnated with the minimum step length. These reconstructions took many fewer iterations than when the solution was approached from below. The results of the three initial guess studies where the solution was approached from above can be seen in Figs. VI-27, VI-28 and VI-29. All of these figures display the proposed initial guess, the final reconstruction and the error in the final reconstruction. All of these reconstructions were successful and the errors are all of similar magnitudes. The total number of iterations required to reduce the misfit and Lagrangian to less than 10^{-6} was determined to be 14, 25 and 18 for initial guesses of 1000%, 5000% and 10000% of the actual parameters, respectively.

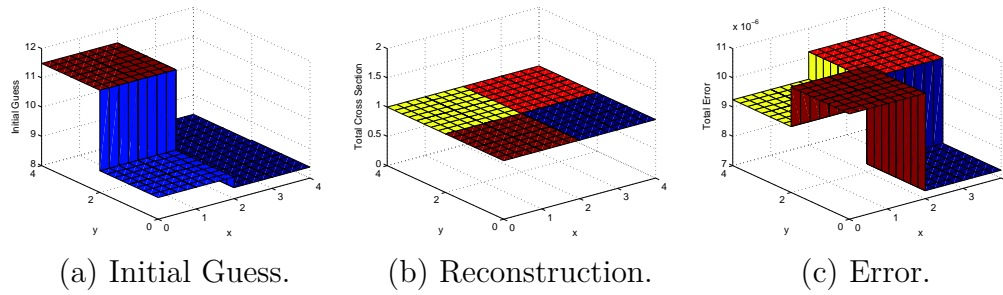


Fig. VI-27.: Initial Guess of $1000\% \pm 200\%$ of Actual Cross Section of Homogeneous Domain.

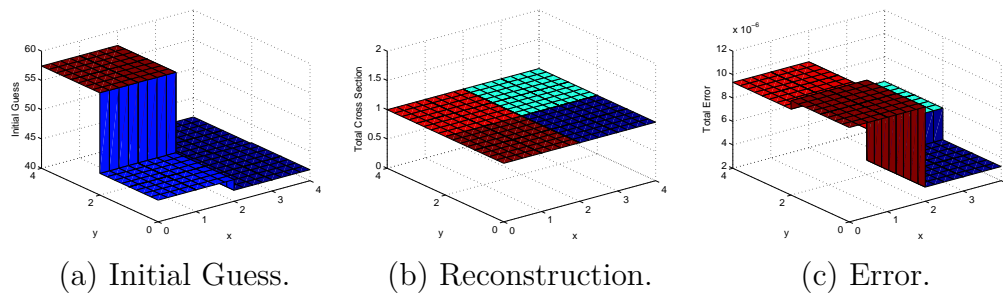


Fig. VI-28.: Initial Guess of $5000\% \pm 1000\%$ of Actual Cross Section of Homogeneous Domain.

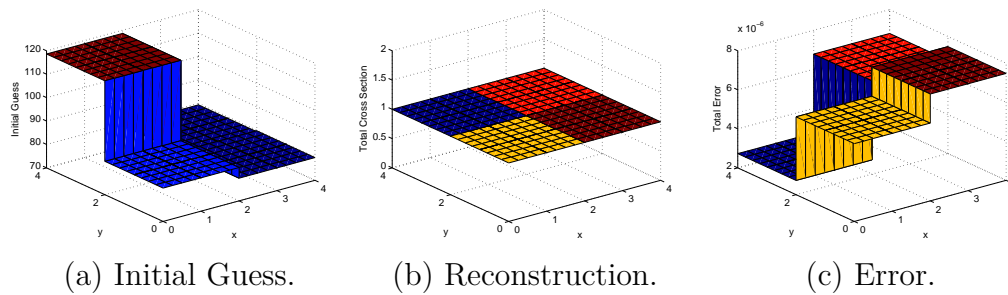


Fig. VI-29.: Initial Guess of $10000\% \pm 2500\%$ of Actual Cross Section of Homogeneous Domain.

Generally, Newton's method with the Wolfe conditions line search was able to reconstruct the solution easier from an initial guess that was above the values of the actual parameters. These higher initial guesses converged in many fewer iterations to solutions with lower error and the step size was never artificially modified.

4. Example 8 - Four-Region Domain with Measurements taken on 1, 2, 3 and 4 Sides

In example 8, a four-region domain is reconstructed with information collected from measurements on 1, 2, 3 or 4 sides of the model. All of these reconstructions were conducted with 8 experiments and a homogeneous initial guess for the parameters of 1.5 was used as the starting point for the reconstruction. The same material region layout and side numbering scheme was used in this example as can be seen in Fig. VI-10 of example 4. The example where measurements are only recorded from one side of the geometry collect measurements from side 1 as explained in Fig. VI-10. The test case where measurements are collected from two sides uses sides 1 and 2 as seen in Fig. VI-10. The test case where measurements are collected from three sides of the geometry uses sides 1, 2 and 3 as seen in Fig. VI-10. Finally, the last model uses measurements from all sides of the geometry to generate the image. A list of the parameters that define the geometry, discretization scheme, reconstructed cross sections and the source and measurement locations for the problem can be seen in Table VI-X.

Table VI-X.: Parameter Description of Four-Region Domain Measuring on 1, 2, 3 or 4 Side(s) of Model

Angular Quadrature (Sn)	8
Domain Sizes (cm)	8x8
Number of Material Regions	4
Material Mesh	4x4
Flux Mesh	16x16
Number of Searched Parameters	4
Actual Cross Section of Material 1 (cm^{-1})	0.7
Actual Cross Section of Material 2 (cm^{-1})	0.9
Actual Cross Section of Material 3 (cm^{-1})	1.1
Actual Cross Section of Material 4 (cm^{-1})	1.3
Homogeneous Initial Guesses (%)	1.5
Illuminating Source Intensity ($\frac{n}{(cm^2-Sr)}$)	100
Illuminating Sources	8-exp, 1/2-side each
Measurements	1, 2, 3 or 4 Sides

Figs. VI-30, VI-31, VI-32 and VI-33 show the reconstruction and error results for the four region domain reconstructions with measurements taken on 1, 2, 3 and 4 sides of the model, respectively. In every case investigated in this example, Newton's method was able to correctly identify the parameters of the domain. It can also be noticed that the quality of the reconstruction is improved and the error in the reconstruction is reduced as measurements from more sides of the model are used. The reconstructions were conducted in fifty-five, fifty-nine, fifty-nine and forty-five minutes

for the models with measurements on 1, 2, 3 and 4 sides, respectively. The images were generated in 126, 124, 132 and 130 iterations for the models with measurements on 1, 2, 3 and 4 sides, respectively. The total number of iterations is pretty consistent for all of the cases, but the reconstruction using measurements from all four sides finished ten minutes quicker than other cases.

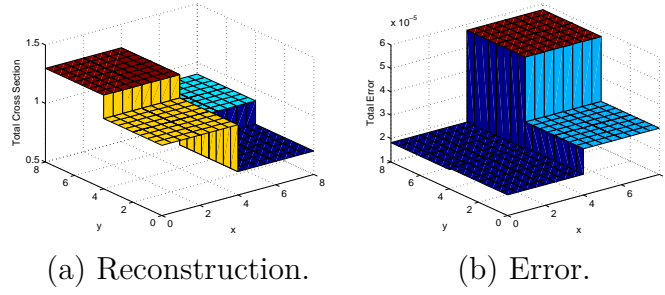


Fig. VI-30.: Four-Region Domain Measuring on 1 Side.

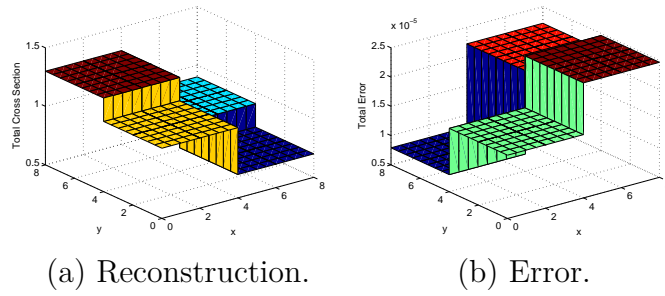


Fig. VI-31.: Four-Region Domain Measuring on 2 Sides.

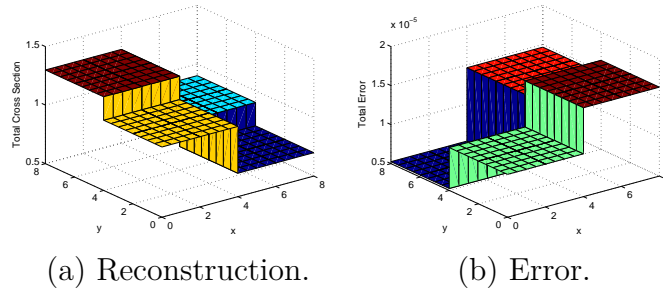


Fig. VI-32.: Four-Region Domain Measuring on 3 Sides.

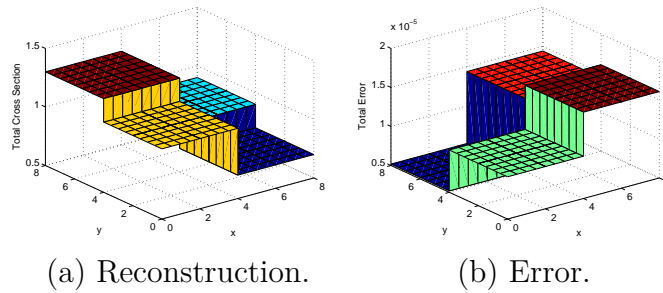


Fig. VI-33.: Four-Region Domain Measuring on 4 Sides.

5. Summary of Findings from Pure Absorbers with Multiple Experiments

In this section on pure absorbers with multiple experiments, the improvements in image quality when using multiple experiments was explored. In example 5, the optical thickness limit of the Newton's method was explored through central inclusion problems of increasing size. Eight experiments each with a beam covering half of a side were used to reconstruct these problems. The optical thickness limit was determined to be eight mean free paths deep into the object. The condition number of the Schur complement matrix was also tracked in these reconstructions and it was a good indicator of the difficulty of the reconstruction problem. The condition number of the Schur matrix increased as the optical thickness increased and all of the successful cases

showed sharp peaks in the condition number in earlier iterations, but lower condition numbers as the method proposes values of the cross sections that become increasingly close to the true cross section values. In the unsuccessful reconstruction, the condition number of the Schur matrix continued to increase through all the interactions of the optimization process and never stabilized. Example 6 showed many of the same trends as example 5. An optical thickness limit of nearly ten mean free paths was achieved with sixteen experiments rather than only eight. The same trends were observed with regard to the condition number of the Schur complement matrix as were seen in example 5. In example 7, the sensitivity of Newton’s method to the initial parameter distribution used to start the optimization process was studied. It was noticed that Newton’s method could reconstruct images much easier from an initial guess consisting of values that were larger in magnitude than the actual parameters than from one with values lower in magnitude. This was noticed from the need to force Newton’s method to take larger steps at various times in the optimization process to overcome stagnation points when starting from lower initial guesses. Also, many more iterations were required for lower initial guesses than higher ones. Finally in example 8, it was noticed that using measurements from more sides of the model in the reconstruction process generally leads to higher quality reconstruction with less error.

C. Pure Absorbers with Signal Noise and Bias

The next few test cases will simulate the effects of signal noise and bias on the measured angular fluxes that are used in the reconstruction process. The addition of signal noise simulates how the presence of background radiation will affect your detector readings. The addition of signal bias simulates the signal drift in the detector as the crystal temperature is increased from cold startup to operating temperatures.

Multiplicative signal noise assumes that all measurements experience the same level of noise represented by Eq. (6.1):

$$z_{i,\text{noise}} = z_i(1 + \beta\epsilon_i) \quad (6.1)$$

Here, β is the percentage of the actual signal that is noise, ϵ_i is the random number that ranges from positive to negative unity and z_i is the measured angular flux vector without signal noise. Signal bias can be represented by the relationship seen in Eq. (6.2):

$$z_{i,\text{biased noise}} = z_i(1 + \delta + \beta\epsilon_i) \quad (6.2)$$

Here, the additional δ term is the signal bias and this term simply shifts all of the measurements in either the positive or negative direction.

1. Example 9 - Four-Strip Domain with Signal Noise

In the ninth example a domain comprised of four strips of different cross sections is considered where 0.01%, 0.10%, and 1.00% signal noise is applied to the measured angular fluxes. The geometry consists of a 4x4 material mesh where all sixteen of these parameters are independently reconstructed. The cross sections of the four regions are 0.9, 1.0, 1.1 and 0.9, respectively. The initial guess for the domain was a homogeneous 1.5 and eight experiments with each beam encompassing half of a side were modeled. A list of the parameters that define the geometry, discretization scheme, reconstructed cross sections and source positions for the problem can be seen in Table VI-XI.

Table VI-XI.: Parameter Description of Four-Strip Domain with Signal Noise

Angular Quadrature (Sn)	8
Domain Sizes (cm)	4x4
Number of Material Regions	4
Material Mesh	4x4
Flux Mesh	32x32
Number of Searched Parameters	16
Actual Cross Section of Material 1 (cm^{-1})	0.9
Actual Cross Section of Material 2 (cm^{-1})	1.0
Actual Cross Section of Material 3 (cm^{-1})	1.1
Actual Cross Section of Material 4 (cm^{-1})	0.9
Homogeneous Initial Guess for Cross Section (cm^{-1})	1.5
Illuminating Source Intensity ($\frac{n}{(cm^2 - sr)}$)	100
Illuminating Sources	8-exp, 1/2-side each
Multiplicative Signal Noise (%)	0.01, 0.1, 1.0

In Fig. VI-34, the results of the four bar domain reconstruction can be seen with 0.01%, 0.10%, and 1.00% signal noise. As is to be expected, the reconstructed image possesses much less accuracy when more noise is applied to the measured angular fluxes. The error plots seen in Fig. VI-35 also evidence this trend. An additional termination criteria was required so that Newton's method would stop. Based on the amount of signal noise, there is a minimum value of the Lagrangian and objective function that Newton's method can achieve which is generally greater than the convergence tolerance of 10^{-6} used in this thesis. This occurs because Newton's method can not

account for the noise in the synthetic data and will always search for the parameters without the applied noise. This leads to an error between the measured and computed fluxes that can never be removed completely. Therefore, an additional check was introduced to see if the two concurrent values of the Lagrangian and misfit only deviate by less than 10^{-6} , then the optimization routine is terminated.

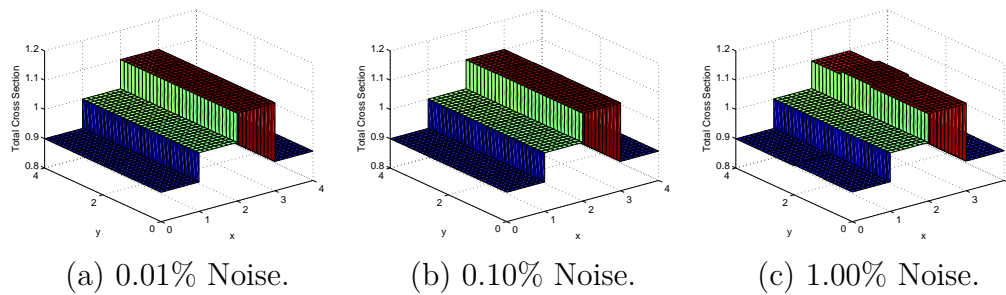


Fig. VI-34.: Reconstructions of Four-Strip Domain with Differing Amounts of Signal Noise.

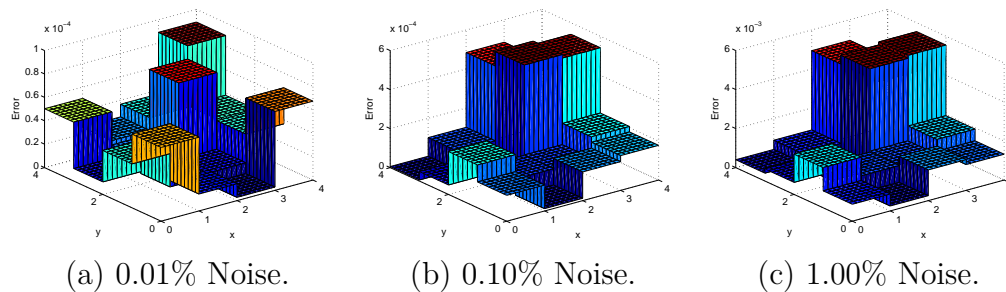


Fig. VI-35.: Error in Reconstructions of Four-Strip Domain with Differing Amounts of Signal Noise.

2. Example 10 - Central Inclusion with Signal Noise and Positive and Negative Signal Bias

In the tenth example a domain comprised of a central inclusion and surrounding medium is considered where only signal noise is applied, noise and positive signal bias are applied or noise and negative signal bias are applied to the measured angular fluxes. In the first set of cases, 0.01%, 0.10%, and 1.00% signal noise is applied to the measured angular fluxes. In the second set of cases, 0.10% signal noise and either 1.00% or 5.00% positive signal bias is applied to the measured angular fluxes. In the third set of cases, 0.10% signal noise and either 1.00% or 5.00% negative signal bias is applied to the measured angular fluxes. However, the geometry of the model remains the same for all of these studies and it consists of a 4x4 material mesh where all sixteen of these parameters are independently reconstructed. The cross sections of the two regions are 1.0 and 1.3, respectively. The initial guess for the domain was a homogeneous 1.5 and eight experiments with each beam encompassing half of a side were modeled. A list of the parameters that define the geometry, discretization scheme, reconstructed cross sections and source positions for the problem can be seen in Table VI-XII.

Table VI-XII.: Parameter Description of Central Inclusion Domain with Signal Noise and Signal Bias

Angular Quadrature (S_n)	8
Domain Sizes (cm)	4x4
Number of Material Regions	2
Material Mesh	4x4
Flux Mesh	8x8
Number of Searched Parameters	16
Actual Cross Section of Surroundings (cm^{-1})	1.0
Actual Cross Section of Inclusion (cm^{-1})	1.3
Homogeneous Initial Guess for Cross Section (cm^{-1})	1.5
Illuminating Source Intensity ($\frac{n}{(cm^2-Sr)}$)	100
Illuminating Sources	8-exp, 1/2-side each
Multiplicative Signal Noise (%)	0.01, 0.10, 1.00
Positive Signal Bias (%)	1.00, 5.00
Negative Signal Bias (%)	1.00, 5.00

Figs. VI-36 and VI-37 display the reconstruction and error results for the noise only studies where 0.01%, 0.10%, and 1.00% signal noise is applied to the measured angular fluxes. As expected, the quality of the reconstruction and the amount of error as more signal noise is imposed. The effects of the signal noise on the reconstructed cross sections are nearly unnoticeable for the models with 0.01% and 0.10% signal noise. The effects are more prominent in the case with 1.00% signal noise. The images were generated in 8.4, 9.9 and 10.5 minutes for the 0.01%, 0.10%, and 1.00% signal noise

cases, respectively. The 0.01% and 0.10% signal noise studies required seventy-one iterations and the 1.00% signal noise study required seventy-five iterations.

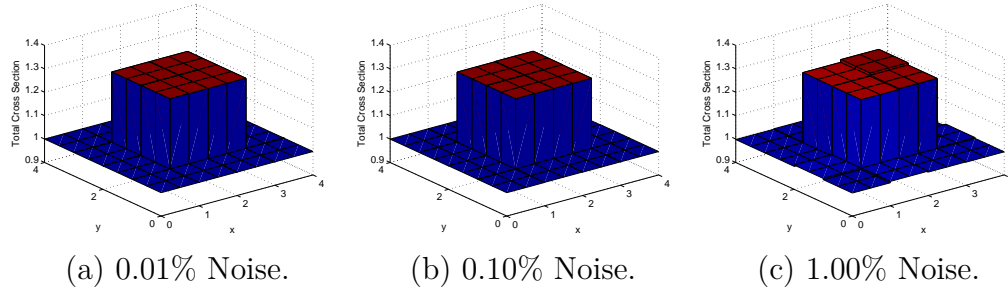


Fig. VI-36.: Reconstruction of Central Inclusion Domain with Differing Amounts of Signal Noise.

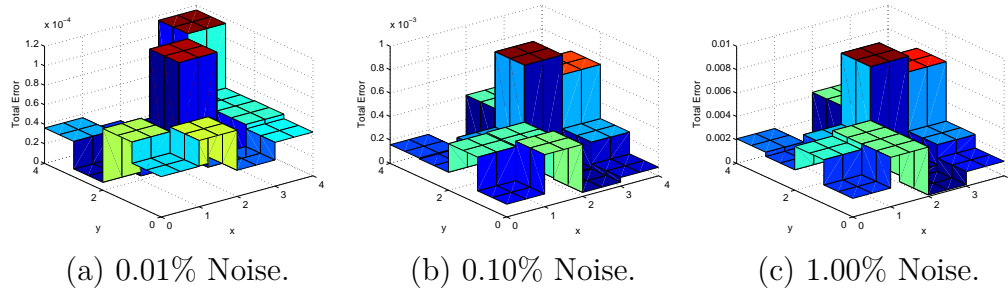


Fig. VI-37.: Error in Reconstruction of Central Inclusion Domain with Differing Amounts of Signal Noise.

Figs. VI-38 and VI-39 display the reconstruction and error results for the signal noise and positive signal bias studies where 0.10% signal noise and 1.00% or 5.00% signal bias are applied to the measured angular fluxes. Since positive signal bias has the effect of increasing all of the measured fluxes by some constant value, the effects are rather apparent in the reconstruction and error results. In the reconstructions for the positive signal bias cases, the reconstructed central inclusion region is lower by approximately 1.00% or 5.00% than the actual cross section of this region of 1.3.

These results make sense because if the measurements are influenced by positive signal bias, then the fluxes are 1.00% or 5.00% higher than they would be if the bias was not present. This implies that the inverse transport method should predict 1.00% or 5.00% less absorption to occur in this region of the domain and this is the case. The cells in the corners of the domain also show this same trend where there predicted values are 1.00% or 5.00% less than if the signal bias was not present. The remaining material regions that lie in the region surrounding the inclusion but not on the corners of the domain are 1.00% or 5.00% more than they would be if the bias was not present. This can be attributed to the fact that the predicted flux distribution with signal bias is still similar to the predicted flux distribution without signal bias and this causes these regions to be elevated to compensate for the decrease in the other cross sections.

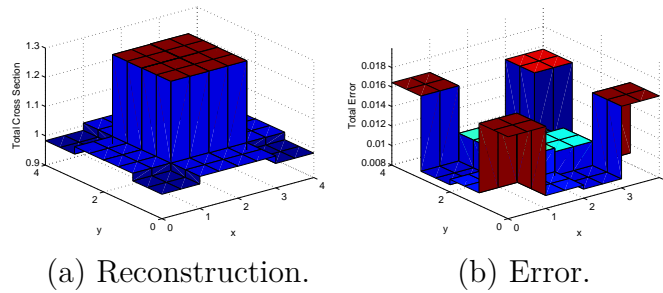


Fig. VI-38.: Central Inclusion Domain with 0.10% Signal Noise and Positive 1.00% Signal Bias.

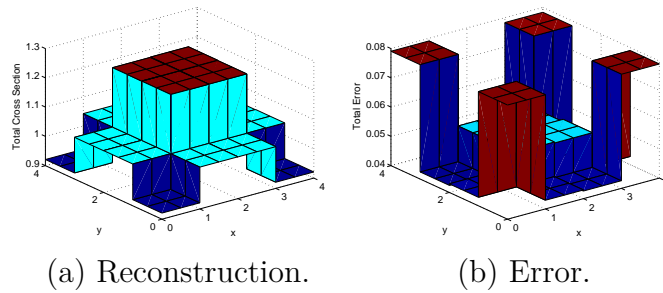


Fig. VI-39.: Central Inclusion Domain with 0.10% Signal Noise and Positive 5.00% Signal Bias.

Figs. VI-40 and VI-41 display the reconstruction and error results for the signal noise and negative signal bias studies where 0.10% signal noise and 1.00% or 5.00% signal bias are applied to the measured angular fluxes. Since negative signal bias has the effect of decreasing all of the measured fluxes by some constant value, the effects are rather apparent in the reconstruction and error results. In the reconstructions for the negative signal bias cases, the reconstructed central inclusion region is higher by approximately 1.00% or 5.00% than the actual cross section of this region of 1.3. These results make sense because if the measurements are influenced by negative signal bias, then the fluxes are 1.00% or 5.00% lower than they would be if the bias was not present. This implies that the inverse transport method should predict 1.00% or 5.00% more absorption to occur in this region of the domain and this is the case. The cells in the corners of the domain also show this same trend where there predicted values are 1.00% or 5.00% more than if the signal bias was not present. The remaining material regions that lie in the region surrounding the inclusion but not on the corners of the domain are 1.00% or 5.00% less than they would be if the bias was not present. This can be attributed to the fact that the predicted flux distribution with signal bias is still similar to the predicted flux distribution without signal bias

and this causes these regions to be decreased to compensate for the increase in the other cross sections.

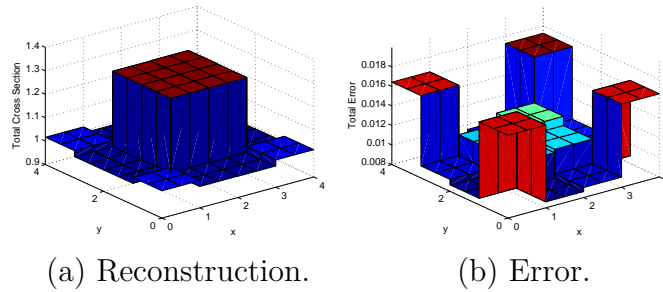


Fig. VI-40.: Central Inclusion Domain with 0.10% Signal Noise and Negative 1.00% Signal Bias.

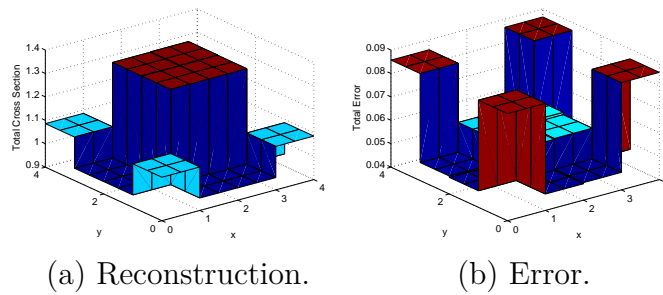


Fig. VI-41.: Central Inclusion Domain with 0.10% Signal Noise and Negative 5.00% Signal Bias.

3. Summary of Findings from Pure Absorbers with Signal Noise and Bias

In this section, the effects of the addition of signal noise and signal bias was explored on some pure absorber problems. Generally, the addition of signal noise and signal bias increased the difficulty in image reconstruction and produced images with greater error. In example 9, a four strip domain was examined where various amounts of signal noise was applied to the synthetic data. Image quality declined as the signal noise

was increased. The need for an additional convergence criteria was required in the reconstructions with signal noise due to the fact that noise represented a minimum amount of error that Newton's method could never eliminate. In example 10, the effects of signal noise and signal bias were examined on a central inclusion problem. The same trend of decreased image quality as the amount of signal noise and bias was increased was also evident for this example. The results seen for the cases with signal bias could be explained by the increased or decreased flux values. An increase in the fluxes would generally imply that less absorption occurred in the domain and visa versa and these trends were apparent in the reconstructions.

D. Problems with Scattering

In this section, the ability of Newton's method to reconstruct the material properties of domains with scattering is examined. In example 11, a two-parameter problem is studied so that the surface of the objective function can be plotted for problems with various amounts of scattering. In example 12, the scattering and total cross sections of a homogeneous domain are reconstructed as eight independent parameters to test Newton's ability to reconstruct a simple domain with scattering. In example 13, the effects of adding signal noise and bias to the reconstruction process for a four-strip domain. In examples 14, 15, 16 and 17 the optical thickness, initial guess, different source locations and different measurement locations example problems are revisited with scattering, respectively. Eight experiments are used in all of the reconstructions in this section with the exception of example 16 where the source locations are varied. In example 16, only one experiment is used in the reconstruction.

1. Example 11 - Scattering Misfit Surface Plots

In the eleventh example the surface of the objective function is considered for a homogeneous domain with constant total and scattering cross sections. This two-parameter problem allows for the misfit surface to be plotted as a function of the scattering and total cross sections. The misfit surface is considered for four different scattering cross sections. These scattering cross sections were determined based on a percentage of the total cross section so that the complete range of low to high scattering medium could be plotted. The scattering percentages considered in these misfit surface plots were 10%, 50%, 90% and 99%. A 50x50 grid of values was used to generate the surface of the objective function and these values ranged from 50% to 200% of the true value of the parameters. The true total cross section was maintained at a value of 1.00 cm^{-1} for all of the studies. Therefore, the true scattering cross sections were 0.10, 0.50, 0.90 and 0.99 cm^{-1} . A list of the parameters that define the geometry, discretization scheme and source positions used to generate these misfit surfaces can be seen in Table VI-XIII.

Table VI-XIII.: Parameter Description of Misfit Surface Geometry

Angular Quadrature (Sn)	8
Domain Size (cm)	4x4
Number of Material Regions	1
Material Mesh	4x4
Flux Mesh	8x8
Number of Searched Parameters	2
True Total Cross Section (cm^{-1})	1.00
True Scattering Cross Section (cm^{-1})	0.10, 0.50, 0.90, 0.99
Number of Guessed Parameter Pairs	2500
Range of Guesses for Total Cross Section (cm^{-1})	0.50-2.00
Range of Guesses for Scattering Cross Section (%)	50-200
Illuminating Source Intensity ($\frac{n}{(cm^2-Sr)}$)	100
Boundaries of Imposed Illuminating Sources	all sides

In Fig. VI-42, the misfit surface that results from the 10% scattering case is presented. With this low amount of scattering, the misfit surface resembles the misfit surface from the pure absorber model seen in example 1. In this case, determining the total cross section is much easier than determining the scattering cross section. This is evidenced by the fact that the misfit surface changes more drastically with changes in the total cross section than with changes in the scattering cross section. The scattering cross section is generally more difficult to reconstruct than the total cross section using Newton's method. Therefore, some of the problems seen in the pure absorber section of this thesis were simplified when it was desired to reconstruct

both the total and scattering cross sections. In addition, because a 50x50 grid of values was used to generate the misfit surface, the combination of cross sections that yeilds the true values was not plotted and no hole is present in the data for any of these figures.

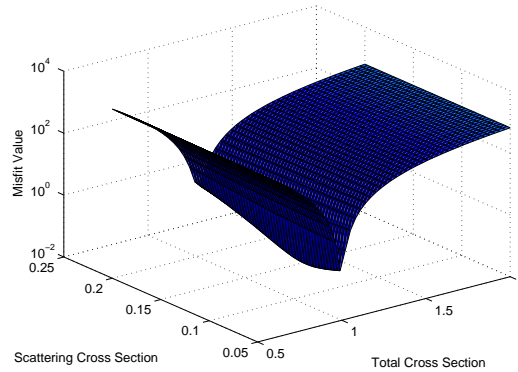


Fig. VI-42.: Misfit Surface Plot with 10% Scattering.

In Fig. VI-43, the misfit surface that results from the 50% scattering case is presented. The area where the sharp peaks are found can be ingored in this figure because the combination of cross sections that were used to generate these values correspond to a situation where the scattering cross section is larger than the total cross section. Since the scattering cross section can never be larger than the total cross section, these values are non-physical and should be ignored. It can also be noticed that the misfit surface of the case with 50% scattering is very flat and the gradient only changes drastically very near the true value of the parameters. This means that the gradient of the objective function provides little information about the location of the minimum of the objective function unless the proposed values of the parameters is very near the true parameters. This displays the difficulty of the optimization problem where both the total and scattering cross section are to be reconstructed and one may expect slow convergence for initial guesses that are far

from the actual solution.

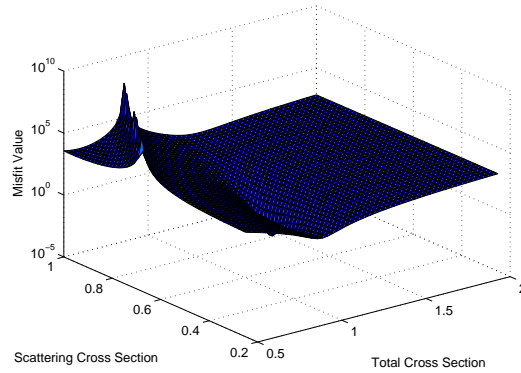


Fig. VI-43.: Misfit Surface Plot with 50% Scattering.

In Fig. VI-44, the misfit surface that results from the 90% scattering case is presented. Again some non-physical parameters combinations have been plotted and these should be ignored. The valley of the misfit where the minimum is located has now rotated so that it runs along a line that approximately corresponds to when the scattering cross section is equal to the total cross section. Again it can be seen that misfit surface is rather flat everywhere except near the misfit valley.

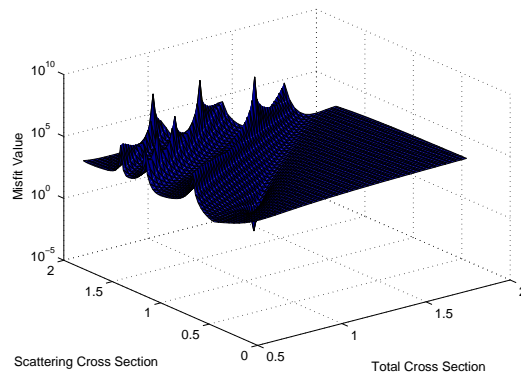


Fig. VI-44.: Misfit Surface Plot with 90% Scattering.

In Fig. VI-45, the misfit surface that results from the 99% scattering case is

presented. Again some non-physical parameters combinations have been plotted and these should be ignored. The valley of the misfit where the minimum is located runs along a line that approximately corresponds to when the scattering cross section is equal to the total cross section.

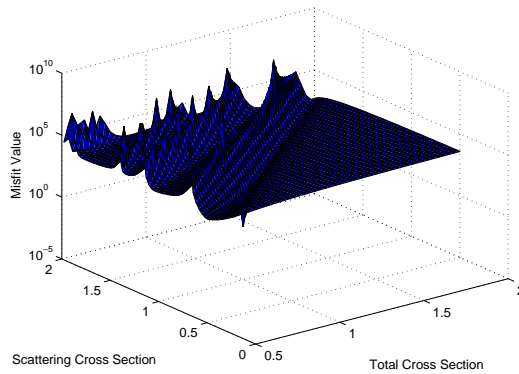


Fig. VI-45.: Misfit Surface Plot with 99% Scattering.

2. Example 12 - 8-Parameter Homogeneous Domain

In example 12, a domain with true total and scattering cross section distributions that are homogeneous is reconstructed as four distinct material regions or an 8-parameter problem. This simple problem serves as an introduction to the process of reconstructing both the scattering and total cross sections simultaneously. This inverse transport problem was conducted for three different scattering cross sections of 0.10, 0.50 and 0.90 cm^{-1} . In all cases the total cross section was maintained at a constant 1.00 cm^{-1} . An initial guess of 1.50 cm^{-1} was proposed for the values of all of the scattering and total cross sections in each of the studies in this example. A list of the parameters that define the geometry, discretization scheme, reconstructed cross sections and source positions for the problem can be seen in Table VI-XIV.

Table VI-XIV.: Parameter Description of Homogeneous Domain with Scattering

Angular Quadrature (Sn)	8
Domain Size (cm)	4x4
Number of Material Regions	1
Material Mesh	4x4
Flux Mesh	16x16
Number of Searched Parameters	8
Actual Total Cross Section (cm^{-1})	1.00
Actual Scattering Cross Section (cm^{-1})	0.10, 0.50, 0.90
Homogeneous Initial Guess for Total Cross Sections (cm^{-1})	1.50
Homogeneous Initial Guess for Scattering Cross Sections (cm^{-1})	1.50
Illuminating Source Intensity ($\frac{n}{(cm^2-Sr)}$)	100
Illuminating Sources	all sides

Figs. VI-46 and VI-47 display the reconstructions and errors for the total and scattering cross sections for the problem with 10% scattering. The reconstruction was successful and the maximum error was determined to be on the order of 10^{-5} and 10^{-6} for the total and scattering cross sections, respectively. The reconstruction was completed in one hundred and twenty-six iterations in fifty-three hours.

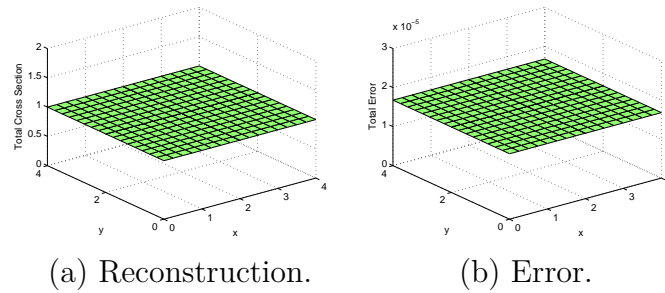


Fig. VI-46.: Total Cross Section Reconstruction for the 8-Parameter Homogeneous Domain with 10% Scattering.

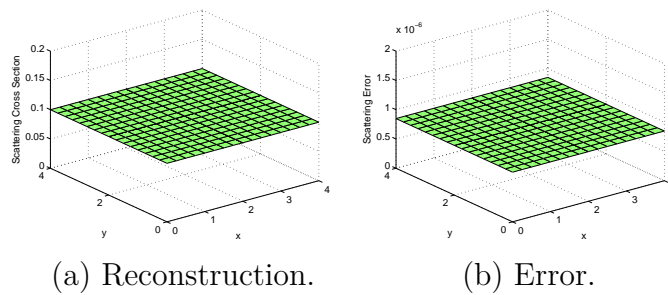


Fig. VI-47.: Scattering Cross Section Reconstruction for the 8-Parameter Homogeneous Domain with 10% Scattering.

Figs. VI-48 and VI-49 display the reconstructions and errors for the total and scattering cross sections for the problem with 50% scattering. The reconstruction was successful and the maximum error was determined to be on the order of 10^{-5} for the total and scattering cross sections. The reconstruction was completed in one hundred and twenty-six iterations in fifty-two hours.

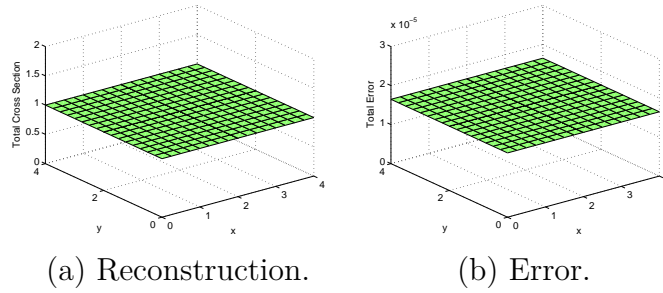


Fig. VI-48.: Total Cross Section Reconstruction for the 8-Parameter Homogeneous Domain with 50% Scattering.

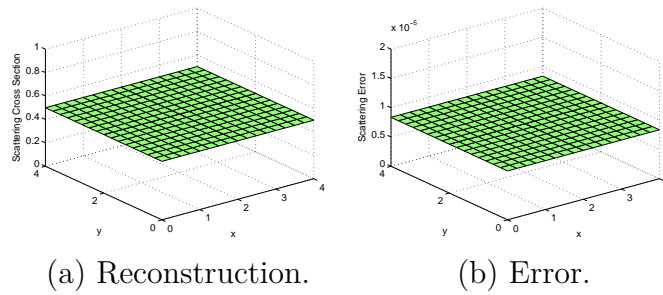


Fig. VI-49.: Scattering Cross Section Reconstruction for the 8-Parameter Homogeneous Domain with 50% Scattering.

Figs. VI-50 and VI-51 display the reconstructions and errors for the total and scattering cross sections for the problem with 90% scattering. The reconstruction was successful and the maximum error was determined to be on the order of 10^{-5} for both the total and scattering cross sections. The reconstruction was completed in eighty-six iterations in thirty-six hours.

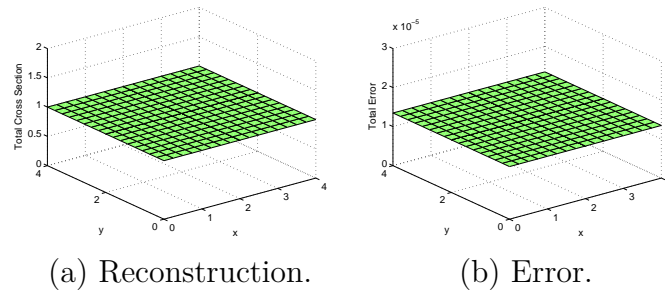


Fig. VI-50.: Total Cross Section Reconstruction for the 8-Parameter Homogeneous Domain with 90% Scattering.

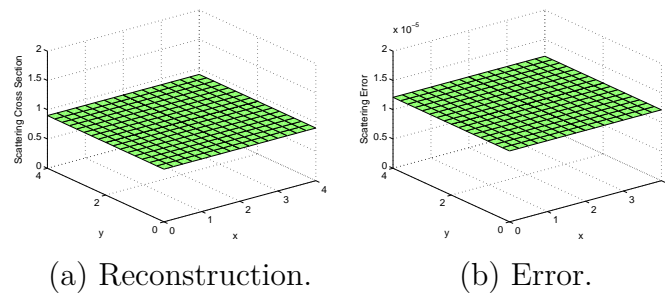


Fig. VI-51.: Scattering Cross Section Reconstruction for the 8-Parameter Homogeneous Domain with 90% Scattering.

Because of the extremely long solve times of fifty-three, fifty-two and thirty-six hours for this simple homogeneous problem, the transport function was optimized so that computational time could be reduced. This optimization process consisted of calculating only once and storing the large matrices that do not change with each iteration of the the transport operator. Significant performance improvements were noticed after this optimization was conducted and this explains why solution time are significantly reduced in the following problems.

3. Example 13 - Four-Strip Domain with No Signal Noise, Only Noise, and Both Noise and Bias

In example 13, a four strip domain is considered with no signal noise, with only signal noise and with both signal noise and signal bias. This four strip domain is grouped into eight distinct regions where both the total and scattering cross sections are reconstructed. This simulation was conducted with eight experiments each covering half of a side and the scattering percentage was maintained at 90% of the total cross section for all regions in all of the studies conducted in this section. Homogeneous initial parameter distributions of 1.2 and 1.1 cm^{-1} were used as the starting points for the reconstructions of the total and scattering cross sections, respectively. A list of the parameters that define the geometry, discretization scheme, reconstructed cross sections, source positions and applied signal noise and bias for the problem can be seen in Table VI-XV.

Table VI-XV.: Parameter Description of Four-Strip Domain with Signal Noise and Bias

Angular Quadrature (Sn)	8
Domain Sizes (cm)	4x4
Number of Material Regions	4
Material Mesh	4x4
Flux Mesh	8x8
Number of Searched Parameters	16
Actual Total Cross Section of Material 1 (cm^{-1})	0.90
Actual Total Cross Section of Material 2 (cm^{-1})	1.00
Actual Total Cross Section of Material 3 (cm^{-1})	1.10
Actual Total Cross Section of Material 4 (cm^{-1})	0.90
Actual Scattering Ratio for All Materials (c)	0.90
Homogeneous Initial Guess for Total Cross Sections (cm^{-1})	1.20
Homogeneous Initial Guess for Scattering Cross Sections (cm^{-1})	1.10
Illuminating Source Intensity ($\frac{n}{(cm^2-Sr)}$)	100
Illuminating Sources	8-exp, 1/2-side each
Multiplicative Signal Noise (%)	0.01, 0.1, 1.0
Positive Signal Bias (%)	1.00, 5.00
Negative Signal Bias (%)	1.00, 5.00

Figs. VI-52 and VI-53 display the reconstructions and errors for the total and

scattering cross sections for the baseline case where no signal noise or bias has been applied to the measured fluxes. The reconstruction was successful and the generated image possessed error on the order of 10^{-5} for both the scattering and total cross sections. This reconstruction was completed in 54 iterations lasting just under three hours.

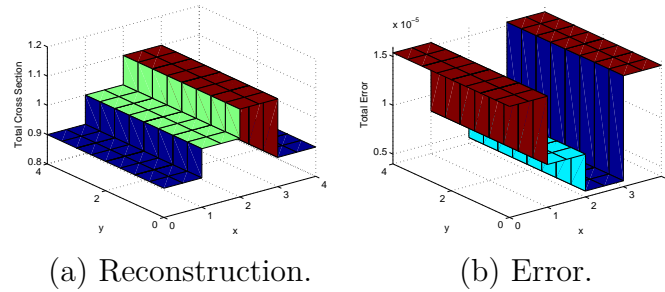


Fig. VI-52.: Total Cross Section Reconstruction Results for Four-Strip Domain without Signal Noise.

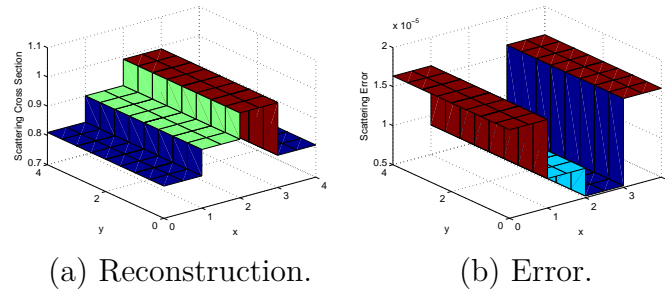


Fig. VI-53.: Scattering Cross Section Reconstruction Results for Four-Strip Domain without Signal Noise.

Figs. VI-54 and VI-55 display the reconstructions and errors for the total and scattering cross sections for the case where 0.01% signal noise has been applied to the measured fluxes. As expected, more error is introduced into the reconstruction due to this signal noise and the resulting error in the total cross section has quadrupled

and resulting error in the scattering cross section has tripled as compared with the baseline case. This reconstruction was completed in fifty-one iterations lasting three hours.

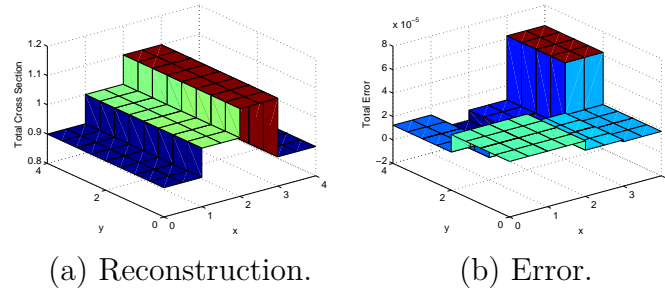


Fig. VI-54.: Total Cross Section Reconstruction Results for Four-Strip Domain with 0.01% Signal Noise.

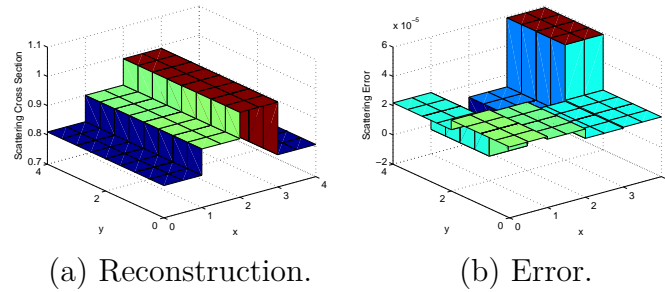


Fig. VI-55.: Scattering Cross Section Reconstruction Results for Four-Strip Domain with 0.01% Signal Noise.

Figs. VI-56 and VI-57 display the reconstructions and errors for the total and scattering cross sections for the case where 0.10% signal noise has been applied to the measured fluxes. Again, the quality of the reconstructions has further diminished with the addition of more signal noise. The error seen in both the scattering and total cross sections is now on the order of 10^{-4} . This reconstruction was completed in 51 iterations lasting two hours and forty-five minutes.

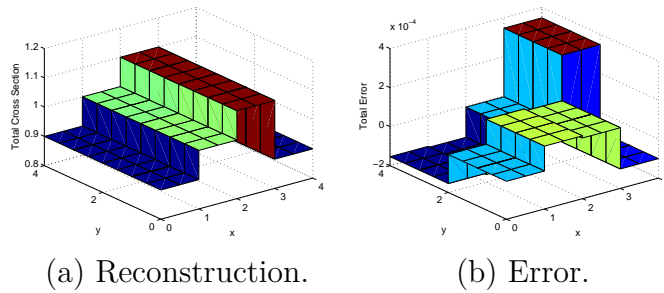


Fig. VI-56.: Total Cross Section Reconstruction Results for Four-Strip Domain with 0.10% Signal Noise.

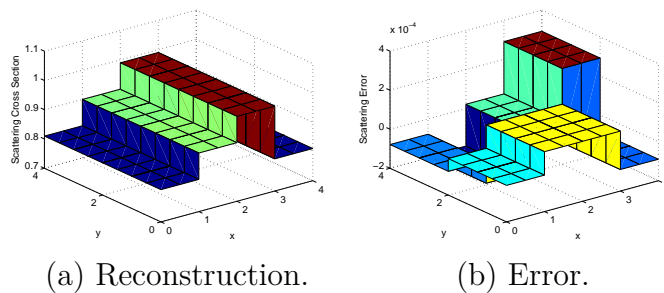


Fig. VI-57.: Scattering Cross Section Reconstruction Results for Four-Strip Domain with 0.10% Signal Noise.

Figs. VI-58 and VI-59 display the reconstructions and errors for the total and scattering cross sections for the case where 1.00% signal noise has been applied to the measured fluxes. The error in the reconstruction has increased by another order of magnitude due to the addition more signal noise and is now on the order of 10^{-3} . This reconstruction was completed in 49 iterations lasting just under three hours.

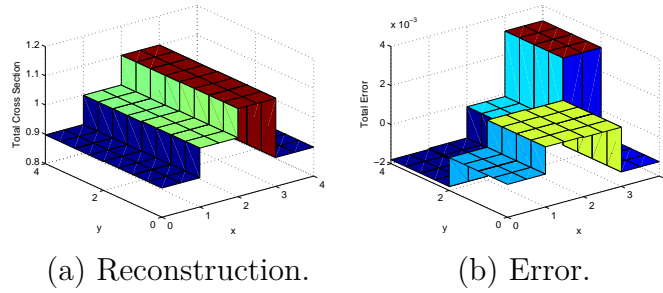


Fig. VI-58.: Total Cross Section Reconstruction Results for Four-Strip Domain with 1.00% Signal Noise.

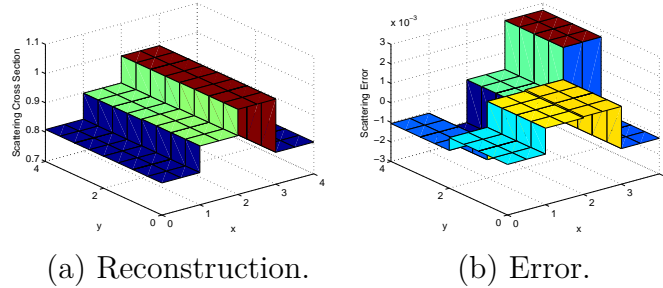


Fig. VI-59.: Scattering Cross Section Reconstruction Results for Four-Strip Domain with 1.00% Signal Noise.

Figs. VI-60 and VI-61 display the reconstructions and errors for the total and scattering cross sections for the case where 0.10% noise and 1.00% positive signal bias has been applied to the measured fluxes. The error was further increased by the addition of signal bias and is on the order of 10^{-3} . The positive signal bias had the effect of shifting the predicted value of the middle two strips by about 1.00% and decreasing the predicted value of the outer two strips by about 1.00%. The shape of the error produced from this case with positive bias resembles the shape of the error for the baseline case for both the scattering and total cross sections. The major differences between the errors seen in this case and the baseline case are that the

baseline case has no noise so the predicted values of the cross sections are uniform within each region of the domain. Also because of the bias, the error has been scaled and is much larger in magnitude for the case with bias. This reconstruction was completed in 49 iterations lasting just under three hours.

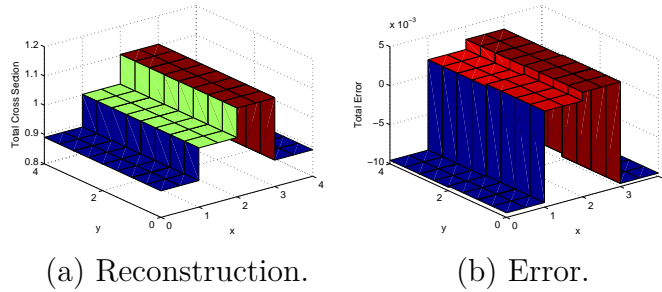


Fig. VI-60.: Total Cross Section Reconstruction Results for Four-Strip Domain with 0.10% Signal Noise and 1.00% Positive Signal Bias.

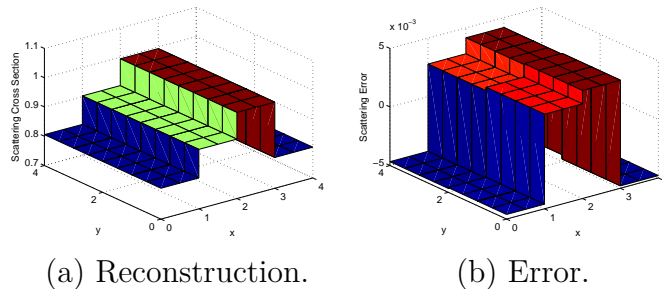


Fig. VI-61.: Scattering Cross Section Reconstruction Results for Four-Strip Domain with 0.10% Signal Noise and 1.00% Positive Signal Bias.

Table VI-XVI displays the average total and scattering cross section values for the true and reconstructed domains. This table displays the trend that as positive signal bias is added, this has the effect of increasing the magnitude of all of the angular fluxes. This then has the effect of decreasing the apparent amount absorption occurring within the domain and decreases the values of the reconstructed cross sections. This

can be seen in Table VI-XVI as the values of the reconstructed total and scattering cross sections are lower in magnitude than their respective true values.

Table VI-XVI.: Average Cross Section Comparison for Four-Strip Domain with 0.10% Signal Noise and 1.00% Positive Signal Bias

Average True Total Cross Section (cm^{-1})	0.9750
Average Reconstructed Total Cross Section (cm^{-1})	0.9717
Average True Scattering Cross Section (cm^{-1})	0.8775
Average Reconstructed Scattering Cross Section (cm^{-1})	0.8770

Figs. VI-62 and VI-63 display the reconstructions and errors for the total and scattering cross sections for the case where 0.10% noise and 5.00% positive signal bias has been applied to the measured fluxes. The error was further increased by the addition of signal bias and is on the order of 10^{-2} . The positive signal bias had the effect of shifting the predicted value of the middle two strips by about 5.00% and decreasing the predicted value of the outer two strips by about 5.00%. Again, the shape of the error produced from this case is similar to the error seen in the baseline and 1.00% positive bias case where the majority of the reconstruction error occurs in the outer strips of the domain. This reconstruction did not converge in five hundred iterations because the Lagrangian was still changing more 10^{-6} between consecutive iterations. These 500 iterations lasted twenty-seven hours.

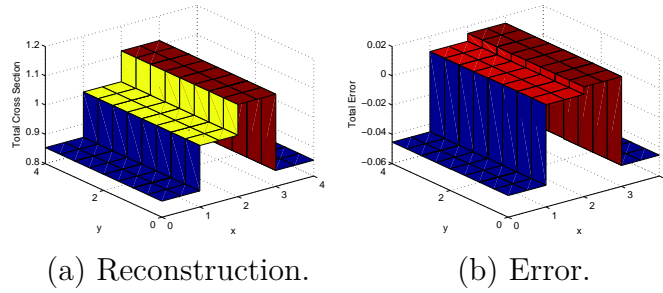


Fig. VI-62.: Total Cross Section Reconstruction Results for Four-Strip Domain with 0.10% Signal Noise and 5.00% Positive Signal Bias.

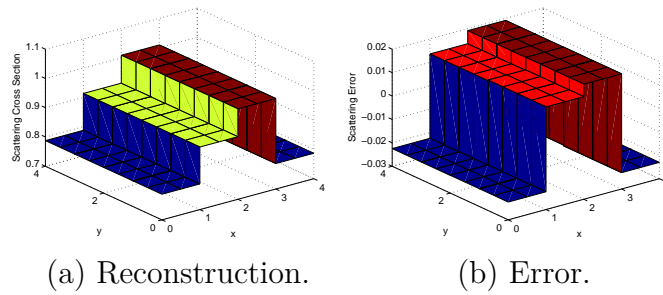


Fig. VI-63.: Scattering Cross Section Reconstruction Results for Four-Strip Domain with 0.10% Signal Noise and 5.00% Positive Signal Bias.

Table VI-XVII displays the average total and scattering cross section values for the true and reconstructed domains. This table again displays the trend that as positive signal bias is added to the measured angular fluxes, the values of the reconstructed cross sections are decreased. Table VI-XVII shows this trend as the values of the reconstructed total and scattering cross sections are lower in magnitude than their respective true values. The average values of the reconstructed cross sections are also reduced as more positive signal bias is added to the fluxes.

Table VI-XVII.: Average Cross Section Comparison for Four-Strip Domain with 0.10% Signal Noise and 5.00% Positive Signal Bias

Average True Total Cross Section (cm^{-1})	0.9750
Average Reconstructed Total Cross Section (cm^{-1})	0.9585
Average True Scattering Cross Section (cm^{-1})	0.8775
Average Reconstructed Scattering Cross Section (cm^{-1})	0.8744

Figs. VI-64 and VI-65 display the reconstructions and errors for the total and scattering cross sections for the case where 0.10% noise and 1.00% negative signal bias has been applied to the measured fluxes. The error is on the order of 10^{-2} for the total cross sections and 10^{-3} for the scattering cross sections. The negative signal bias had the opposite effect of the positive bias and decreased the predicted value of the middle two strips by about 5.00% and increased the predicted value of the outer two strips by about 5.00%. The shape of the error produced from this case is similar to the error seen in the baseline case where the majority of the reconstruction error occurs in the outer strips of the domain. This reconstruction was completed in 42 iterations lasting about two hours.

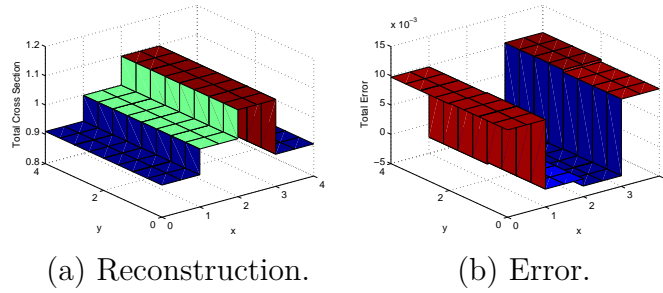


Fig. VI-64.: Total Cross Section Reconstruction Results for Four-Strip Domain with 0.10% Signal Noise and 1.00% Negative Signal Bias.

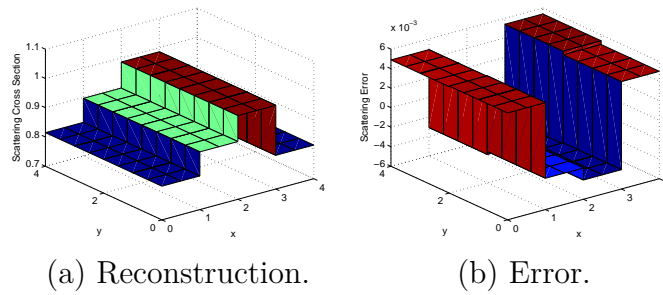


Fig. VI-65.: Scattering Cross Section Reconstruction Results for Four-Strip Domain with 0.10% Signal Noise and 1.00% Negative Signal Bias.

Table VI-XVIII displays the average total and scattering cross section values for the true and reconstructed domains. This table displays the opposite trend that as negative signal bias is added, this has the effect of decreasing the magnitude of all of the angular fluxes. This then has the effect of increasing the apparent amount absorption occurring within the domain and increases the values of the reconstructed cross sections. This can be seen in Table VI-XVIII as the values of the reconstructed total and scattering cross sections are lower in magnitude than their respective true values.

Table VI-XVIII.: Average Cross Section Comparison for Four-Strip Domain with 0.10% Signal Noise and 1.00% Negative Signal Bias

Average True Total Cross Section (cm^{-1})	0.9750
Average Reconstructed Total Cross Section (cm^{-1})	0.9787
Average True Scattering Cross Section (cm^{-1})	0.8775
Average Reconstructed Scattering Cross Section (cm^{-1})	0.8783

Figs. VI-66 and VI-67 display the reconstructions and errors for the total and scattering cross sections for the case where 0.10% noise and 5.00% negative signal bias has been applied to the measured fluxes. The error is on the order of 10^{-2} for the total and scattering cross sections. Again, the reconstruction of the domain underpredicted the values of the middle two strips by about 5.00% and overpredicted the values of the outer two strips by about 5.00%. The shape of the error produced from this case is similar to the error seen in the baseline and the other bias cases where the majority of the reconstruction error occurs in the outer strips of the domain. This reconstruction was completed in 220 iterations lasting about ten hours and forty-five minutes.

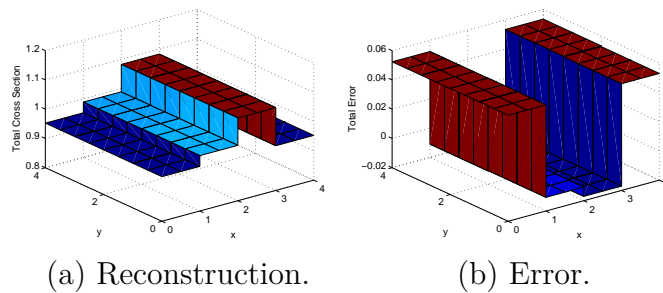


Fig. VI-66.: Total Cross Section Reconstruction Results for Four-Strip Domain with 0.10% Signal Noise and 5.00% Negative Signal Bias.

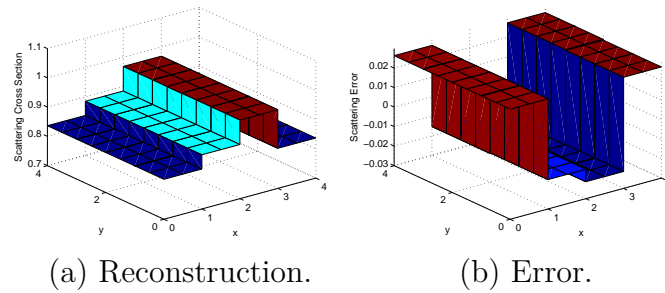


Fig. VI-67.: Scattering Cross Section Reconstruction Results for Four-Strip Domain with 0.10% Signal Noise and 5.00% Negative Signal Bias.

Table VI-XIX displays the average total and scattering cross section values for the true and reconstructed domains. This table again displays the trend that as negative signal bias is added to the measured angular fluxes, the values of the reconstructed cross sections are increased. Table VI-XIX shows this trend as the values of the reconstructed total and scattering cross sections are greater in magnitude than their respective true values. The average values of the reconstructed cross sections are also increased as more negative signal bias is added to the fluxes.

Table VI-XIX.: Average Cross Section Comparison for Four-Strip Domain with 0.10% Signal Noise and 5.00% Negative Signal Bias

Average True Total Cross Section (cm^{-1})	0.9750
Average Reconstructed Total Cross Section (cm^{-1})	0.9944
Average True Scattering Cross Section (cm^{-1})	0.8775
Average Reconstructed Scattering Cross Section (cm^{-1})	0.8818

4. Example 14 - Central Inclusion Optical Thickness Study Reconstructing Both Scattering and Total Cross Sections

In example 14, central inclusion problems of increasing size are examined to determine the optical thickness limit for problems with scattering. In these problems, both the total and scattering cross sections of the central inclusion and surrounding regions are reconstructed using eight experiments. These problems generally required significantly longer computational times than the pure absorber central inclusion problems even after the code optimization had been conducted. The introduction of scattering within the domain increased the complexity of the problem and a much lower optical thickness limit was discovered. A list of the parameters that define the geometry, discretization scheme, reconstructed cross sections and source positions for the problem can be seen in Table VI-XX.

Table VI-XX.: Parameter Description of Central Inclusion Domains with 8 Experiments and Scattering

Angular Quadrature (Sn)	8
Domain Sizes (cm)	4x4, 6x6
Number of Material Regions	2
Material Mesh	4x4, 6x6
Flux Mesh	8x8, 12x12
Number of Searched Parameters	4
Actual Total Cross Section of Surroundings (cm^{-1})	0.90
Actual Total Cross Section of Inclusion (cm^{-1})	1.30
Actual Scattering Cross Section of Surroundings (cm^{-1})	0.45
Actual Scattering Cross Section of Inclusion (cm^{-1})	0.65
Initial Guess for Inclusion Total Cross Section (cm^{-1})	1.50
Initial Guess for Inclusion Scattering Cross Section (cm^{-1})	0.85
Illuminating Source Intensity ($\frac{n}{(cm^2-Sr)}$)	100
Illuminating Sources	8-exp, 1/2-side each

Figs. VI-68 and VI-69 display the reconstructions and errors for the total and scattering cross sections of the 4x4cm central inclusion domain. Newton's method was able to reconstruct all four of the cross sections that define this domain. The history of the condition numbers for the 23 Newton iterations can be seen in VI-69c.

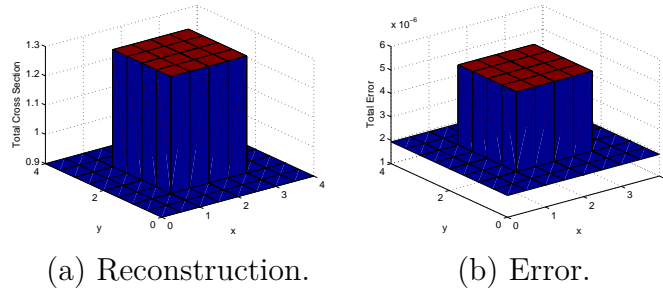


Fig. VI-68.: Total Cross Sections Results for the 4x4cm Central Inclusion Domain.

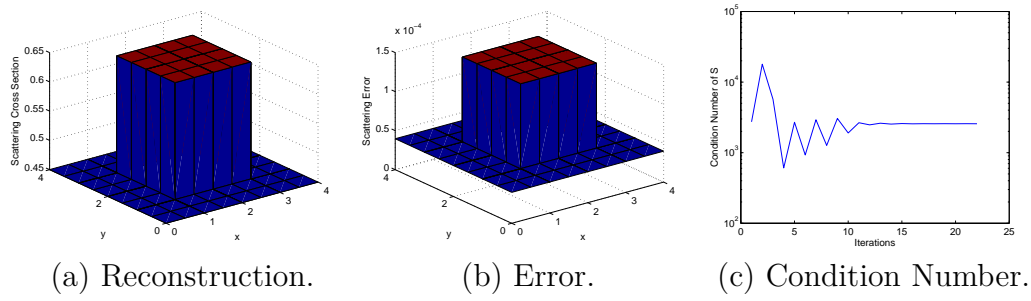


Fig. VI-69.: Scattering Cross Sections Results for the 4x4cm Central Inclusion Domain.

Figs. VI-70 and VI-71 display the reconstructions and errors for the total and scattering cross sections of the 6x6cm central inclusion domain. Newton's method failed to reconstruct the cross sections of the 6x6cm domain. In this slightly optically thicker problem, the values of the cross sections of the central inclusion region contribute even less to the value of the objective function. Because of this, changing the value of the scattering cross section does not affect the value of the misfit and Newton's method begins to propose negative values for this cross section. The negative cross section backtrack mentioned in Chapter IV was employed, but a minimum value of 10^{-4} for the line search parameter α was applied as well. So a negative scattering cross section of the inclusion region was eventually proposed because of this mini-

mum value of the line search parameter. The history of the condition numbers for all 500 Newton iterations can be seen in VI-71c. In this case, the condition number continues to grow with every successive Newton iteration and cross sections will never be reconstructed successfully. Therefore, an optical thickness limit of 2-3 mean free paths has been determined for the central inclusion domain with scattering and eight experiments.

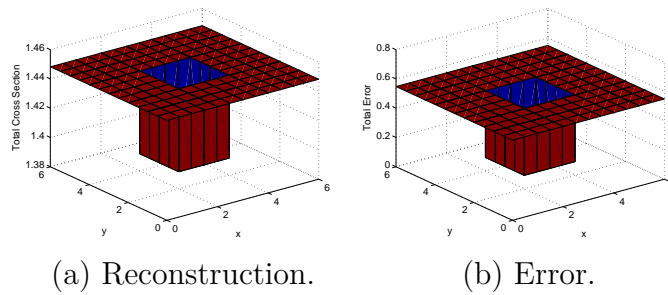


Fig. VI-70.: Total Cross Sections Results for the 6x6cm Central Inclusion Domain.

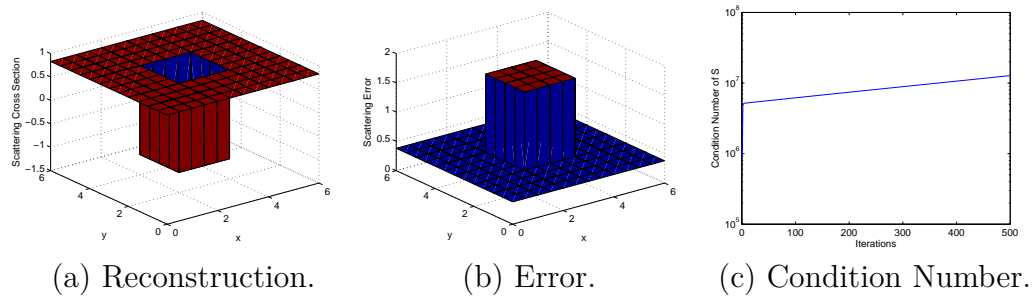


Fig. VI-71.: Scattering Cross Sections Results for the 6x6cm Central Inclusion Domain.

5. Example 15 - Homogeneous Domain Initial Guess Study Reconstructing Both Scattering and Total Cross Sections

In example 15, the sensitivity of Newton's method when reconstructing both the total and scattering cross sections is test on a homogeneous domain. Three different initial guesses are proposed as the starting point for the optimization process starting from the values above and below the actual parameters. The same heuristic procedure was implemented as in the pure absorber initial guess problem where if the optimization process began to stagnate and the line search was only permitting Newton's method to take very small steps, the step size was overwritten and a larger step was taken. This process was almost never required when the actual parameters were approached from above starting from a higher initial guess. This process was frequently required when the actual parameters were approached from below starting from a lower initial guess. A description of the input parameters for the problem for all of the studies conducted in this example as well as the initial parameter distributions used to start the optimization process are described in Table VI-XXI. Again, since the reconstructed domain was homogeneous, the initial guess was generated with random numbers to make it heterogeneous and more challenging for Newton's method.

Table VI-XXI.: Parameter Description of Homogeneous Domain Reconstruction from Various Initial Guesses with Scattering

Angular Quadrature (S_n)	8
Domain Sizes (cm)	4x4
Number of Material Regions	1
Material Mesh	4x4
Flux Mesh	16x16
Number of Searched Parameters	4
Actual Total Cross Section (cm^{-1})	1.0
Actual Scattering Cross Section (cm^{-1})	0.5
Initial Guesses Approaching from Above (%)	1000 ± 200 , 5000 ± 1000 , 10000 ± 2500
Initial Guesses Approaching from Below (%)	90 ± 2 , 80 ± 5 , 50 ± 10
Illuminating Source Intensity ($\frac{n}{(cm^2-Sr)}$)	100
Illuminating Sources	8-exp, 1/2-side each

Figs. VI-72, VI-73, VI-74, VI-75, VI-76 and VI-77 display the initial guess, reconstruction and error results for the scattering and total cross sections of the homogeneous domain starting from an initial guess that is lower than the actual scattering and total cross sections. Figs. VI-72 and VI-73 represent the optimization results when an initial guess of $90\% \pm 2\%$ of the true scattering and total cross sections was used. Figs. VI-74 and VI-75 represent the optimization results when an initial guess of $80\% \pm 5\%$ of the true scattering and total cross sections was used. Figs. VI-76 and VI-77 represent the optimization results when an initial guess of $50\% \pm 10\%$ of the true scattering and total cross sections was used. Newton's method

was able to reconstruct the homogeneous domain from the $90\% \pm 2\%$ and $80\% \pm 5\%$ initial parameters distributions, but it was unable to reconstruct the domain from the $50\% \pm 10\%$ initial guess. In both of the successful reconstructions, the step length was required to be reset many times before the solution was achieved. This again reinforced the trend that Newton's method found it easier to approach the solution from a higher initial guess than a lower one. In addition, the complexity of the scattering problem was emphasized as the proposed initial guesses had to be much closer to the true parameter distribution for the problem with scattering as compared with the pure absorber problems seen in example 7.

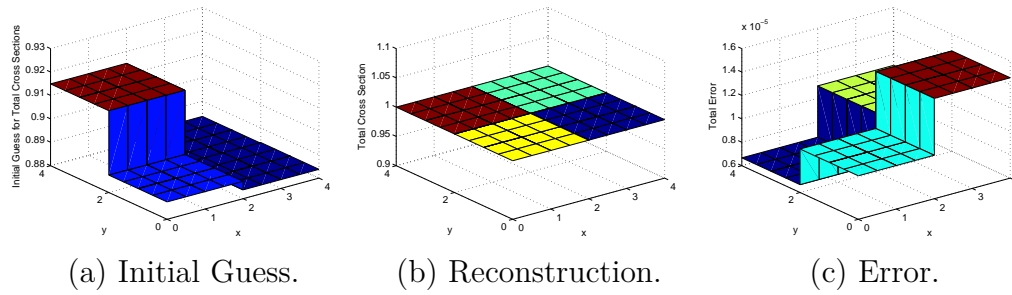


Fig. VI-72.: Initial Guess, Reconstruction and Error Results for Total Cross Section with $90 \pm 2\%$ Initial Guess.

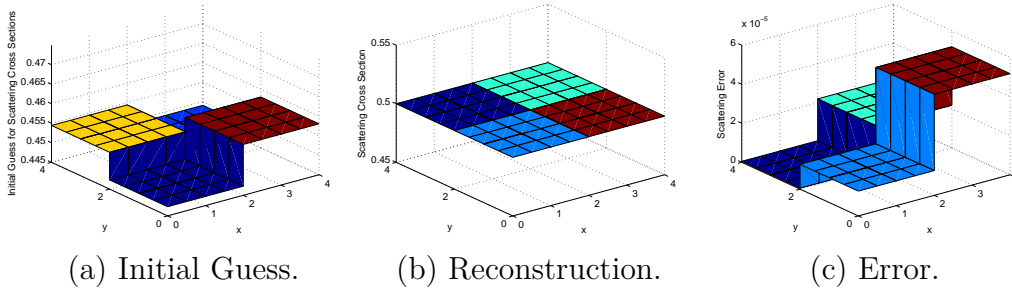


Fig. VI-73.: Initial Guess, Reconstruction and Error Results for Scattering Cross Section with $90 \pm 2\%$ Initial Guess.

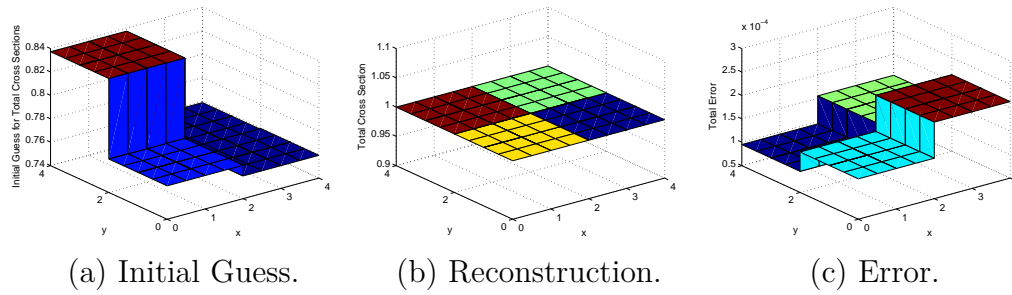


Fig. VI-74.: Initial Guess, Reconstruction and Error Results for Total Cross Section with $80 \pm 5\%$ Initial Guess.

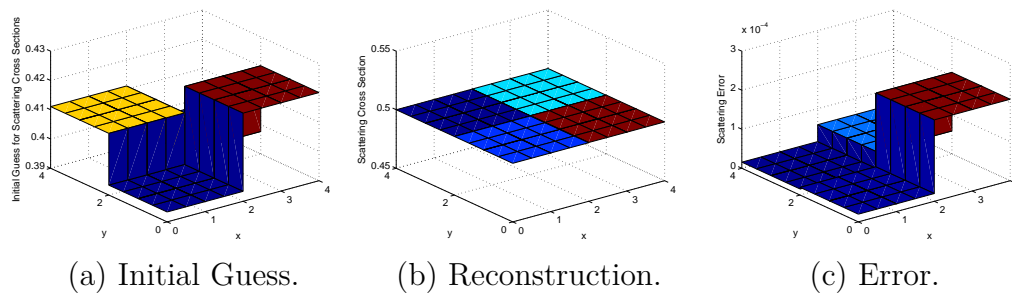


Fig. VI-75.: Initial Guess, Reconstruction and Error Results for Scattering Cross Section with $80 \pm 5\%$ Initial Guess.

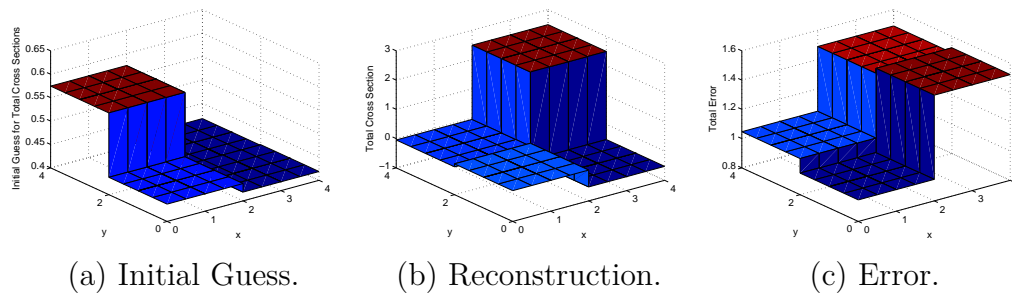


Fig. VI-76.: Initial Guess, Reconstruction and Error Results for Total Cross Section with $50 \pm 10\%$ Initial Guess.

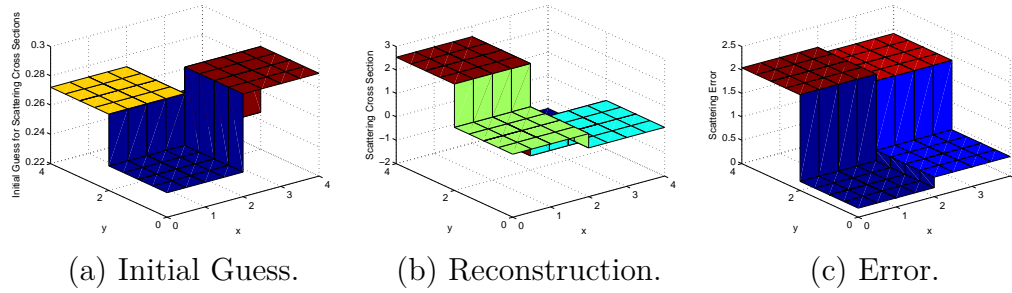


Fig. VI-77.: Initial Guess, Reconstruction and Error Results for Scattering Cross Section with $50 \pm 10\%$ Initial Guess.

Figs. VI-78, VI-79, VI-80, VI-81, VI-82 and VI-83 display the initial guess, reconstruction and error results for the scattering and total cross sections of the homogeneous domain starting from an initial guess that is higher than the actual scattering and total cross sections. Figs. VI-78 and VI-79 represent the optimization results when an initial guess of $1000\% \pm 200\%$ of the true scattering and total cross sections was used. Figs. VI-80 and VI-81 represent the optimization results when an initial guess of $5000\% \pm 1000\%$ of the true scattering and total cross sections was used. Figs. VI-82 and VI-83 represent the optimization results when an initial guess of $10000\% \pm 2500\%$ of the true scattering and total cross sections was used. Newton's method was able to reconstruct the homogeneous domain from the $1000\% \pm 200\%$ and $5000\% \pm 1000\%$ initial parameters distributions, but it was unable to reconstruct the domain from the $10000\% \pm 2500\%$ initial guess. In all of these cases where the initial guess was greater than the true values of the parameters, the lines search method never stagnated and the step length was never reset. This again reinforced the trend that Newton's method found it easier to approach the solution from a higher initial guess than a lower one. The complexity of the scattering problem was emphasized as $10000\% \pm 2500\%$ initial guess was unsuccessful when both the scattering and total

cross sections were reconstructed as compared with the pure absorber problem seen in example 7.

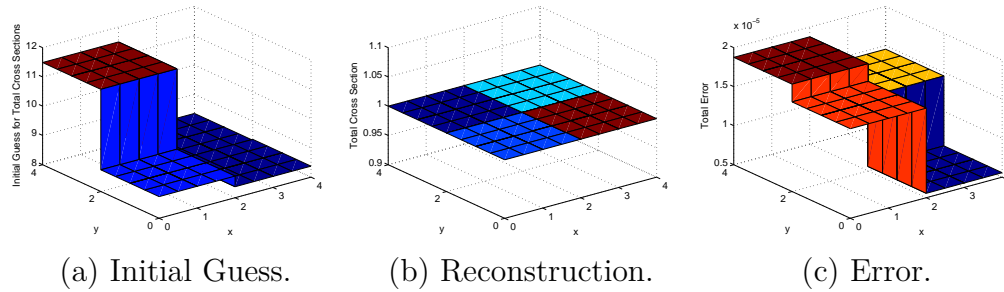


Fig. VI-78.: Initial Guess, Reconstruction and Error Results for Total Cross Section with $1000 \pm 200\%$ Initial Guess.

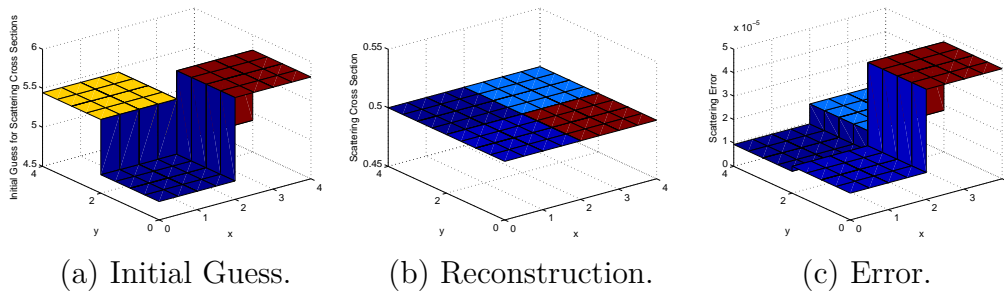


Fig. VI-79.: Initial Guess, Reconstruction and Error Results for Scattering Cross Section with $1000 \pm 200\%$ Initial Guess.

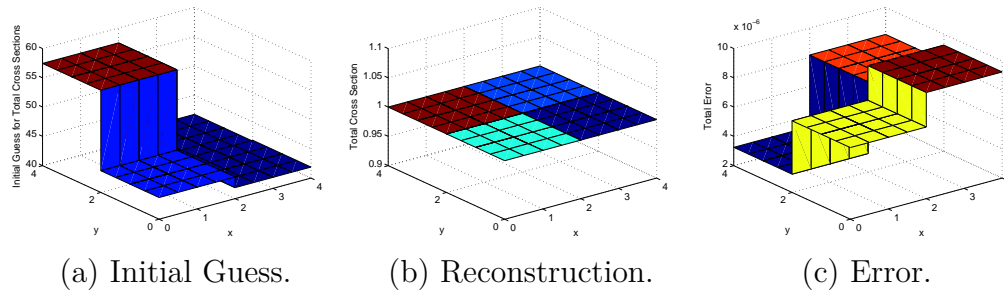


Fig. VI-80.: Initial Guess, Reconstruction and Error Results for Total Cross Section with $5000 \pm 1000\%$ Initial Guess.

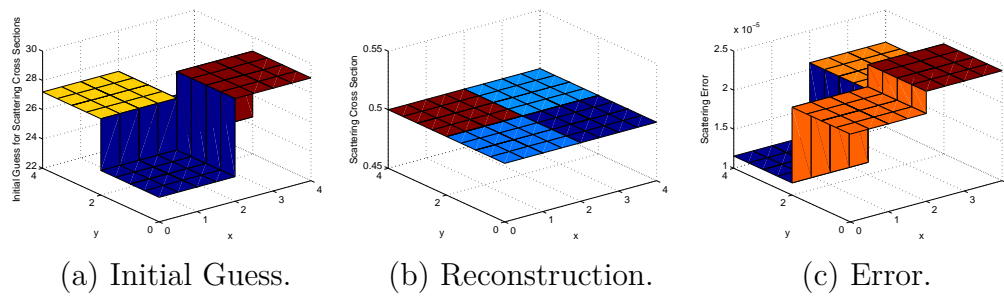


Fig. VI-81.: Initial Guess, Reconstruction and Error Results for Scattering Cross Section with $5000 \pm 1000\%$ Initial Guess.

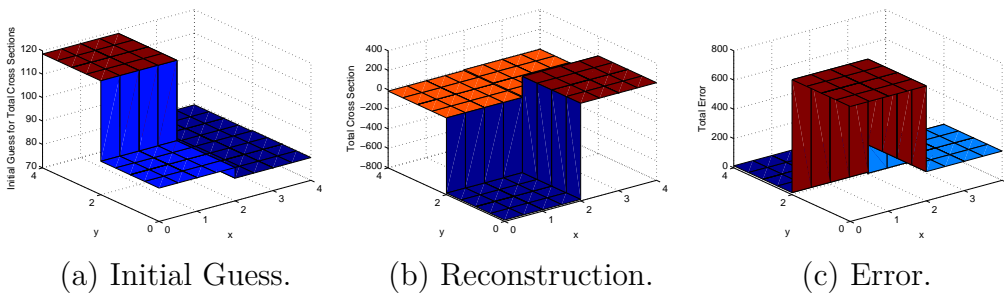


Fig. VI-82.: Initial Guess, Reconstruction and Error Results for Total Cross Section with $10000 \pm 2500\%$ Initial Guess.

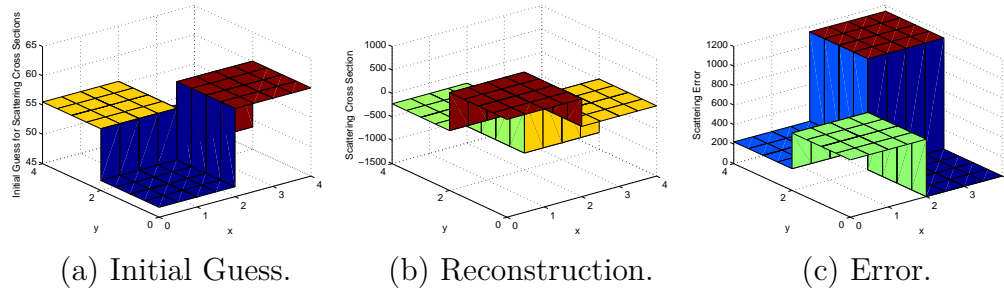


Fig. VI-83.: Initial Guess, Reconstruction and Error Results for Scattering Cross Section with $10000 \pm 2500\%$ Initial Guess.

6. Example 16 - Four-Region Domain with Illuminating Sources on 1, 2, 3 or 4 Sides Reconstructing Both Scattering and Total Cross Sections

In example 16, the effects of imposing sources on different numbers of sides in a single experiment is examined on a four region domain with scattering. The scattering cross sections for the domain were maintained at 50% of the total cross section for all of the studies conducted in this section. The same material region layout and side numbering scheme was used in this example as can be seen in Fig. VI-10 of example 4. A list of the parameters that define the geometry, discretization scheme, reconstructed cross sections and source positions for the problem can be seen in Table VI-XXII.

Table VI-XXII.: Parameter Description of Four-Region Domain with Scatting and Varying Illuminating Sources

Angular Quadrature (Sn)	8
Domain Size (cm)	8x8
Number of Material Regions	4
Material Mesh	4x4
Flux Mesh	16x16
Number of Searched Parameters	8
Actual Total Cross Section of Material 1 (cm^{-1})	0.70
Actual Total Cross Section of Material 2 (cm^{-1})	0.90
Actual Total Cross Section of Material 3 (cm^{-1})	1.10
Actual Total Cross Section of Material 4 (cm^{-1})	1.30
Actual Scattering Ratio for All Materials (c)	0.50
Homogeneous Initial Guess for Total Cross Sections (cm^{-1})	1.5
Homogeneous Initial Guess for Scattering Cross Sections (cm^{-1})	1.3
Illuminating Source Intensity ($\frac{n}{(cm^2-Sr)}$)	100
Illuminating Sources	1, 2, 3, 4 sides

Figs. VI-84 and VI-85 display the results of the reconstruction as sources are applied to only one side of the model. In this case, the reconstruction is unsuccessful just as it was not in the pure absorber problem in example 4. The single experiment with a single beam does not proved sufficient information about the domain to gen-

erate an image. Most likely the beam is sufficiently attenuated and scattered within the domain that measurable fluxes do not provide a good representation of the material properties of the domain and the reconstruction fails. This failure is evidenced by the large errors in the scattering and total cross sections which are on the order of 10^{-1} . The Newton iterations were terminated after five hundred iterations and forty hours.

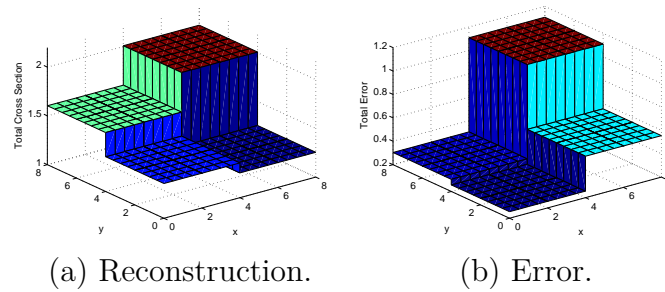


Fig. VI-84.: Total Reconstruction and Error for Four-Region Domain with Sources on 1 Side.

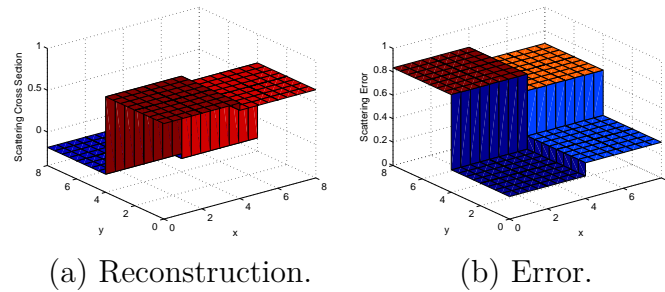


Fig. VI-85.: Scattering Reconstruction and Error for Four-Region Domain with Sources on 1 Side.

Figs. VI-86, VI-87, VI-88, VI-89, VI-90 and VI-91 display the reconstruction and error results for the other three models with sources on two, three or four sides of the model. All of these cases were successful and the general trend of a reduction

in the reconstruction error and an improvement in image quality as more sources are used can be seen in these results. The successful reconstructions were conducted in 124, 260 and 240 iterations for the simulations with beams on two, three and four sides, respectively. These reconstructions required ten and half, twenty-six and twenty-three hours for the studies with illuminating sources on two, three and four sides to complete, respectively.

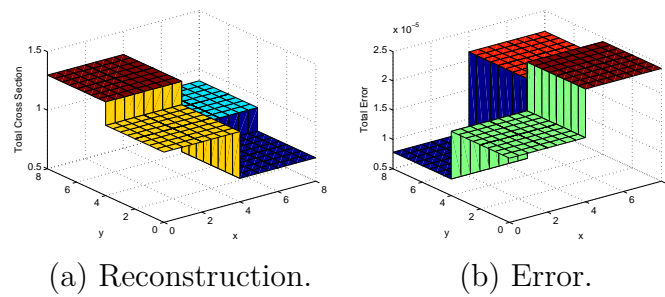


Fig. VI-86.: Total Reconstruction and Error for Four-Region Domain with Sources on 2 Sides.

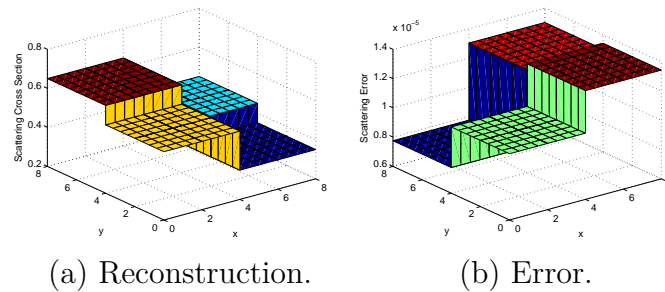


Fig. VI-87.: Scattering Reconstruction and Error for Four-Region Domain with Sources on 2 Sides.

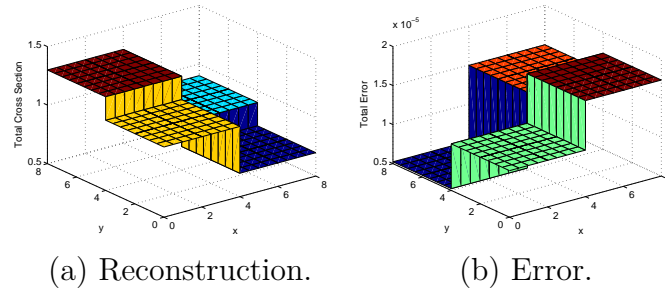


Fig. VI-88.: Total Reconstruction and Error for Four-Region Domain with Sources on 3 Sides.

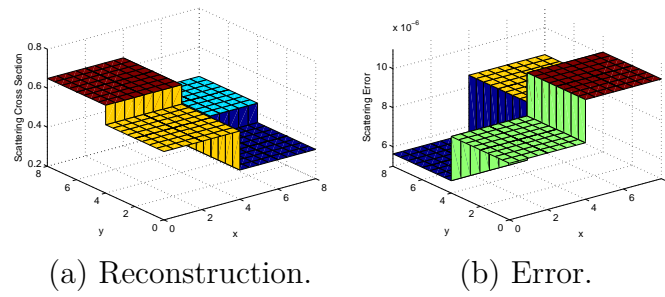


Fig. VI-89.: Scattering Reconstruction and Error for Four-Region Domain with Sources on 3 Sides.

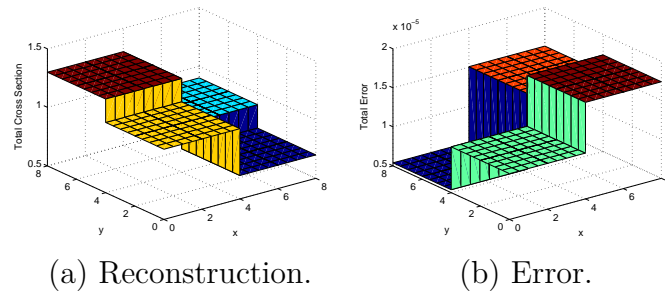


Fig. VI-90.: Total Reconstruction and Error for Four-Region Domain with Sources on 4 Sides.

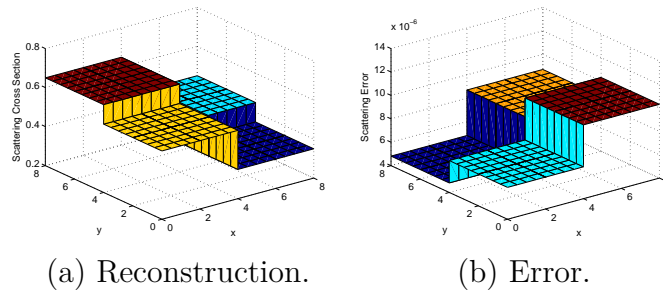


Fig. VI-91.: Scattering Reconstruction and Error for Four-Region Domain with Sources on 4 Sides.

7. Example 17 - Four-Region Domain Reconstructing Both Scattering and Total Cross Sections Using Measurements from 1, 2, 3 and 4 Sides

In example 17 the effects of using the measurements from different combinations of sides of the model in the reconstruction process are explored. All of the models seen in this example are simulated with eight experiments each covering half of a side and both the total and scattering cross sections are reconstructed simultaneously. All of the scattering cross sections in the models simulated in example 17 are maintained at 90% of the total cross section values. The same material region layout and side numbering scheme was used in this example as can be seen in Fig. VI-10 of example 4. Homogeneous initial guesses of 1.5 cm^{-1} and 1.3 cm^{-1} were used as starting points for Newton's method for the total and scattering cross sections. A list of the parameters that define the geometry, discretization scheme, reconstructed cross sections and source positions for the problem can be seen in Table VI-XXIII.

Table VI-XXIII.: Parameters Description of Four-Region Domain Measuring on 1, 2, 3 or 4 Side of Model

Angular Quadrature (Sn)	8
Domain Sizes (cm)	8x8
Number of Material Regions	4
Material Mesh	4x4
Flux Mesh	16x16
Number of Searched Parameters	4
Actual Total Cross Section of Material 1 (cm^{-1})	0.70
Actual Total Cross Section of Material 2 (cm^{-1})	0.90
Actual Total Cross Section of Material 3 (cm^{-1})	1.10
Actual Total Cross Section of Material 4 (cm^{-1})	1.30
Actual Scattering Ratio for All Materials (c)	0.90
Homogeneous Initial Guess for Total Cross Sections (cm^{-1})	1.50
Homogeneous Initial Guess for Scattering Cross Sections (cm^{-1})	0.85
Illuminating Source Intensity ($\frac{n}{(cm^2-Sr)}$)	100
Illuminating Sources	8-exp, 1/2-side each
Measurements	1, 2, 3 or 4 Sides

Figs. VI-92 and VI-93 display the reconstruction and error results as the total and scattering cross sections of the domain are reconstructed only with the measurements from one side. In this case, Newton's method was unable to reconstruct the

cross sections of the domain in the provided two hundred iterations. This was most likely due to the fact that insufficient information was collected from only measuring on one side of the model to correctly identify the material property distribution of the domain. This failed reconstruction is evident by the large errors seen in the reconstruction that are on the order of 10^0 . The two hundred iterations that were conducted for this problem lasted for about nine hours.

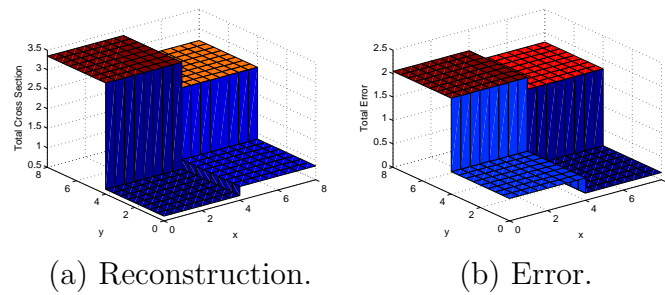


Fig. VI-92.: Total Reconstruction and Error Results for the Four-Region Domain with Measurements on 1 Side.

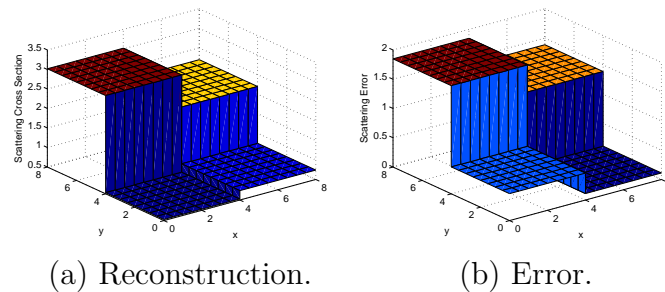


Fig. VI-93.: Scattering Reconstruction and Error Results for the Four-Region Domain with Measurements on 1 Side.

Figs. VI-94, VI-95, VI-96, VI-97, VI-98 and VI-99 are the reconstruction and error results for the scattering and total cross sections for the domain where measurements gathered from two, three or four sides of the model were used in the reconstruc-

tion. All of these simulations were successful. The trend of improved image quality and reduction in reconstruction error as more measurements are use to generate the image is again noted in this example. Forty-four, forty-nine and forty-nine iterations were required for the reconstruction for the models run with measurement collected from two, three and four sides, respectively. These simulations lasted twenty-four, twenty-nine and twenty-four hours to run, respectively.

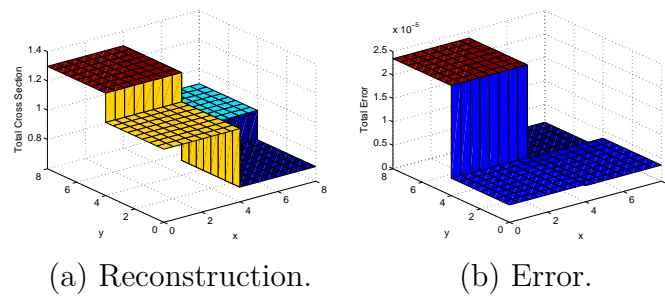


Fig. VI-94.: Total Reconstruction and Error Results for the Four-Region Domain with Measurements on 2 Sides.

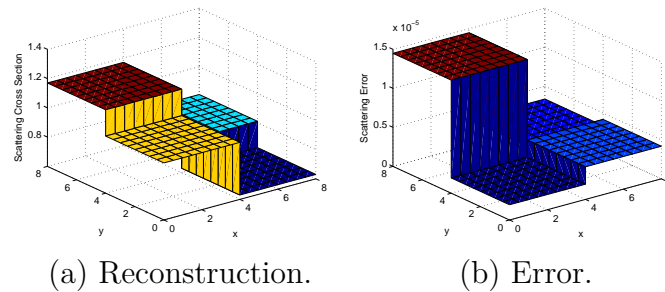


Fig. VI-95.: Scattering Reconstruction and Error Results for the Four-Region Domain with Measurements on 2 Sides.

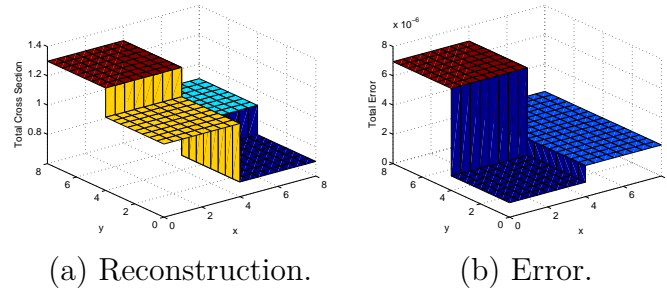


Fig. VI-96.: Total Reconstruction and Error Results for the Four-Region Domain with Measurements on 3 Sides.

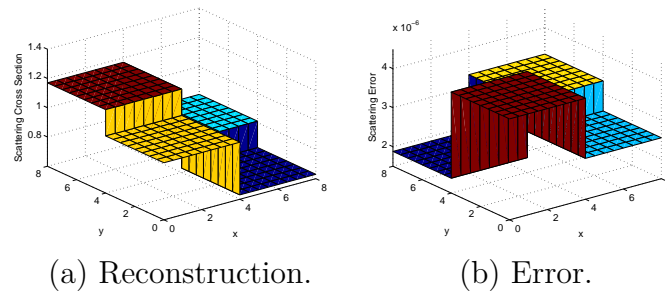


Fig. VI-97.: Scattering Reconstruction and Error Results for the Four-Region Domain with Measurements on 3 Sides.

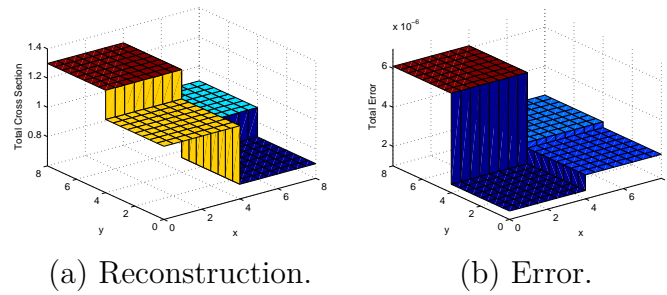


Fig. VI-98.: Total Reconstruction and Error Results for the Four-Region Domain with Measurements on 4 Sides.

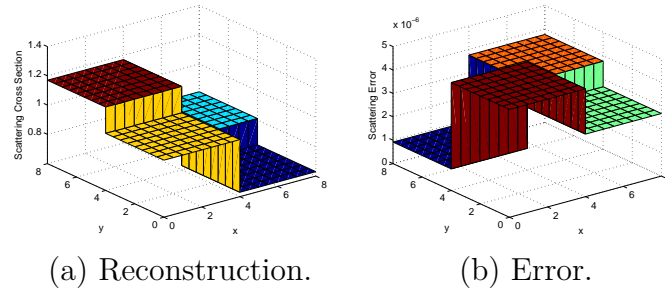


Fig. VI-99.: Scattering Reconstruction and Error Results for the Four-Region Domain with Measurements on 4 Sides.

8. Summary of Findings from Scattering Problems

In this section the challenges of introducing scattering into many problems was examined. It was noticed the scattering process increases the complexity of the inverse transport problem because the measurable radiation is now clouded with uncertainty about the origin of the particle. In the pure absorber problems, the image of the domain is generated based simply on the difference between the original intensity of the incident beams and the measured radiation at the measurement point. In other words, the amount of radiation that is removed from the beam or absorbed by the domain is used to create the image. However, when scattering is introduced, now radiation can be measured at the detectors after it has interacted within the domain. This complicated the reconstruction process because now the origin of the measured radiation is uncertain and can only be categorized by a probability. This again is more complex than the pure absorber problems where radiation only traverses the domain in straight lines. Only isotropic scattering was studied in this thesis as well, so in actuality the inverse transport problem contains even more complexity.

In addition to the added difficulty noticed in all of the scattering problems, some other unique findings were uncovered in each of the specific scattering problems. In

example 11, the misfit surface of a two-parameter problem was plotted as to understand its shape as the scattering and total cross sections were varied. This evidenced the additional difficulty in determining the scattering cross section and that the surface was often rather flat unless the proposed values was very near the actual solution. This meant that the gradient of the misfit provided little information about the location of the minimum and the wall of the misfit valley were also noticed to be convex. Both of these observations again reinforce the complexity of the inverse transport problem. In example 12, a simple homogeneous domain was examined to get a feel for the capability of Newton's method to reconstruct both the scattering and total cross sections. The method had little trouble reconstructing these parameters, but the computational time required for problems with scattering was noted and algorithm was optimized for better performance. In example 13, the four-strip domain was revisited with signal noise and bias. The same trends were noticed in the scattering reconstruction as in the pure absorber problems. Increasing the noise in the measured fluxes caused greater error in the reconstructed image. Signal bias had the effect of shifting the cross section of the domain in either the positive or negative direction due to the uniform increase or decrease seen in the measured fluxes. In example 14, central inclusion problems with scattering of increasing optical thickness are considered. An optical thickness limit of 2-3 mean free paths thick was determined to be the maximum depth that permitted a successful reconstruction of the cross sections of the domain. In example 15, the initial guess studies were revisited and the complexity of the scattering problems became apparent as many of the initial guess that were successful for the pure absorber problems were not for the scattering cases. The same challenges were noticed as Newton's method approached the solution from a lower initial guess and higher initial guess proved to be more reliable. In example 16, the problem where sources were applied to different combinations of

sides of the domain was studied for a scattering problem. Again, when the beam was imposed on only one side of the model, insufficient information could be collected to fully characterize the material properties of the domain. The reconstruction was successful when beams were imposed on more sides of the model and as more beams were imposed, image quality improved. Finally, in example 17 a four region domain with scattering was reconstructed with measurements from various numbers of sides of the domain. The added complexity of scattering was noted as the reconstruction was unsuccessful when measurements were collected from only one side of the model, because this case was successful for the pure absorber case. The trend of improved image quality as measurements were recorded from more sides of the model was again evident.

CHAPTER VII

CONCLUSIONS AND OUTLOOK

Using transport theory and Newton's method to create images of various domains has the potential to be a useful algorithm to analyze cargo container scans. First, this algorithm generally requires fewer iterations and computational time than any derivative-free technique. Second, this method is also easy to implement as long as the first and second derivatives of the Lagrangian function can be computed. Third, it is also flexible enough to accommodate differing illuminating sources, numbers of experiments, initial guesses and measurement locations. Fourth, this technique showed a successful ability to reconstruct domains where signal noise and bias was applied to the angular fluxes. And last, the inverse transport method proved capable to reconstruct a wide range of problems ranging from pure absorbers to highly scattering mediums.

Many limitations of applying Newton's method to the transport equation were also noted. First, a maximum of ten mean free paths thick for pure absorbers and two mean free paths for scattering problems were determined to be the maximum optical thicknesses where the measurable signal from the illuminating sources is still strong enough to permit reconstruction. Second, the dependence of the success of the reconstruction and the required computational time was determined to be highly dependent on the initial guess for the parameters. And third, this method allows for Newton's method to propose negative cross section values and scattering cross sections that are larger there corresponding total cross section. An additional backtracking technique was employed as an attempt to prevent this problem, but these scenarios have no physical meaning and further constraints could be applied to prevent this.

Looking forward, there are a few ways to improve how Newton's method is applied to the optimality conditions of the inverse transport problem. First, a more robust line search than the Armijo or Wolfe backtrack technique could be employed to ensure that Newton's method does not overshoot the true solution. Second, the Lagrangian could be modified to include further constraints including an upper and lower bound on the cross sections and a check that ensures that the total cross section is always greater than or equal to the scattering cross section. Third, a method for treating the uncollided flux could be considered in unison with this method to better characterize the uncollided radiation. Fourth, a preconditioner could be implemented to provide Newton's method with an improved initial guess for the distribution of the cross sections within the domain. Fifth, this method could be made compatible with adaptive meshing strategies so that finer meshes could be generated in areas of interest and coarser meshes could be used for less interesting areas. Sixth, anisotropic scattering could be added to the forward solver to expand the range of problems that can be considered with the method. Seventh, the method could be extended to three dimensions to tackle more realistic problems. And last, this method could be parallelized so that the problem could be solved more efficiently on multiple processors.

REFERENCES

- [1] J. B. McNeill, “100 Percent Cargo Container Scanning: A Global Disaster,” Webmemo #2407, Kathryn and Shelby Cullom Davis Institute for International Studies (2008).
- [2] J. Fontelera, “Homeland Security to Miss Cargo Scanning Deadline,” Thomas-Net News; available on the internet at <http://news.thomasnet.com/mt41/mt-tb.cgi/1876> (March 4, 2009).
- [3] D. Slaughter, M. Accatino, A. Bernstein,, J. Candy, A. Dougan et al., “Detection of Special Nuclear Material in Cargo Containers Using Neutron Interrogation,” UCRL-ID-155315, Lawrence Livermore National Laboratory (2003).
- [4] G. Aloise, L. Cogliani, N. Crothers, J. Fremont, J. Shafer et al., “Combating Nuclear Smuggling: DHS’s Cost-benefit Analysis to Support the Purchase of New Radiation Detection Portal Monitors Was Not Based on Available Performance Data and Did Not Fully Evaluate All the Monitors’ Costs and Benefits,” GAO-07-133R, United States Government Accountability Office (2006).
- [5] W. Bangerth, “A Framework for the Adaptive Finite Element Solution of Large-Scale Inverse Problems,” *SIAM Journal on Scientific Computing*, **30**, 2965 (2008).
- [6] E. Haber and U. M. Ascher, “Preconditioned All-at-Once Methods for Large, Sparse Parameter Estimation Problems,” *Inverse Problems*, **17**, 1847 (2001).
- [7] A. D. Klose, and A. H. Hielscher. “Iterative Reconstruction Scheme for Optical Tomography Based on the Equation of Radiative Transfer,” *Medical Physics*, **26**, 1698 (1999).

- [8] A. D. Klose, and A. H. Hielscher, “Quasi-Newton Methods in Optical Tomographic Image Reconstruction,” *Inverse Problems*, **19**, 387 (2003).
- [9] A. Klose, V. Ntziachristos, and A. Hielscher, “The Inverse Source Problem Based on the Radiative Transfer Equation in Optical Molecular Imaging,” *Journal of Computational Physics*, **202**, 323 (2005).
- [10] G. S. Abdoulaev, K. Ren, and A. H. Hielscher, “Optical Tomography as a PDE-constrained Optimization Problem,” *Inverse Problems*, **21**, 1507 (2005).
- [11] G. S. Abdoulaev, and A. H. Hielscher, “Three-Dimensional Optical Tomography with the Equation of Radiative Transfer,” *Journal of Electronic Imaging*, **12**, 594 (2003).
- [12] A. H. Hielscher and S. Bartel, “Use of Penalty Terms in Gradient-Based Iterative Reconstruction Schemes for Optical Tomography,” *Journal of Biomedical Optics*, **6**, 183 (2001).
- [13] W. Bangerth and A. Joshi, “Adaptive Finite Element Methods for the Solution of Inverse Problems in Optical Tomography,” *Inverse Problems*, **24**, 034011 (2008).
- [14] R. Roy and E. M. Sevick-Muraca, “Active Constrained Truncated Newton Method for Simple-Bound Optical Tomography,” *Journal of the Optical Society of America A*, **17**, 1627 (2000).
- [15] E. M. A. Hussein and J. T. C. Bowles, “Expanding the Domain of Contraction Mapping in the Inverse Problem of Imaging with Incoherently Scattered Radiation,” *Inverse Problems*, **23**, 1289 (2007).
- [16] V. Scipolo, “Scattered Neutron Tomography Based on a Neutron Transport Problem,” Master’s thesis, Texas A&M University, College Station (2004).

- [17] M. R. Sternat, “Application of a Constrained Optimization Technique to the Imaging of Heterogeneous Objects Using Diffusion Theory,” Master’s thesis, Texas A&M University, College Station (2009).
- [18] Z. Wu, “Advances in Inverse Transport Methods and Applications to Neutron Tomography,” Ph.D. dissertation, Texas A&M University, College Station (2010).
- [19] W. M. Stacey, “Nuclear Reactor Physics,” John Wiley & Sons, New York (2001).
- [20] J. Nocedal and S. J. Wright, “Numerical Optimization,” Springer, New York (2006).
- [21] J. A. Nelder and R. Mead, “A Simplex Method for Function Minimization,” *The Computer Journal*, **7**, 308 (1965).

VITA

Nathaniel Raymond Fredette was born to Mark A. Fredette and Denise M. Fredette in Houston, TX. He graduated from Strake Jesuit College Preparatory in 2004, received his Bachelor of Science in mechanical engineering from Marquette University in 2009 and his Master of Science in nuclear engineering from Texas A&M University in 2011. He is a member of the American Nuclear Society and the National Scholars Honor Society. His primary interests are nuclear reactor design and simulation specifically related to naval applications. He plans to start a career with Knolls Atomic Power Laboratory designing power reactors.

Department of Nuclear Engineering

Texas A&M University

3133 TAMU

College Station, TX 77843-3133

nate.fredette@gmail.com